Deltares

Rip Current Characteristics at the Dutch Coast: Egmond aan Zee

1204386-000

Deltares

Title

Rip Current Characteristics at the Dutch Coast: Egmond aan Zee

Project	Reference	Pages
1204386-000	1204386-000-HYE-0004	151

Keywords

Rip currents, Egmond aan Zee, Field experiment, Lagrangian flow measurements, GPS drifter, Numerical modelling, XBeach

Abstract

Rip currents are narrow, seaward directed flows in the surf zone that pose a serious threat to swimmers as they pull them offshore into deeper waters. This issue has received attention particularly on swell dominated coasts (such as the US, Australia, France and UK) where numerous field experiments have been undertaken. However, the threat of rip currents is less recognised on wind-sea dominated coasts such as the North Sea, even though a consistent number of swimmers drift offshore (in rip currents) and require rescue by surf lifeguards each year (for example at Egmond aan Zee, The Netherlands).

The main objectives of this research were to investigate the mean flow characteristics of rip currents at Egmond aan Zee and to identify the prominent parameters that drive these currents. A field study was undertaken with drifter instruments and human drifters that were tracked via GPS to measure rip currents in the field and to correlate their behaviour to outside forcing. The applicability of the numerical model XBeach was assessed in the hindcast of a laboratory rip current experiment and the field experiment presented in this study. The sensitivity of rip currents to various hydrodynamic and geometric parameters was tested in a this validated XBeach model. Along with the field data the results of the sensitivity analysis were used to identify the governing parameters of rip currents at Egmond aan Zee and to describe the particularities of these currents compared to rip currents in other environments.

Version	Date	Author	Initials	Review	Initials	Approval	Initials
	Mar-12	G. Winter		A.R. van Dongeren		T. Schilperpoort	

State

final

Deltares

Rip Current Characteristics at the Dutch Coast: Egmond aan Zee

By

Gundula Winter

February 2012

A thesis submitted in partial fulfilment of the requirements for the degree of

Master of Science

in the field of

Civil Engineering

at

Delft University of Technology

Delft, The Netherlands

TU Delft Delft University of Technology

Graduation Committee:

Prof.dr.ir. M.J.F. Stive	Chairman, Delft University of Technology
Dr.ir. A.R. van Dongeren	Deltares
Dr.ir. J.S.M. van Thiel de Vries	Deltares / Delft University of Technology
Ir. M.A. de Schipper	Delft University of Technology
Dr.ir. M. Zijlema	Delft University of Technology
Ir. R. Morelissen	Deltares

This research was carried out at:

Deltares
Rotterdamseweg 185
2600 MH Delft

The Netherlands

Cover: Drifter experiments at the beach of Egmond aan Zee
Picture by: Prof.dr.ir. Dano Roelvink, 2011

Abstract

Rip currents are narrow, seaward directed flows in the surf zone that can pose a serious threat to swimmers. This issue has received attention particularly on swell dominated coasts (such as the US, Australia, France and UK) where numerous field experiments have been undertaken. However, the threat of rip currents is less recognised on wind-sea dominated coasts such as the North Sea, even though a consistent number of swimmers drift offshore (in rip currents) and require rescue by surf lifeguards each year (for example at Egmond aan Zee, The Netherlands).

In August 2011, a five day field experiment was conducted at Egmond aan Zee. Lagrangian velocities in the surf zone were measured with drifter instruments and human drifters that were tracked via GPS. An extensive dataset of measurements was collected from which parameters that govern the strength of rip currents and affect their mean flow properties were identified.

Three flow patterns were observed in the experiment: (1) a locally governed circulation cell, (2) a pattern in which the drifter initially floats offshore and then is advected by a strong long-shore current and (3) a meandering longshore current. A variety of rip current velocities were measured with the strongest being approximately 0.6 m/s. A statistically significant correlation between the ratio of offshore wave height over water depth on the bar and rip current speeds was established from the data.

A 2-dimensional hydrostatic XBeach model was validated against laboratory rip current experiments and field data from Egmond aan Zee. A sensitivity analysis was performed to test a range of parameters that were categorised into two groups of different time scales: hourly and daily altering hydrodynamic parameters, and daily to weekly (sometimes longer) varying geometric parameters. Various hydrodynamic scenarios of wave height, wave period, wave angle and tidal water level were tested to evaluate the influence on rip current initiation and mean flow properties. Additionally, the importance of wave and tidal driven longshore currents was investigated. The key geometric parameters tested were channel width and depth. A reduction of the hydrodynamic parameters along with simplification of the model bathymetry allowed for identification of the governing rip current parameters.

The sensitivity analysis demonstrated that rip currents strengthen with increasing wave height, decreasing water depth over the updrift bar and increasing channel depth. The influence of the wave period was of secondary importance and the wave angle did not affect the offshore rip current velocity for site specific channel dimensions. The wave angle was observed to only have an impact for relatively narrow channels (relative to the forcing).

This study revealed similarities and differences of rip currents at the Dutch coast and rip currents at previous field sites. The driving parameters of rip currents were identical; however, the flow patterns differed. While in previous field experiments drifters were predominantly retained within the surf zone, most drifters at Egmond aan Zee were ejected from the surf zone and did not return shoreward. Offshore of the channel the drifter behaviour was governed by the tidal current that advected the drifters alongshore. In case of weak tidal currents (slack water) the rip currents extended far offshore.

Acknowledgements

I would like to acknowledge the support and contribution of many people who were involved in this study that I thoroughly enjoyed working on as well as the people who accompanied me through my studies:

First of all, I want to thank my graduation committee for their support and guidance in this research: To prof.dr.ir. M.J.F. Stive who drew my attention to Coastal Dynamics and enabled me to conduct this diverse project. Special thanks to my daily supervisors dr.ir. A.R. van Dongeren who developed the research idea and guided me throughout this project, dr.ir. J.S.M. van Thiel de Vries for his endless time to explain and discuss the numerical model XBeach and to ir. M.A. de Schipper for his never-ending interest in my research, his highly valued food-for-thought and his much appreciated experience in field work. Further I want to thank dr.ir. M. Zijlema for his thoughtful comments on numerical modelling and ir. R. Morelissen for introducing me to the world of Argus (remote video imaging).

Assoc.prof.dr.ir. A.J.H.M. Reniers (University of Miami) for the inspiring email discussions on wave current interaction and wave dissipation in XBeach and ir. R. McCall (Plymouth University) for the appreciated practical input to the numerical modelling component of this study.

Shore Monitoring who provided help and equipment during the field experiment and who conducted the bathymetry survey. On site Shore Monitoring was represented by Roeland de Zeeuw and Sierd de Vries.

To Willem Verbeek whose long-year experience with rip currents at Egmond aan Zee was highly valued and who greatly documented the field experiment in photos.

I thank the many volunteers who resisted the cold North Sea water and assisted in collecting the field data: Andrew Pomeroy, Antoon Hendriks, Arnold van Rooijen, Claire Bouchigny, Cilia Swinkels, Dano Roelvink, Dirk Knipping, Erwin Bergsma, Giorgio Santinelli, Greta van Velzen, Hesseltje Roelvink, Ivan Garcia, Jamie Lescinski, Jeroen Stark, Lisa de Graaf, Leo Sembiring, Maarten van Ormondt, Roland Vlijm, Timon Pekkeriet and in particular Brice Blossier, le chef de BBQ, who catered us after energy-sapping drifter experiments. You all made the week in the field a memorable experience.

I also thank the lifeguards at Egmond aan Zee who invited me for trainings and shared their practical experience on rip currents with me.

Rijkswaterstaat is gratefully acknowledged for the use of the wave buoy data taken at Petten that was provided to me by Andre Jansen.

And Saskia Huisman from Deltares is thanked for providing help in the analysis of the sediment samples.

I am grateful for the many friends from all over the world I met during my studies and that made my time in Delft truly enjoyable. In particular, the students at Deltares that I shared many coffees, ideas and modelling frustrations with.

To my family, that supported me throughout my whole studies and always believed in my abilities. To my brother, despite being far away, who gave me advice and confidence and got me physically fit through this research project.

And most of all I want to thank Andrew for his patience, the discussions on my research, mental support, the countless coffees, the enjoyable weekend trips and simply for being there for me. Thanks for everything.

I would like to acknowledge Deltares who hosted me and supported this study. The research was funded by Flood Control 2015 (Realtime Safety on Sedimentary Coasts program) and Building with Nature (Swimmer Safety project), Deltares Strategic Funding in the framework of the System Tools for Prevention and Preparation program (project 1202362).

Contents

Figures and Tables

1 Introduction

1.1 Background

Rip currents are a serious hazard to beach users at many beaches all over the world. These seaward-directed currents typically pull swimmers offshore whilst the swimmers intuitively try to swim against the current. Often the swimmers become exhausted and require professional help. *Brander and MacMahan* [2011] estimate that the annual number of drownings associated with rip currents is likely to exceed 500 worldwide. In The Netherlands, the Surf lifesavers at Egmond aan Zee have identified strong rip currents that are of high risk to swimmers at their beach. In the summer of 2010, the surf lifesavers attributed the rescue of 16 people to only one of these rip currents [2010]. These rip currents are tied to channels that interrupt the inner sand bar. Improved insight into the near shore hydrodynamics at Egmond may provide useful information to assess where and when dangerous conditions could be expected. This may assist lifeguards to reduce the future risk of these rip currents and also aid in the development of rip forecast models. So far, rip current research has been concentrated on swell dominated coasts (such as the US coast, Australian coast and the French and British Atlantic coast) while little research has been undertaken in wind-sea dominated environments such as the Dutch coast. In particular the influence of strong wave-driven and tidal longshore currents on rip current initiation and strength is not fully understood.

1.2 Research question and objectives

Rip currents induce complex flow patterns in the nearshore zone and are affected by a range of geometrical and hydrodynamic parameters. The influence of these parameters along the Dutch North Sea coast is not well understood but is likely to have a specific impact on rip currents found along the Dutch coast.

The aim of this study is to investigate the particular characteristics of rip currents at the Dutch coast and to evaluate the capability of a numerical model to simulate these currents.

The specific objectives of this research are to:

- identify and describe the surf zone flow patterns at Egmond aan Zee;
- identify the particularities of rip currents at Egmond aan Zee;
- correlate the mean flow properties of rip currents with hydrodynamic forcing, in particular
  - wave height,
  - water level,
  - wave angle,
  - wave period, and
  - tidal current velocity;
- evaluate the importance of distinct geometric parameters which are
  - rip channel width,
  - rip channel depth and
  - small scale bed irregularities; and
- evaluate the suitability of XBeach for modelling rip currents.

1.3 Methodology

The present study consists of four main components: (1) A pre-field experiment study to determine the suitability of the numerical model XBeach and to develop hypotheses, (2) a field experiment, (3) field data analysis and (4) a numerical modelling study.

In the first component of this study, the suitability of XBeach to model rip currents is demonstrated against data collected during a laboratory experiment. The numerical model XBeach was selected for the modelling component of this study because it accounts for wave current interaction. This is crucial to model the flow in the rip channel where the current opposes the incident waves. A synthetic model was then used to test the applicability of XBeach in site scale dimensions. A review of previous studies along with the results of the synthetic model assisted to formulate hypotheses prior to the field campaign and to define a measurement plan for the field experiment.

The field experiment (component 2) measured the flow patterns and velocities of rip currents at Egmond aan Zee (hereafter Egmond). The measurements were then correlated to the hydrodynamic conditions present during the field campaign (component 3). The underlying bathymetry was surveyed during the field experiment and was used to set up a hindcast model in XBeach that was validated with the data obtained in the field.

In the fourth component of the study, the validated model was used to identify the parameters that govern rip currents at Egmond. The identified parameters were then subjected to a sensitivity analysis and the results were compared with rip observations in Egmond aan Zee and other environments.

1.4 Structure of the report

Chapter 2 summarises the theoretical background associated with the generation and characteristics of rip currents along with the results of key studies. The features of the numerical model XBeach utilised in this study are then presented in Chapter 3. Herein, the capability of XBeach to model rip current flow is demonstrated by simulation of a physical experiment conducted by *Haller et al.* [2002]. A synthetic model of Egmond is then used to model rip currents of field site scale and the results are compared against observations reported in literature and by lifeguards at Egmond aan Zee. A description of the field site, methods and results follow in Chapter 4 with the results of the rip current measurements in particular described in Chapter 5. Chapter 6 presents a selection of the measurements used to validate the hindcast model while the hydrodynamic and geometric parameters that govern rip current properties identified in the model are presented in Chapter 7. Finally, the conclusions and recommendations of the study are summarised in Chapter 8.

2 Literature Review

2.1 Description of a rip current cell

Under the influence of wave breaking, it has been observed that most floating objects move shoreward. This has led to the conclusion, in order to satisfy the continuity equation of mass, that some form of a return flow must compensate for the landward movement of water. The return flow can have two forms: (a) a longshore uniform undertow that flows at intermediate depths or (b) a narrow offshore directed flow that stretches over the whole water column, the so-called rip current. From discussions with lifeguards in California *Shephard et al.* [1941] concluded that the latter is widely evident and must therefore account for most of the return flow. In the field he identified three components that together form a rip current (Figure 2.1). The first is a feeder current formed by water moving parallel to the shore. The second is a rip neck that is maintained by feeder currents from either side or, in some cases, by a feeder current from one side only. The flow in the rip neck is narrow and offshore directed and exhibits the strongest flow velocities and will be referred to as rip strength. The third component is the rip head in which the flow diffuses and the velocities decrease. Together with the onshore mass transport of water in the breaker zone the rip current forms a closed circulation cell.

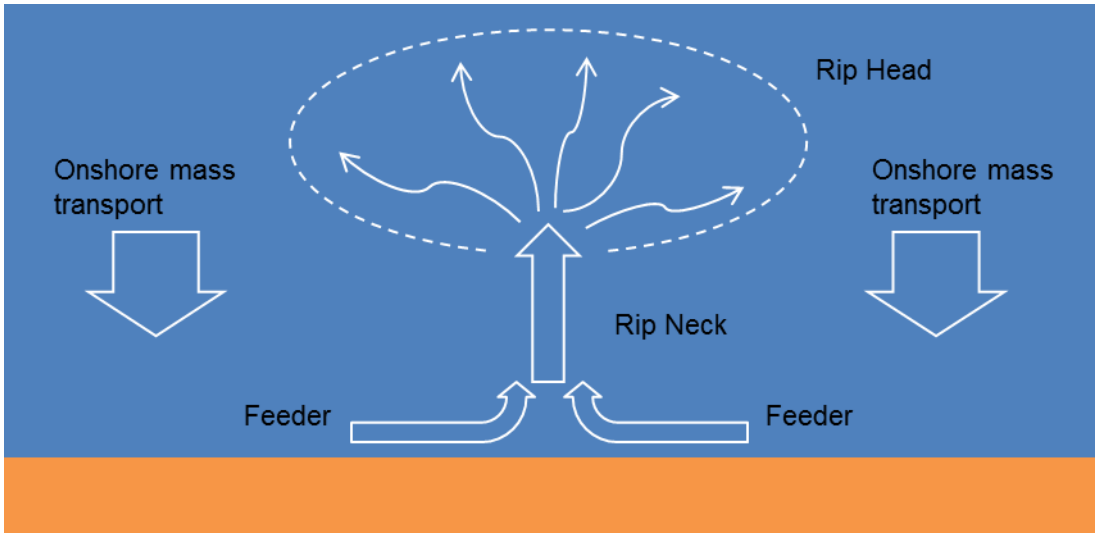

Figure 2.1 Definitions in a rip current system

2.2 Generation of rip currents

The concept of radiation stress is essential to describe the generation of rip currents. Waves induce a momentum flux in the water column that arises due to the particle motions in a wave $\rho\vec{u}$ and the wave-induced pressure p_{wave}. The time averaged transport of momentum per unit width is referred to as radiation stresses [*Longuet-Higgins and Stewart*, 1964]:

$$S_{xx} = \overline{\int_{-d}^{\eta} \left(\rho u_x^2 + p_{wave} \right) dz} = \left(n - \frac{1}{2} + \cos^2 \theta \right) E$$
$$S_{yy} = \overline{\int_{-d}^{\eta} \left(\rho u_y^2 + p_{wave} \right) dz} = \left(n - \frac{1}{2} + \sin^2 \theta \right) E \quad (2.1)$$
$$S_{xy} = S_{yx} = \overline{\int_{-d}^{\eta} \left(\rho u_x u_y + \tau_{xy} \right) dz} = n \cos\theta \sin\theta E$$

S_{xx} and S_{yy} are the radiation stresses in cross-shore and longshore direction, S_{xy} or S_{xy} are the radiation shear stresses, n is the wave number and θ is the angle of wave incidence. The wave energy E is given by:

$$E = \frac{1}{8} \rho g H^2 \quad (2.2)$$

The shoreward evolution of wave height generates gradients in the radiation stresses. When wave height decays (as a consequence of breaking), a negative radiation stress gradient develops. This induces a positive net force on the water body. To compensate for these wave-induced forces and satisfy the momentum balance equation in the cross-shore direction, the radiation stress gradient is balanced by a pressure gradient:

$$\frac{\partial S_{xx}}{\partial x} = -\rho g (h + \bar{\eta}) \frac{\partial \bar{\eta}}{\partial x} \quad (2.3)$$

where $\bar{\eta}$ is the mean water level elevation and h the still water depth. Thus, wave breaking exerts a force in the water column that induces a water level set up at the shoreline.

A rip current is driven by longshore gradients in water level set-up that originate from alongshore varying pressure gradients in cross-shore direction. These gradients stem from the longshore non-uniformity of either the wave field or the bottom topography [*Bowen*, 1969]. The water level set-up is large shoreward of an area with intense wave breaking triggered by high waves or small water depths whilst shoreward of an area with moderate or no wave breaking the set-up is somewhat smaller or absent. The resultant longshore water level gradients drive shore parallel flows. Longshore flows with opposite direction converge at locations with less set up and feed the rip current.

2.3 Morphologically controlled rip currents

Dalrymple [1978] has identified that the most common form of rip currents are controlled by the underlying morphology. This group consists of rip currents induced by the bottom topography, coastal boundaries (such as breakwaters and groins) and barred coastlines. These morphologically controlled rip currents are found to be stronger than their not morphologically controlled counterparts, the so called transient rip currents [*Dalrymple et al.*, 2011]. This thesis will focus on barred coastlines and the rip currents induced in this context.

The location of morphologically controlled rip currents is tied to a rip channel that interrupts the sand bar. The generation of rip currents in this context can be explained by (1) a force and (2) a mass balance approach. (1) Waves break over the bar and the resultant wave forcing causes a relatively high water level set-up in the trough between the beach and the

bar. In the channel the waves break later (due to the deeper water) and induce less set up. A longshore flow parallel to the beach is initiated (by a gradient in set-up) towards the rip channel where it is deflected offshore. (2) Breaking waves also transport water onshore in the roller of the broken waves. To satisfy the continuity of mass the landward transport of water over the bar needs to be compensated by some form of return flow. In the case of a bar with incised rip channels this return flow takes place in the form of a rip current.

A second circulation cell has also been observed in an experimental study by *Haller et al.,* [2002] (Figure 2.2). In the rip channel the waves progress closer to shore and finally break while behind the bar the waves are either smaller or absent. This results in a larger wave set-up in the rip channel than behind the bar. This gradient in set-up causes the water to flow away from the rip channel and in the opposite direction to the feeder current.

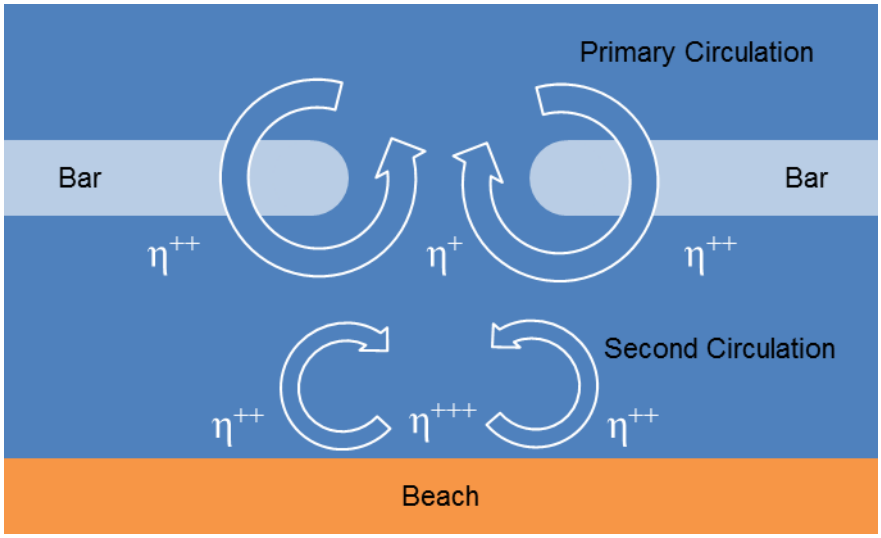

Figure 2.2 Bathymetric controlled rip current; η^{+++}: high wave set-up, η^{++}: intermediate wave set-up, η^{+}: low wave set-up

The channel itself evolves from an initially small bottom perturbation and quickly grows through a feedback mechanism. The offshore current transports sediment from the channel seawards where it is deposited at the rip head and the channel gradually deepens.

On the morphological time scale of the beach, rip channels change and for this reason may migrate slowly in longshore direction over the course of several days, weeks or months. Rip channels have been found on all of the intermediate beach configurations described by *Wright et al.* [1984] (Figure 2.3): Longshore Bar Trough (LBT), Rhythmic Bar an Beach (RBB), Transverse Bar and Rip (TBR) and Ridge and Runnel or Low Tide Terrace respectively (RR or LTT). RBB and TBR beach states are found to inhibit the highest longshore variability [*Ranasinghe et al.*, 2004] and thus rip channels are most pronounced.

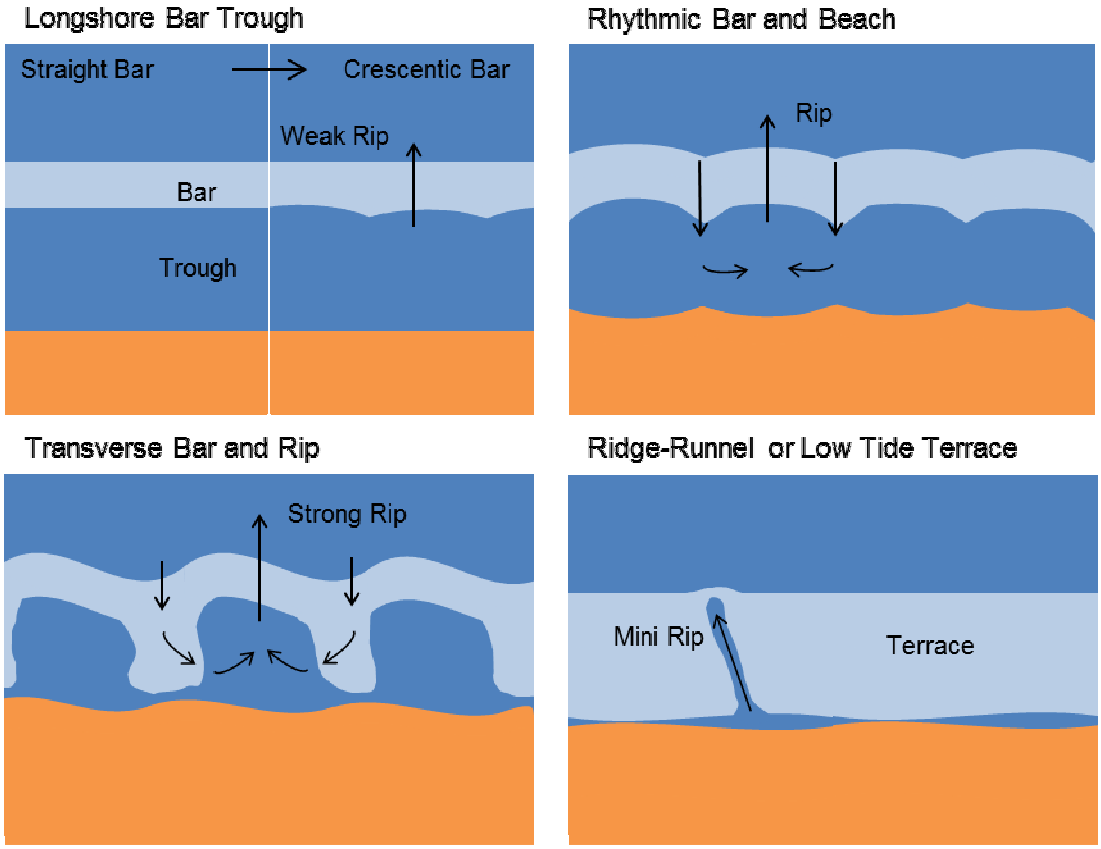

Figure 2.3 The intermediate beach states [adapted from Wright et al., 1984].

2.4 Characteristics of rip currents

Rip current flow is conditional upon wave dissipation. Waves will break over the bar if the ratio of wave height to water depth exceeds a certain value. This implies that rip currents are not only dependent on wave height but also on the water level that is modified by the tide. The strongest rip velocities have been measured in the field at low tide [*Aagaard et al.*, 1997; *Austin et al.*, 2010; *Brander and Short*, 2000; *MacMahan et al.*, 2005; *Sonu*, 1972]. In a study at the Danish North Sea coast, *Aagaard et al.* [1997] determined that rip currents are initiated when the ratio of significant wave height over water depth on the bar (γ_s) exceeds 0.35. At high tide they observed that waves passed over the bar without breaking and as a consequence the rip current was weaker or completely inactive. *Austin et al.* [2010] attribute the enhancement of rip currents during low tide to (1) the large wave dissipation gradient from the bar to the channel and (2) to flow restriction. However, at Egmond aan Zee the surf lifeguards report most dangerous rip current conditions just after low water with upcoming tide. This observation is addressed further in Chapter 7.

Rip currents do not exhibit a stationary flow, but rather pulsate at low frequencies. Several mechanisms have been proposed to explain these rip pulsations:

- *Haller and Dalrymple* [2001] associate these pulsations with jet instabilities in the rip current.

- *Haas et al.* [2003] suggest that pulsations are associated with the effect of wave current interaction. The offshore directed current slows down wave propagation in the channel. As a consequence the incident waves steepen and bend (due to current refraction) towards the centre of the channel. Eventually waves begin to break in the channel and induce a water level set-up that in turn reduces the longshore water level gradient. As the longshore water level gradient is the main driving mechanism of the rip current, this leads to reduced rip velocities. The weaker rip affects wave propagation less and wave breaking no longer occurs in the channel. Hence, the current again increases in strength. This feedback mechanism leads to pulsations of the rip current.

- Another mechanism is proposed for irregular wave fields by *MacMahan et al.* [2004]. The spatial and temporal wave height variability associated with wave groups induces fluctuations in the wave forcing. The spatial and temporal variation in the wave forcing and its coupling with the underlying bathymetry cause rip current cells to oscillate at very low frequencies (VLF, below 0.004 Hz). The VLF motions are believed to cause the infrequent surf zone exits of floating material while Stokes drift accounts for the retention of drifters within the surf zone [*Reniers et al.*, 2009].

In active rip currents, the flow velocity in the rip neck has been measured to be typically in the order of 0.3 to 0.6 m/s (Table 2.1) but can be as high as 2 m/s due to velocity fluctuations in the rip current. The total rip velocity is the superposition of velocity components with different frequency bands [*MacMahan et al.*, 2006]:

$$u_{rip} = u_{mean} + u_{IG} + u_{VLF} + u_{tide} \tag{2.4}$$

where u_{mean} is the mean rip velocity that describes the offshore flow due to the 2D circulation pattern, u_{IG} is the contribution within the infragravity band, 0.004–0.04 Hz (25–250 s), u_{VLF} is the contribution within the very low frequency band, 0.0005–0.004 Hz (4–30 min) and u_{tide} is the velocity modulation associated with the tidal water level (12.25 hours). The study will focus on the mean velocity in the rip current and the tidal modulation.

*Table 2.1 Overview of rip current characteristics as they were observed in the field (adapted from MacMahan et al. [2006]), where u_{rip} is the cross-shore rip velocity, u_{max} is the maximum measured rip velocity, λ_r is the rip channel spacing, w_r is the rip channel width, h_r * is the rip channel depth, h_b* is the bar height, H_{m0} is significant wave height, T_p is the peak wave period, and D_{50} is the median sediment size.(* relative to MSL)*

Location	u_{rip} *[m/s]*	u_{max} *[m/s]*	λ_r *[m]*	w_r *[m]*	h_r *[m]*	h_b *[m]*	H_{m0} *[m]*	T_p *[s]*	D_{50} *[mm]*
Skallingen (DEN)	0.3	1.7	90	150	1.25	1	0.8	8	0.25
Palm Beach (AUS)	0.4	2	200	60	1.8	1	0.75	10	0.35
Muriwai (NZL)	0.65	2	500	150	1.5	1	1.5	14	0.25
Moreton Island (AUS)	0.4	1	300	35	1.4	1	0.5	10	0.2
Torrey Pines (CA,USA)	0.2	1	300	35	1.4	1	0.5	12	0.1
Monetery (CA,USA)	0.3	2	1.25	60	1.5	1	1.5	12	0.35
Sea Grove (FL,USA)	0.35	1.25	60	30	0.8	0.3	0.5	8	0.3

To put the rip current velocities presented in Table 2.1 in context, a list of swimmer speeds dependent on the swimmer level and age group is given in Table 2.2. Following this table

mean rip velocities alone constitute a danger to older and poor trained swimmers while maximum rip velocities up to 2 m/s pose a danger even to well trained swimmers who cannot swim against a current of this magnitude.

Table 2.2 Swim speeds dependent on age and swimmer level. The values resemble swim speeds that can be maintained for as long as 12 min in a swimming pool (adapted from www.muien.nl). 'M' indicates the results for male and 'F' for female swimmers.

Swimmer level		Age Group				
		13-19	20-29	30-39	40-49	50-59
		Swim speed [m/s]				
Very poor	M	< 0.7	< 0.6	< 0.49	< 0.4	< 0.35
	F	< 0.6	< 0.4	< 0.35	< 0.28	< 0.21
Poor	M	0.7 - 0.8	0.56 - 0.69	0.49 - 0.62	0.42 - 0.55	0.35 - 0.48
	F	0.56 - 0.69	0.42 - 0.55	0.35 - 0.48	0.28 - 0.42	0.21 - 0.35
Average	M	0.83 - 0.97	0.7 - 0.8	0.62 - 0.76	0.56 - 0.69	0.49 - 0.62
	F	0.7 - 0.8	0.56 - 0.69	0.49 - 0.62	0.42 - 0.55	0.35 - 0.48
Good	M	0.97 - 1.11	0.83 - 0.97	0.76 - 0.9	0.7 - 0.83	0.62 - 0.76
	F	0.83 - 0.97	0.7 - 0.83	0.62 - 0.76	0.56 - 0.69	0.49 - 0.62
Excellent	M	> 1.11	> 0.97	> 0.9	> 0.83	> 0.76
	F	> 0.97	> 0.83	> 0.76	> 0.7	> 0.63

2.5 Field observations and measurements of rip currents

Six features have been proposed by *Shephard et al.* [1941] to identify rip currents in the field:

1. Sediment laden water indicates the presence of a rip because sediment is transported seawards by the current.
2. The location of the channel is marked by green water where the depth is larger.
3. The foam of the breaking waves is carried offshore beyond the breaker line by the rip current.
4. Choppy water points to locations where currents oppose the incident waves.
5. In the rip channel the waves break closer to the shore and therefore a gap in the breaker line is observed.
6. Floating objects can be used to test if an offshore current is present.

Though none of these characteristics alone is sufficient to prove the presence of a rip current, they all together can give a hint to its existence. In addition to the above mentioned indicators the presence of a rip current can be deduced from a cross pattern in the advancing waves. The incident waves bend towards the rip current due to current refraction and form a cross sea.

The hostile environment of the surf zone complicates the measurement of rip currents in the field. As a result, rip current field data is scarce. The first attempt to demonstrate rip currents

in the field was by *Shephard et al.* [1941] who mapped the drifter paths of floating objects. *Sonu* [1972] again used floating objects. He filled polyethylene balls with water such that they had a neutral density in water and therefore floated within the water column and were not subject to surf events. *Brander* [1999] illustrated the rip current flow patterns with potassium permanganate dye in the near shore zone.

A number of instruments have been used to undertake a quantitative analyse of rip currents in various experiments [*Aagaard et al.*, 1997; *Brander*, 1999; *Brander and Short*, 2000; *Bruneau et al.*, 2009; *Callaghan et al.*, 2004; *Dette et al.*, 1995; *MacMahan et al.*, 2005; *MacMahan et al.*, 2008]. Current meters deployed in cross shore and/or longshore transects provide Eulerian flow measurements and give insight in the temporal variations of rip currents. However, the installation of these instruments in the surf zone is problematic. Furthermore, Eulerian measurements have two limitations. Firstly, current meters at a limited number of positions cannot capture the whole flow pattern. Secondly, the measurements cannot depict the spatial variability of rip currents because they are restricted to predefined locations.

In more recent field studies GPS tracked drifters have been used to obtain a more comprehensive image of the flow patterns in a rip current and to overcome the limitations associated with fixed instrument transects. *Johnson and Pattiaratchi* [2004] developed a drifter with a cylinder that comprises the GPS receiver and that would float at the water surface. To prevent surf events of the drifter on broken waves, two parachutes were attached to it. Another GPS tracked drifter follows the design by *Schmidt et al.* [2003] whereby surf events are avoided by a large floatation depth and a weight that is mounted on the bottom of the floating body. *Brander and Short* [2000] utilised people as human drifters who were tracked with two theodolites from the beach while *MacMahan et al.* [2010] recorded human drifter paths with a GPS mounted to the people's heads.

The results of GPS drifter tracking have shown that floating objects are mainly retained in the surf zone [*Reniers et al.*, 2009]. Observed flow patterns include eddies and meandering long shore currents [*MacMahan et al.*, 2010] and only infrequently is drifting material ejected offshore or washed on the beach.

2.6 Numerical modelling of rip currents

Rip currents are influenced by bathymetry and the hydrodynamic conditions. Several numerical studies have investigated the influence of geometric as well as hydrodynamic parameters on rip current systems in a synthetic environment. *Svendsen et al.* [2000] analysed rip currents on a barred beach with rip channels using the 3D nearshore circulation model SHORECIRC. It was identified that the offshore velocity in the rip channel does not depend on the rip spacing and that the rip has only a limited capacity to draw water from its surroundings. With increasing rip spacing the amount of return flow in form of undertow was shown to increase. The importance of undertow increased with decreasing distance of the bar from the shoreline. Their study suggests that the strongest rips occur with normal incident waves because oblique incident waves generate longshore currents that possess enough inertia to bypass the channel. In contrast, *Voulgaris et al.* [2011] examined the total velocities in the rip channel and found maximum velocities with waves under an angle of 10°.

Numerical simulations have been also performed to reproduce data obtained in the laboratory, in the field and to investigate synthetic cases. *Haller et al.* [2002] measured morphologically controlled rip currents in the laboratory. For this purpose a bathymetry was created that consisted of a sloping bottom with a bar and two incised rip channels. The rips were generated by regular waves of various wave heights and normal incidence. Only one

test was performed with waves under an angle of 10°. Various water levels were also tested. An extensive data set of current velocities, wave heights and water levels was recorded and has been used to verify three rip current numerical models:

The first was performed by *Chen et al.* [1999] who used a fully nonlinear Boussinesq type model to simulate the rip currents measured in the laboratory. It was found that the rip current was accompanied by strong vortices and that the flow oscillated in the channel. It was hypothesised that the instabilities of the current in the channel prevent the rip from extending further offshore. The instabilities were associated with small perturbations in the bathymetry of the wave basin. However, instabilities also occurred in simulations with a nearly perfect symmetric bathymetry, although they emerged later.

With a quasi-three-dimensional model, *Haas et al.* [2003] investigated the influence of bottom friction, wave current interaction and three-dimensional effects on rip current characteristics. Firstly, it was identified that an increase in bottom friction stabilises the location of the rip current in the channel and reduces peak velocities. Secondly, wave current interaction proved to be important to reproduce the meandering of the rip in the channel, which reduces the offshore extent of the rip current. Thirdly, three-dimensional simulations introduce additional dissipation terms next to turbulent mixing, bottom friction and horizontal shear stresses. It was shown that including the three-dimensional dispersive mixing mechanism caused vortices to dissipate quicker and stabilise the flow pattern.

Jacobs [2010] conducted the most recent study and demonstrated that a non-hydrostatic version of XBeach reproduces the experimental results well. The agreement of the modelled and measured data of wave height, water levels and flow velocities was in the order of or better than those predicted in the previous studies [*Chen et al.*, 1999; *Haas et al.*, 2003]. It is noted that a higher grid resolution was used in the XBeach model set-up than in the previous studies.

2.7 Rip current forecast models

Empirical forecast models have been developed in the US as a response to the high number of fatalities along US beaches. The US Lifesaving Association attributes 64 drownings a year to rip currents [*NOAA*, 2011]. *Lushine* [1991] reviewed the Medical Examiner's death records, beach patrol rescue logs and newspapers in Florida (US) and correlated the rip current drownings to wind speed, wind direction, tide and wave height. He discovered that the rip current danger increases with onshore winds, increasing wind speed, decreasing water level and increasing wave height. From these observations he developed the LURCS (LUshine Rip Current Scale) to assess the rip current threat. *Lascody* [1998] adapted the LURCS formula for Daytona Beach and Smyrna Beach and added a factor for wave period. The resultant ECFL (East Central FLorida) LURCS accounts for a larger number of rescues with long period waves. The model was further modified by *Engle* [2003] who discarded the effects of wind, but included the effect of wave angle and directional spreading. He found that a large number of rescues coincides with normal incident waves and narrow banded directional spectra.

The forecast models summarised above have a number of common drawbacks: Firstly, empirical models are biased by beach attendance. Therefore, the individual risk for a swimmer cannot be derived from those models, but only a societal risk. Secondly, the interdependence of the factors (e.g. wind and wave direction, wind and wave height, wave height and wave period) hinders the identification of parameters that affect rip current activity. And thirdly, the importance of the underlying bathymetry is disregarded. The latter was

acknowledged by *Nelko and Dalrymple* [2008] who present a simple model to predict the formation of rip favouring morphology. Wave height and period subsequent to a storm are used to evaluate whether accretion has taken place. Accretion is associated with increased longshore topographic variability and indicates the existence of rip channels. Another approach by *Voulgaris et al.* [2011] involves a process based model. However, the proposed model was a 3D model and computationally expensive. Furthermore, the model was used to investigate a theoretical case and was not validated against field data.

3 Model Evaluation

3.1 Introduction

The numerical model XBeach was applied in this study to simulate rip current flow. XBeach has been developed as a joint effort of UNESCO IHE, Deltares, Delft University of Technology and The University of Miami. The purpose of the model evaluation conducted in this study was to investigate the capabilities and limitations of XBeach with respect to rip current modelling. An overview of the model along with implementation of the wave-current interaction and the roller model in particular are described in Section 3.2.

A schematic barred beach with incised rip channels was modelled in XBeach to determine the suitability of XBeach to model rip currents. A comparison of the results against experimental data [*Haller et al.*, 2002] from the Ocean Engineering Laboratory at the University of Delaware (Section 3.3) was conducted to gain confidence in the model. A sensitivity analysis of the laboratory scale model investigated the importance of two model features: (1) the wave-current interaction and (2) the roller model. Finally, a synthetic model of Egmond aan Zee was built to assess the suitability of XBeach to simulate rip currents in field site scale (Section 3.4). The trends suggested by the synthetic model were compared to results in literature and were also used to formulate hypotheses about rip current activity at Egmond aan Zee. These hypotheses formed the basis for the measurement plan used in the field experiment (Chapter 4).

3.2 XBeach

3.2.1 Model structure

XBeach is a 2DH model that was initially developed to model dune erosion and overwash during storms time dependent and physics based [*Roelvink et al.*, 2009]. It comprises a number of functionalities that are treated in modules. The main modules of interest for this study are the hydrodynamic modules, which are the short wave module and the flow module (Figure 3.1). Morphodynamic processes are included in the model but they are not of interest for this study and therefore not further mentioned here. Within the short wave module, the wave action equation is solved and the wave dissipation is calculated. Optionally wave current interaction can be included. The radiation stress gradients determined from the short wave forcing then serve as an input into the flow module. Within the flow module the shallow water equations are solved. The outputs of the flow module are surface elevations and Generalised Lagrangian Mean (GLM) velocities. If wave current interaction is included, the flow velocities are used to modulate the wave field in the short wave module. The update interval between the two modules is governed by the ‘waveint’ parameter and is expressed as a multiple of the wave period.

For a comprehensive model description the reader is referred to *Roelvink et al.* [2009]. This thesis will only describe the wave-current interaction and the roller model within XBeach in more detail.

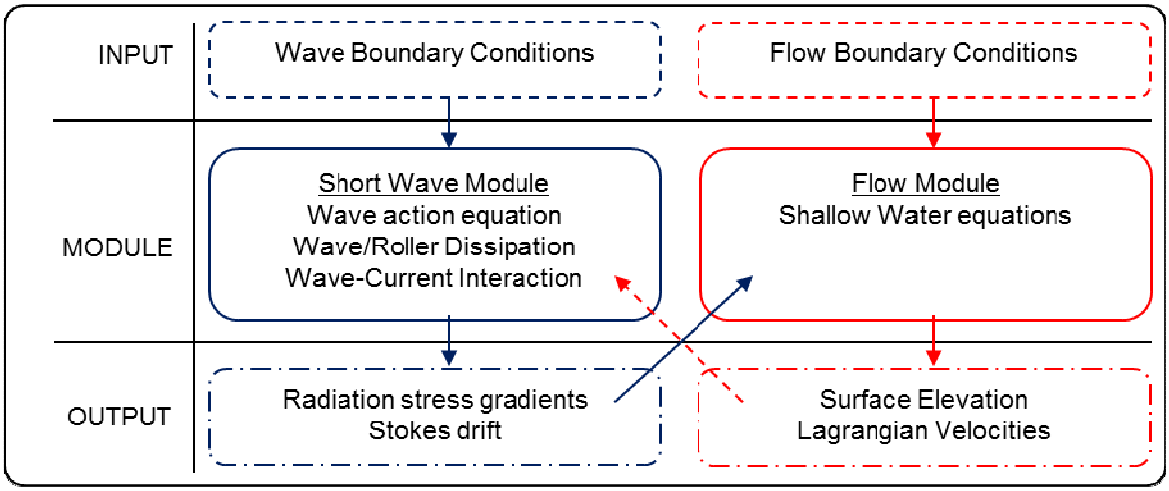

Figure 3.1 Structure of the main hydrodynamic models in XBeach (modified from Daly [2009]). The red dashed arrow is only activated when wave-current interaction is turned on.The model also includes morphodynamic modules, but they are not used in this study and therefore not listed in the model structure.

3.2.2 The importance of wave-current interaction

A change in wave height due to breaking induces currents in the surf zone. The wave-current interaction describes the feedback of these currents on the incoming waves. In the presence of currents, waves can be modified in five ways: (1) refraction, (2) energy bunching, (3) Doppler shifting, (4) an energy transfer between waves and currents [*Holthuijsen*, 2007] and (5) modification of the wave dissipation.

(1) Refraction

Longshore gradients in opposing currents (present in a narrow rip current) force an incoming wave to refract. This is due to part of a wave (subjected to the stronger current) slowing down with respect to the other part of the wave (that is subjected to a weaker current). In XBeach, this effect is accounted for in the formulation of the wave group propagation speed in the θ space:

$$c_\theta(x,y,t,\theta) = \frac{\sigma}{\sinh 2kh}\left(\frac{\partial h}{\partial x}\sin\theta - \frac{\partial h}{\partial y}\cos\theta\right) + \cos\theta\left(\sin\theta\frac{\partial u}{\partial x} - \cos\theta\frac{\partial u}{\partial y}\right) + \sin\theta\left(\sin\theta\frac{\partial v}{\partial x} - \cos\theta\frac{\partial v}{\partial y}\right) \quad (3.1)$$

where the first term on the right hand side accounts for depth induced refraction and the second and third term account for current induced refraction.

(2) Energy bunching

Energy bunching refers to current induced shoaling and is incorporated in the model by using an absolute wave action propagation speed in x and y-direction in the presence of a current. These are given by:

$$c_x = c_g \cos\theta + u^L$$
$$c_y = c_g \sin\theta + v^L \tag{3.2}$$

where u^L and v^L are the depth averaged Lagrangian flow velocities.

(3) Doppler shifting and (4) Energy transfer between waves and currents

When a wave propagates on a current, it does not change its absolute frequency ω from a Lagrangian point of view. But because the wave moves with the current its intrinsic frequency σ is altered from a Eulerian point of view. This modulation is given by:

$$\sigma = \omega - k_x u^L - k_y v^L \tag{3.3}$$

The so-called frequency shifting is accounted for by using the wave action balance (Eq. 3.4) instead of the wave energy balance.

$$\frac{\partial A}{\partial t} + \frac{\partial c_x A}{\partial x} + \frac{\partial c_y A}{\partial y} + \frac{\partial c_\theta A}{\partial \theta} = -\frac{D_w}{\sigma} \tag{3.4}$$

Wave action A is defined as wave energy density S_w in each directional bin divided by the relative frequency:

$$A(x, y, t, \theta) = \frac{S_w(x, y, t, \theta)}{\sigma(x, y, t)} \tag{3.5}$$

Wave action is conservative in the presence of currents while wave energy is not conservative because waves can transfer energy to currents and vice versa.

(5) Wave dissipation

Wave current interaction also affects the wave dissipation D_w. The numerical models in this study are driven by stationary waves for which the wave dissipation formulation is described in this Section. An evaluation of the wave dissipation formulation for in-stationary waves by *Roelvink* [1993] is provided in Appendix A.

For stationary waves, the wave dissipation in XBeach is calculated according to the Baldock formulation [*Baldock et al.*, 1998]. This model is developed for saturated surf zones. This means that an increase in wave energy is immediately compensated for by an increase in wave dissipation and that the local water depth largely controls wave breaking. This assumption is applicable to wide surf zones with steep incident waves. The wave dissipation by *Baldock et al.* [1998] is given by:

$$D_w = \frac{1}{4}\alpha Q_b \rho g f_{rep} \left(H_b^2 + H_{rms}^2 \right) \tag{3.6}$$

with α in the order of 1 and f_{rep} a representative intrinsic frequency. The proportion of breaking waves is estimated by:

$$Q_b = \exp\left[-\left(\frac{H_b^2}{H_{rms}^2}\right)\right] \tag{3.7}$$

The breaking wave height H_b is expressed as a fraction of the local water depth h as follows:

$$H_b = \gamma h \tag{3.8}$$

An empirical formulation by *Ruessink et al.* [2003] is used to determine the breaking parameter γ. The model is non-parametric and solely dependent on the local water depth h and the wave number k:

$$\gamma = 0.76kh + 0.29 \tag{3.9}$$

This formulation was developed for barred beaches and was validated against field data from Egmond aan Zee. The wave height predictions in the inner trough are improved significantly by the use of this formulation when compared to the initial formulation based on the offshore wave steepness [*Battjes and Stive*, 1985]. According to this empirical relation γ increases in the presence of a current because the wave number k increases as a result of current induce shoaling. It is noted that this formulation was intended to improve wave height predictions on a barred beach and was not developed to account for the effect of currents. An adaptation for the wave breaking parameters γ in the presence of currents is not available at present.

Haller et al. [2002] propose that a rip current will shift the type of breaking more towards the plunging regime. This hypothesis is supported by observations in the laboratory in which more intense wave breaking and higher H/h ratios occurred in the presence of a strong rip. This would be consistent with the empirical model by Ruessink et al. [2003] that predicts larger γ in an opposing current. However, present wave dissipation formulations do not readily account for this type of wave breaking.

3.2.3 The Roller model

After a wave is broken the wave bore propagates further as the so-called roller. The roller is sustained by the energy dissipation of the short waves D_w that acts as a sink term in the wave-action equation (3.4). The roller-energy balance is given by:

$$\frac{\partial S_r}{\partial t} + \frac{\partial c_x S_r}{\partial x} + \frac{\partial c_y S_r}{\partial y} + \frac{\partial c_\theta S_r}{\partial \theta} = -D_r + D_w \tag{3.10}$$

where S_r is the roller energy per directional bin. The propagation speeds of the roller in x- and y-direction are given by:

$$\begin{aligned} c_x &= c\cos\theta + u^L \\ c_y &= c\sin\theta + v^L \end{aligned} \tag{3.11}$$

The last terms in equations (3.11) are only taken into account when wave-current interaction is turned on. Rollers and waves are assumed to propagate in the same direction and thus the phase speed of the roller is identical to the one of the short waves:

$$c = \frac{\sigma}{k} \tag{3.12}$$

The total roller energy dissipation D_r is given by [*Reniers et al.*, 2004]:

$$D_r = \frac{2g\beta_r E_r}{c} \tag{3.13}$$

where E_r is the roller energy distributed over all directional bins and β_r is the roller slope coefficient which is in the order of 0.15.

The propagating roller generates turbulent kinetic energy in the boundary layer between the roller and a wave [*Battjes*, 1988]. To capture the energy dissipation due to the increased turbulence the horizontal viscosity is increased locally. In the surf zone, the horizontal viscosity is substituted by the larger roller induced viscosity:

$$\upsilon_h(x,y) = \max\left[\upsilon_{Smag};\upsilon_{roller}\right] \tag{3.14}$$

Where υ_{Smag} is the viscosity due to subgrid turbulence based on Smagorinsky's model. The roller induced viscosity is given by:

$$\upsilon_{roller} = \alpha_{roller} h \left(\frac{D_r}{\rho}\right)^{1/3} \tag{3.15}$$

and α_{roller} is a scale factor which can range between 0 and 1. The default value for this scale factor is 1. A smaller scaling factor reduces the roller induced viscosity.

Breaking waves generate turbulence only locally and thus, the viscosity induced in this context acts predominantly in the vertical and is absorbed at small time scales. XBeach, however, is a depth averaged model and translates the locally induced vertical viscosity into a horizontal viscosity. It is noted that the relation between vertical and horizontal viscosity is complex and requires an advanced model in a physics based approach. In XBeach this relation is simplified and it is assumed that the horizontal viscosity is a fraction of the vertical viscosity that is expressed in the scaling factor α_{roller} .

3.3 Validation against a laboratory experiment

3.3.1 Introduction

An experimental study on bathymetrically controlled rip currents was conducted in the coastal lab at the University of Delaware [*Haller et al.*, 2002]. The results from this experiment were used as a validation case for XBeach in the present study. A hindcast model was set up for Test B, which comprised the most extensive current and wave measurements (Figure 3.2). The results of a calibrated model are presented in Section 3.3.2. A sensitivity analysis (Section 3.3.3) investigated the influence of the key components (the wave-current interaction and the roller model) on the model's capability to simulate rip current flow.

The tests were performed on a linear sloping bottom with a bar that was cut by two rip channels (see also Figure 3.5). The bathymetry used for the simulations was based on the survey results obtained in the laboratory and was projected onto a 10 x 10 cm grid.

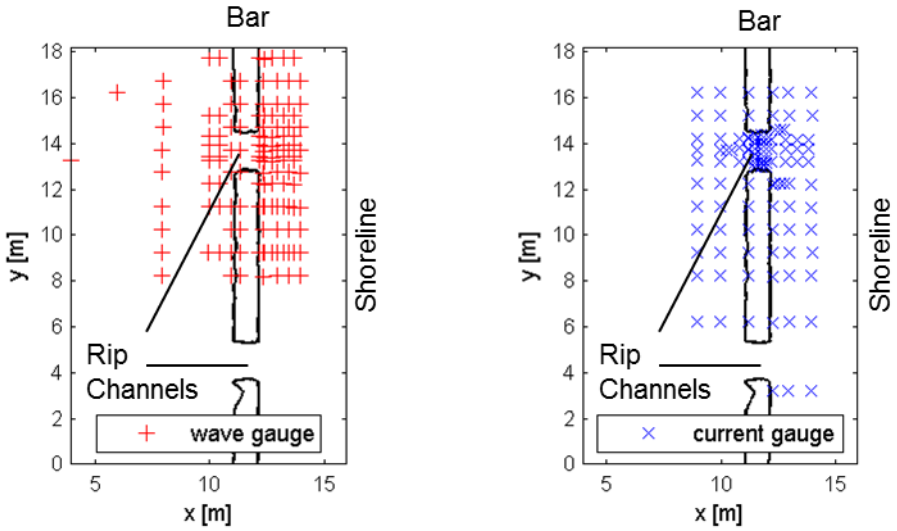

Figure 3.2 Locations of wave gauges (left) and ADVs (right) for test B. In each plot the offshore boundary is on the left and the beach is on the right. The location of the bar is indicated by the black line and the rip channels are each at y = 5 m and y = 13 m.

During this experiment regular stationary waves with a constant water level were tested and resulted in XBeach being driven with constant wave energy so without wave groups. The offshore boundary of the model was set at x = 3.95 m where the most offshore wave gauges were located during the experiment. The wave height measured at the offshore wave gauges was 4.75 cm. All boundaries were 'closed' as there was no water added or withdrawn during the experiment conducted in the laboratory. The simulations were run for 1600 s. To exclude warm-up effects, the results were averaged over the second half of the simulation before they were compared to time and depth averaged measured values.

3.3.2 Results

The best model calibration was achieved when both wave-current interaction and the roller energy balance were turned on. The directional resolution was set to 20°. The viscosity was modelled using the Smagorinsky formulation with a background viscosity of 0.1 and the roller induced viscosity scaled with the factor $\alpha_{roller} = 1$. The wave dissipation was modelled with the Baldock formulation with a spatially varying γ (discussed previously).

The time averaged velocities are presented in Figure 3.3. The flow was not found to be symmetric as one would expect from a symmetric design bathymetry, but the upper rip was notably stronger. This behaviour was also observed during the laboratory experiments and was confirmed in previous modelling studies [*Chen et al.*, 1999; *Haas et al.*, 2003; *Jacobs*, 2010]. The imbalance between the upper and lower rip was attributed to subtle deviations of the real bathymetry from the design bathymetry so that the bar slopes slightly down towards the lower rip. *Haas et al.* [2003] demonstrated that the bias towards the upper rip resulted from this imperfection in the bathymetry. Overall, the flow patterns were well replicated with a

primary circulation in the rip channel and a secondary circulation onshore of the rip, which was more pronounced for the lower rip (Figure 3.3, right).

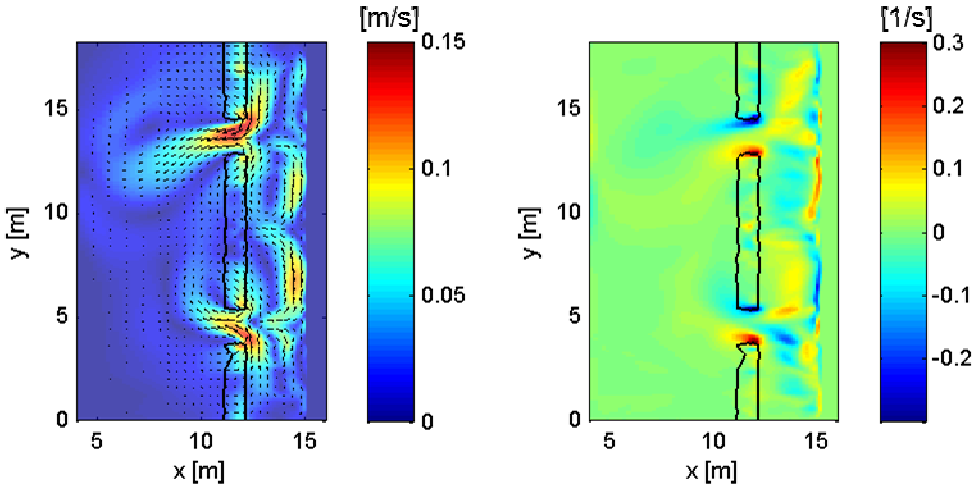

Figure 3.3 Time averaged velocities (left) and vorticity (right) from the XBeach model. Red areas in the vorticity plot on the right indicate counter-clockwise rotating flow and blue areas indicate clockwise rotating flow.

A visual comparison of the measured and computed Eulerian velocities in the upper rip channel was conducted at the points where ADVs were located in the laboratory experiment (Figure 3.4). Both feeder currents exhibited very good agreement in direction and strength with the modelled values. The flow in the centre of the rip channel was also well simulated, although the computed flow directions in the upper part of the channel deviated from those measured in the laboratory experiment.

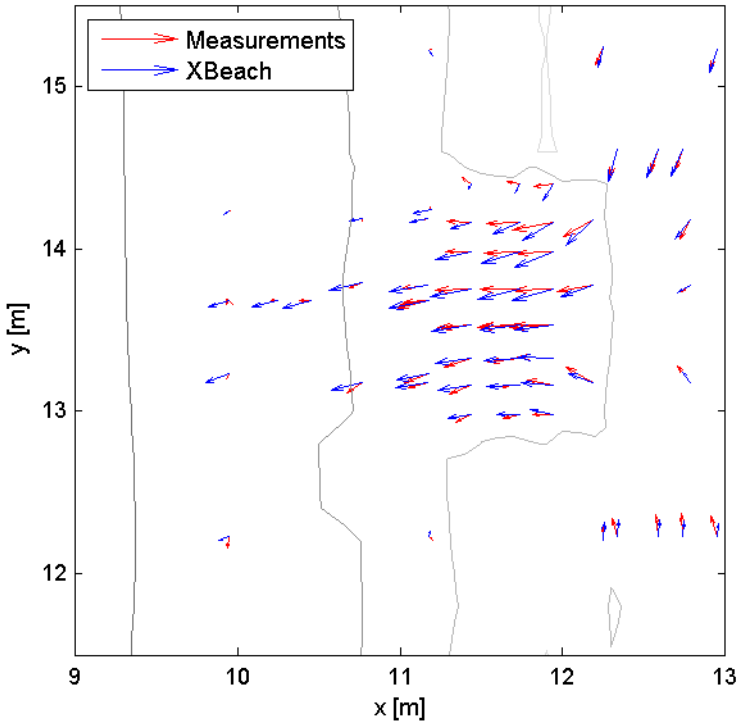

Figure 3.4 Comparison of the time averaged measured velocities and the modelled velocities in the rip channel.

Offshore of the rip the velocities were overestimated by the XBeach model. In a similar experiment *Haas and Svendsen* [2002] demonstrated that the vertical structure of the rip current is nearly depth uniform within the channel, but has a distinct profile offshore with strong offshore velocities near the surface and only weak offshore or even onshore directed velocities near the bottom. During the measurements the ADVs were mounted at a height of 3 cm [*Haller et al.*, 2000] whereas the model results comprised of depth averaged values. It is hypothesised that the rip current flow in the wave tank passed over the top of the ADVs offshore of the channel. As a consequence, the laboratory measurements cannot be compared to the depth averaged results produced by the model simulations in the region offshore of the channel. The impact of the vertical velocity profile on rip current modelling is discussed in more detail in Section 6.4.

For the assessment of the model skill, Willmott's index of agreement d [*Willmott et al.*, 1985] was selected to enable comparison with previous modelling studies based on this experiment [*Chen et al.*, 1999; *Haas et al.*, 2003; *Jacobs*, 2010]. This model skill score is defined as

$$d = 1 - \frac{\sum_{i=1}^{n} \left(x_c(i) - x_m(i) \right)^2}{\sum_{i=1}^{n} \left(\left| x_c(i) - \overline{x}_m \right| + \left| x_m(i) - \overline{x}_m \right| \right)^2} \tag{3.16}$$

where x_c are the computed values, x_m are the measured values and $\overline{x}_m$ is the mean of the measured values. A model skill of 1 indicates prefect agreement. All points available from the measurements were used to calculate the indices of agreement which are presented in Table 3.1 along with the model skills of previous hindcasts of the laboratory experiment. Graphical comparisons of the modelled and measured quantities in alongshore transects (Figure 3.5) are presented in Figure 3.6 to Figure 3.9.

Table 3.1 Willmott's indices of model agreement: d_H for wave heights, d_{zs} for water levels, d_u for cross-shore velocities, d_v for longshore velocities

Model	d_H	d_{z_s}	d_u	d_v
2D hydrostatic (present study)	0.95	0.92	0.92	0.86
Boussinesq [*Chen et al.*, 1999]	0.97	0.98	0.92	0.86
Quasi 3D [*Haas et al.*, 2003]	0.96	0.96	0.92	0.80
2D non-hydrostatic [*Jacobs*, 2010]	0.95	0.98	0.95	0.88

Figure 3.5 Bathymetry of the lab experiment showing the transects where XBeach results for wave height and water level (red) and for velocities (blue) are extracted.

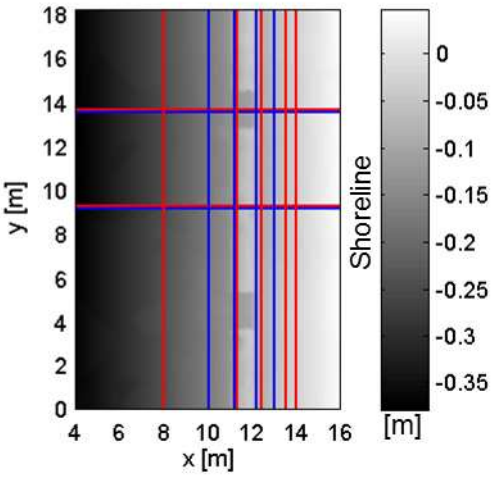

The simulated wave heights are shown along with the measurements in Figure 3.6. Just onshore of the bar (x = 12.4 m) the model reproduced the reduction of wave height over the bar well. The increase in wave height in the channel (same alongshore transect) was also

simulated well although the maximum wave height in the channel was underestimated. The wave heights were only slightly overestimated offshore of the bar (x = 8 m) and slightly underestimated in the feeder channel (x = 14 m). The water levels (Figure 3.7) were predicted fairly well in all alongshore transects apart from the alongshore transect just onshore of the bar (x = 12.4 m) where the water level was underestimated. This was attributed to the wave height in this transect being slightly overestimated, i.e. the modelled amount of wave dissipation was less and thus, the water level set-up was also less (see Section 2.2). The offshore velocities in the rip channel (Figure 3.8, x = 11.2 and 12.2 m) were in good agreement with the measurements. Only in the feeder channels (x = 13 and 14 m) the modelled cross-shore velocities deviated from the measured values. As discussed above the offshore velocities in the rip current offshore of the channel (x = 10 m) were overestimated due to the specific vertical flow structure. The alongshore directed feeder currents in the model (Figure 3.9, x = 12.2 m) represented the flow towards the rip channel well and were in good agreement with the measurements. The reversed flow direction of the second circulation cell (x = 14 m) was also captured in the model although the velocity magnitude was simulated less accurate onshore of the bar (x = 13 and 14 m).

A striking result that was not expressed in the time averaged results is that the rip was very stable and did not meander or pulsate as observed in the experiment [*Haller and Dalrymple*, 2001]. Such meanders and pulsations were however captured in the numerical models previously discussed. Dynamic rip current behaviour in this model was only achieved when the roller induced viscosity was reduced (α_{roller} < 0.2) and thus deviated significantly from the default value of 1.

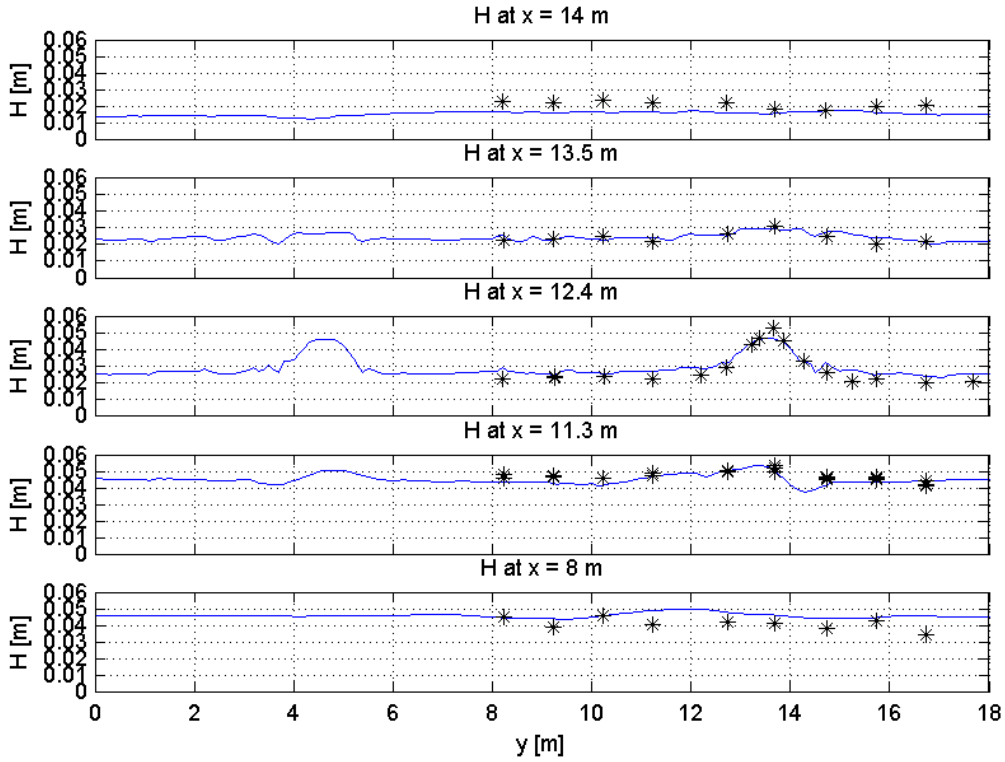

Figure 3.6 Alongshore transects of modelled wave height (blue) with the reference settings are compared to measured wave height (asterisks).

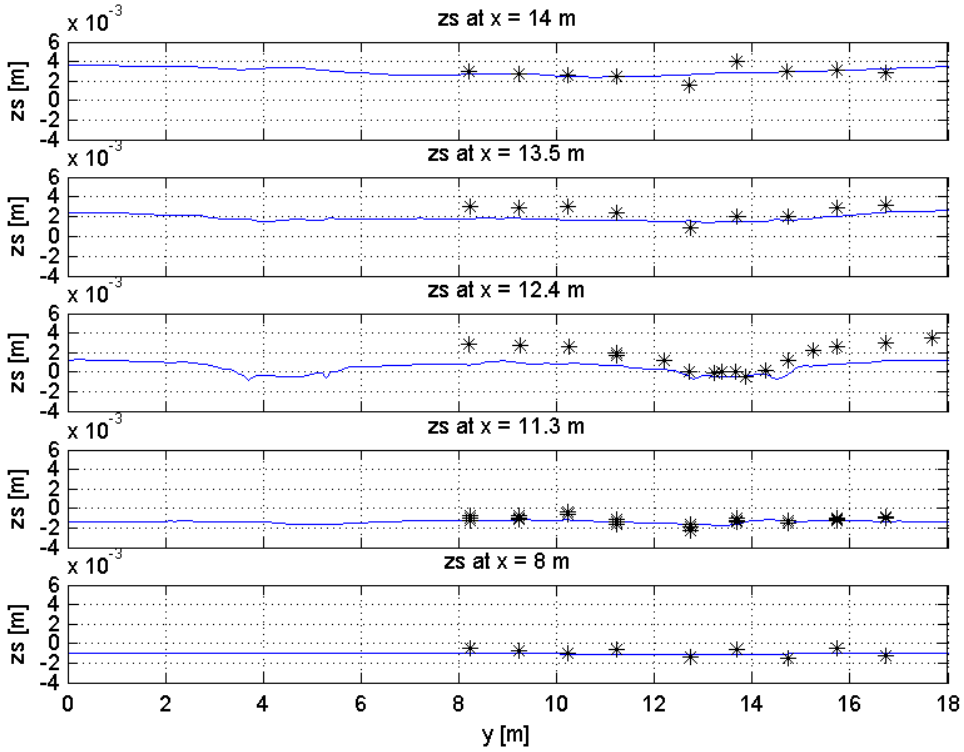

Figure 3.7 Alongshore transects of modelled water level (blue) with the reference settings are compared to measured water levels (asterisks).

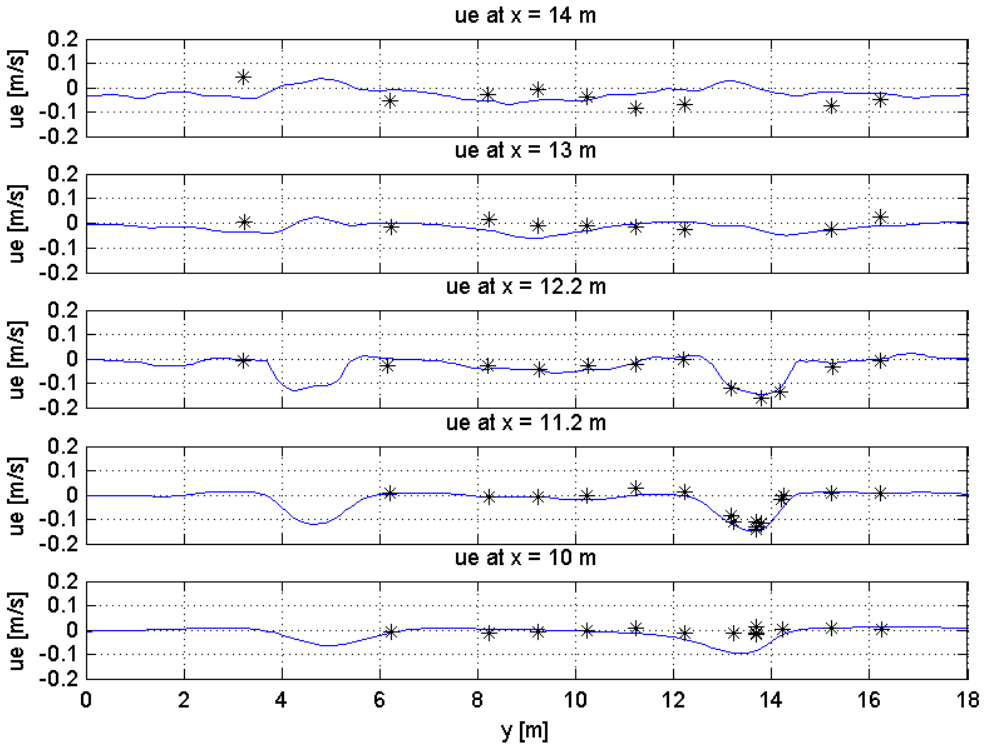

Figure 3.8 Alongshore transects of modelled Eulerian cross-shore velocity (blue) with the reference settings are compared to measured cross-shore velocities (asterisks).Negative values represent offshore velocities.

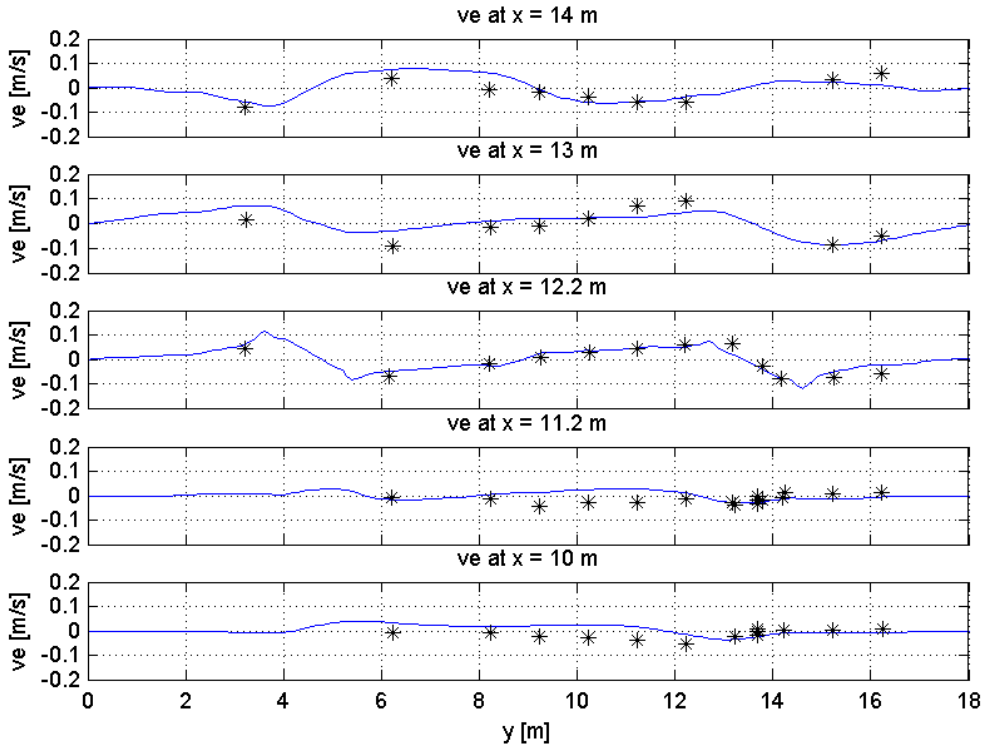

Figure 3.9 Alongshore transects of modelled Eulerian alongshore velocity (blue) with the reference settings are compared to measured alongshore velocities (asterisks).

3.3.3 Sensitivity analysis

The sensitivity of the model to the wave-current interaction and the roller model was investigated. The results of the sensitivity analysis are plotted along either longshore or cross-shore transects through the rip channel and the bar (Figure 3.5).

Wave-current interaction

Wave-current interaction was identified to be an important feature to correctly model rip currents. Figure 3.10 depicts the cross-shore wave height evolution with and without wave-current interaction over the bar and in the rip channel. Over the bar, the results indicated only a small difference with and without wave-current interaction and are in good agreement with the measurements (solid lines and crosses). But in the rip channel, where the current opposes the incoming wave field, the results differed significantly (dashed lines and circles). This was due to current induced refraction and shoaling that increased the wave height offshore of the break point. The wave height decay commenced later and was much more rapid for wave-current interaction cases. The inaccuracies associated with the absence of wave-current interaction were found to have implications on the water level set up and resultant currents. With wave-current interaction waves were larger due to current induced shoaling and induced a water level set-down (Section 2.2) that enhanced the offshore directed flow (Figure 3.11).

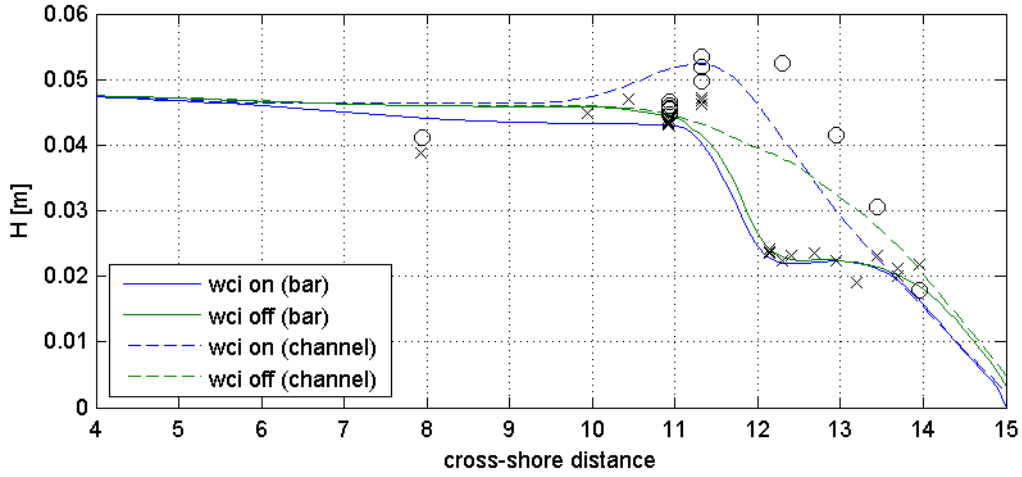

Figure 3.10 Cross-shore transect of modelled wave height with wave current interaction (blue) and without (green) over the bar (solid line) and in the rip channel (dashed line) and the experimental data over the bar (crosses) and in the rip channel (circles).

Although wave-current interaction improved the modelled cross-shore wave height evolution significantly, a limitation of this model component was identified. The increase in wave height and wave breaking was initiated further offshore than measured in the experiment (Figure 3.10). Because wave breaking commences further offshore a wave forcing is induced that counteracts the rip current (Section 2.2). As a result the model did not reproduce the maximum offshore velocities in the rip channel accurately. The overestimation of the currents offshore of the rip channel may be due to the low position of the ADVs in the water column addressed in Section 3.3.2.

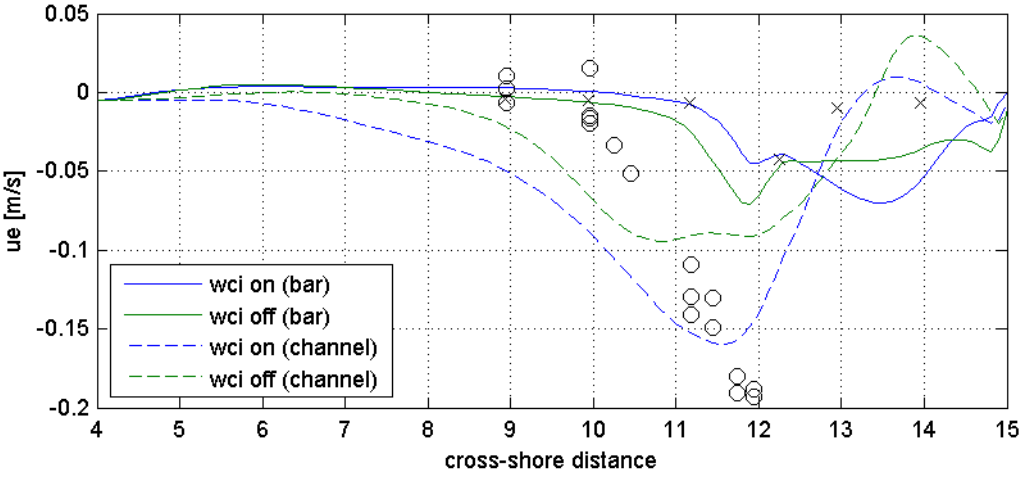

Figure 3.11 Cross-shore transect of modelled Eulerian cross-shore velocity with wave current interaction (blue) and without (green) over the bar (solid line) and in the rip channel (dashed line) and the experimental data over the bar (crosses) and in the rip channel (circles).

To use wave-current interaction effectively in the model, the directional resolution has to be sufficiently large. To examine this effect, simulations without directional resolution

($d\theta = 170°$) and with directional resolution ($d\theta = 20°$) were performed with the results presented in Figure 3.12.

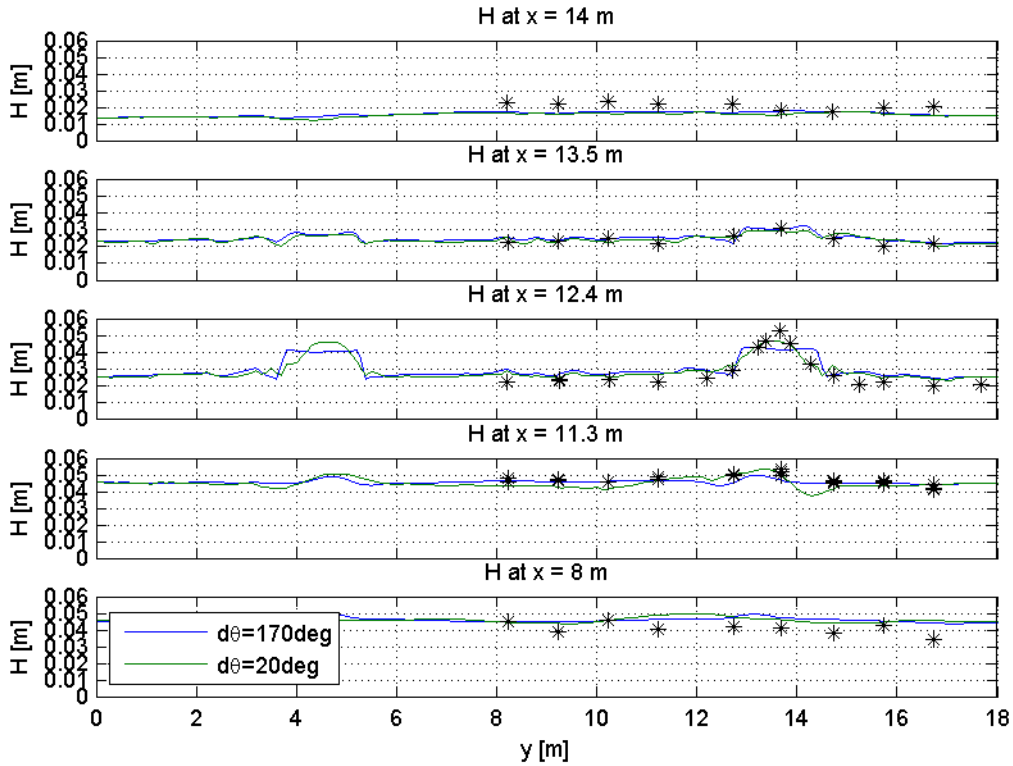

Figure 3.12 Alongshore transect of modelled wave height without directional resolution (blue) and with a directional resolution of dθ = 20°(green) at x = 14, 13.5, 12.4, 11.3 and 8 m (from onshore to offshore) and the measured wave height (asterisks).

Far onshore and offshore of the channel, the directional resolution had no influence on the modelled wave height. But in the rip neck at x = 12.4 m a resolution of $d\theta = 20°$ produced a smoother cross-shore wave height distribution that agreed well with the measurements. Sufficient spatial resolution ($d\theta = 20°$) was crucial in the model to account for the current induced refraction. The opposing current caused the waves to refract towards the centre of the channel and the wave height there to be amplified.

The roller model

As shown in Section 3.2.3 the roller model mainly modifies the viscosity in the surf zone. A change in viscosity did not affect the time averaged results, but had a significant impact on the dynamic behaviour of the rip current. Without the roller model the viscosity is governed throughout the whole domain by the Smagorinsky viscosity model. But a roller model with α_{roller} = 1 increased the viscosity in the surf zone because the rollers induced turbulence as they dissipate in the model. The larger viscosity smoothed the velocity field and dampened fluctuations and oscillations of the rip current (Figure 3.13, lower panel) while the model without the roller energy balance showed a strong dynamic behaviour and triggered vortex shedding (Figure 3.13, upper panel).

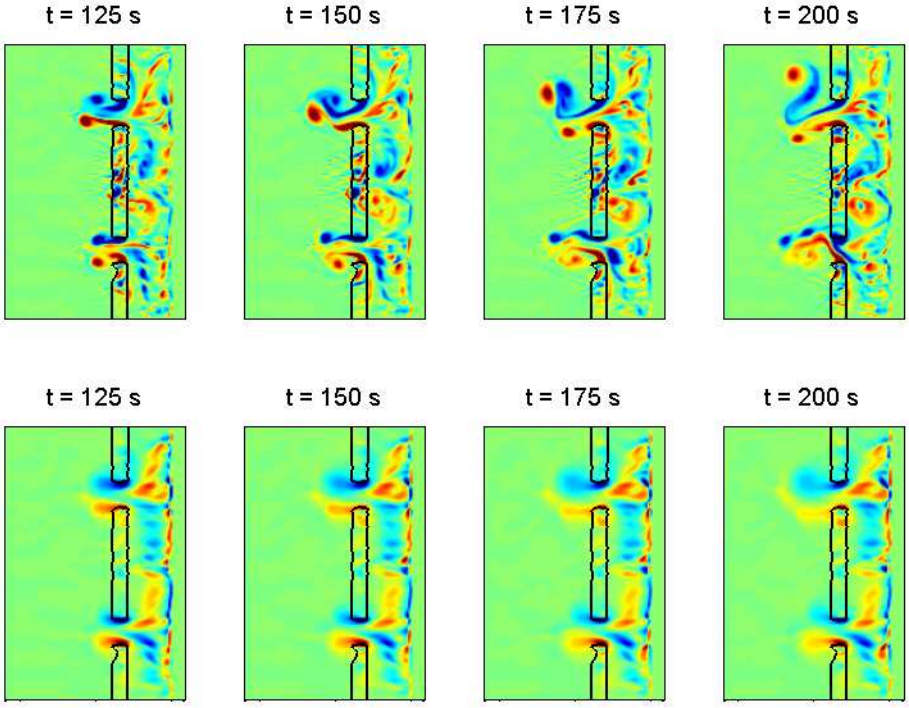

Figure 3.13 Snapshots of vorticity after 125, 150, 175 and 200 s of simulation time without roller-energy balance (top) and with roller-energy balance using α_{roller} = 1 (bottom)

Likewise the dynamic behaviour of the rip current was favoured by reducing the scale factor α_{roller} (Figure 3.14). The default value for this scale value is 1, but the frequencies of the velocity fluctuations in the rip agree better with the measured rip behaviour for $\alpha_{roller} < 0.2$, but the amplitude of these fluctuations remains underestimated with all values of α_{roller} .

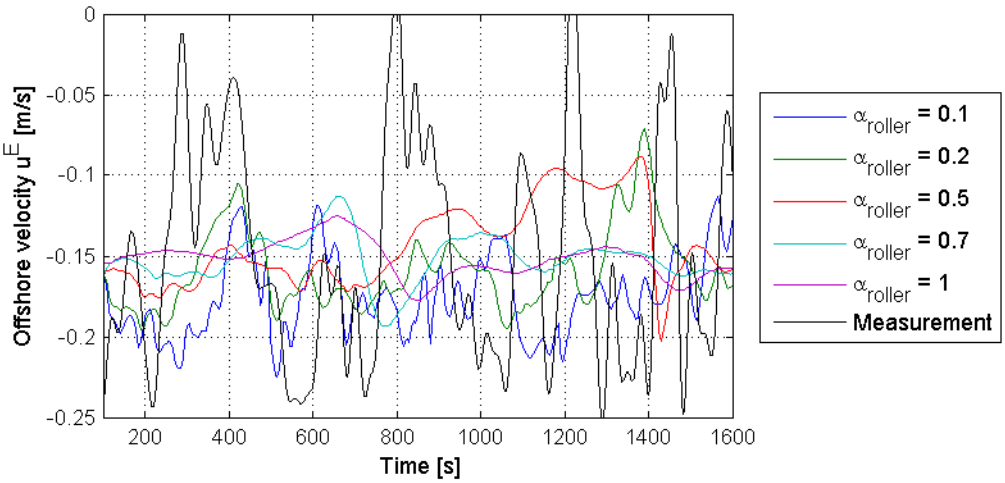

Figure 3.14 Time series of the modelled Eulerian cross-shore velocity in the rip at x = 11.4 m and y = 13.6 m with α_{roller} ranging from 0.1 to 1 (colours). The measured velocity time series (black) was low-pass filtered with a cut-off frequency of 0.03 Hz to be consistent with previous data analysis on this experiment [Haas, 2012; Haas et al., 2003].

It is acknowledged that viscosity is scale dependent and thus the roller induced viscosity may have a different effect in a larger scale model. Therefore, the roller model is not calibrated against the laboratory experiment and is reconsidered in Chapter 6.

3.3.4 Conclusions

It was shown that the 2D hydrostatic XBeach model replicated the laboratory experimental results well. The model skills were in the same order as the results obtained with a Boussinesq type model [*Chen et al.*, 1999], a quasi 3D model [*Haas et al.*, 2003] and a non-hydrostatic version of XBeach [*Jacobs*, 2010]. However, the simplicity of the 2D hydrostatic model allowed for shorter run times and was therefore better suited for an operational forecast model. One should keep in mind that primarily time averaged properties of the rip current were tested. The dynamic behaviour that was reproduced was less accurate than the results of the above mentioned numerical models.

The following model properties were found to play a key role in the numerical simulation of rip currents and were applied in the subsequent models associated with this study:

- Wave current interaction is crucial to the accurate simulation of the shoaling and refraction of the incoming waves due to an opposing rip current. Prediction of the wave height in the rip channel is important to correctly estimate rip current velocity. However, the cross-shore wave height evolution in the rip channel was not found to match the measurements exactly as wave breaking commenced too far offshore and the breaking wave height was underestimated. This resulted in smaller rip current velocities than those measured.
- In combination with wave-current interaction the directional resolution must be sufficiently high to capture wave refraction towards the rip channel. A resolution of $d\theta = 20^\circ$ was determined to be sufficient on basis of the model validation presented here.
- The dynamic behaviour of the simulated rip current is very sensitive to the roller induced viscosity. However, this aspect was not further examined in this context because viscosity is scale dependent and may have a different effect in a large scale model. Therefore, it will be re-examined in Chapter 6 on the basis of the hindcast model of the field measurements.

The capability of XBeach to simulate rip currents has been tested with stationary waves. While it is acknowledged that rip current fluctuations triggered by wave groups [*MacMahan et al.*, 2004] are disregarded in this approach, this simplification was considered acceptable within the aims of the study. The mean rip current properties that were important for this study are replicated well with the present model.

3.4 Numerical study of a synthetic model of Egmond aan Zee

3.4.1 Introduction

A site scale model of Egmond aan Zee was set up and the results were compared to rip current characteristics described in literature. The model is intended to demonstrate the sensitivity of site scale rip currents to various hydrodynamic conditions. The results of this model were compared against rip current behaviour described in literature. Along with the literature the results presented at the end of this chapter were used to formulate hypotheses about rip current activity at Egmond aan Zee. Based on these hypotheses the measurement campaign was planned. The specific results of the various hydrodynamic conditions are

discussed in Chapter 7 in the context of the Egmond XBeach model while only the trends are considered in the present chapter.

3.4.2 Model set-up

A bathymetry of Egmond aan Zee with a high enough resolution to reveal rip channels on the inner bar was not available prior to the field campaign. Therefore, an idealised bathymetry was designed based on the JARKUS (JAaRlijkse KUStmetingen) profile at km 38 from 2010 (Figure 3.15). JARKUS beach profiles are measured yearly along the Dutch coast at intervals of 250 m.

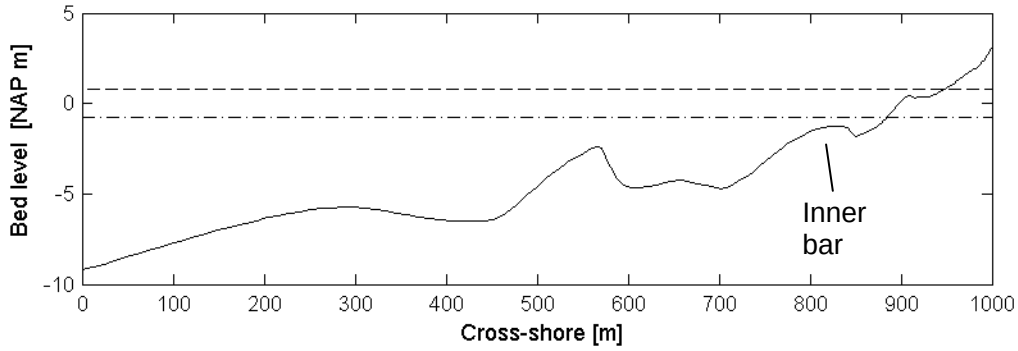

Figure 3.15 JARKUS profile at km 38 from 2010: The dashed line indicates the mean high water level and the lower line indicates the mean low water level.

The JARKUS profile was extended in the longshore direction and a rip channel of 1 m depth and 60 m width was superimposed on the inner surf zone bar (Figure 3.16). The adopted channel depth represents a typical value for rip channels observed at Egmond aan Zee by the lifeguards and reported by *Reintjes* [2002]. Mean low and high tide water levels are NAP ±0.8 m (Normaal Amsterdam Peil).

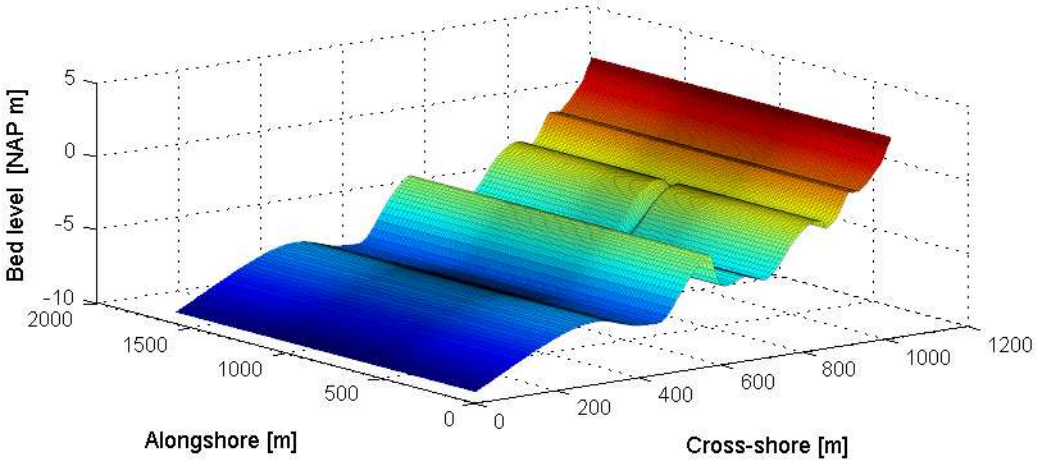

Figure 3.16 Idealised bathymetry of Egmond aan Zee on the basis of the JARKUS profile from 2010 with a superimposed rip channel

Summer wave conditions on the Northern Dutch coast were analysed for the years 2001 to 2010 to determine typical combinations of wave height and period as well as wave height and angle (Figure 3.17). Wave heights range from 0.5 to 1 m with a corresponding peak period of

5 to 6 s. These conditions deviated slightly from an all year average because large wave heights and long periods are less probable during summer months. The predominant wave directions were South West (240°) and North West (315° to 330°) and are consistent with yearly averages.

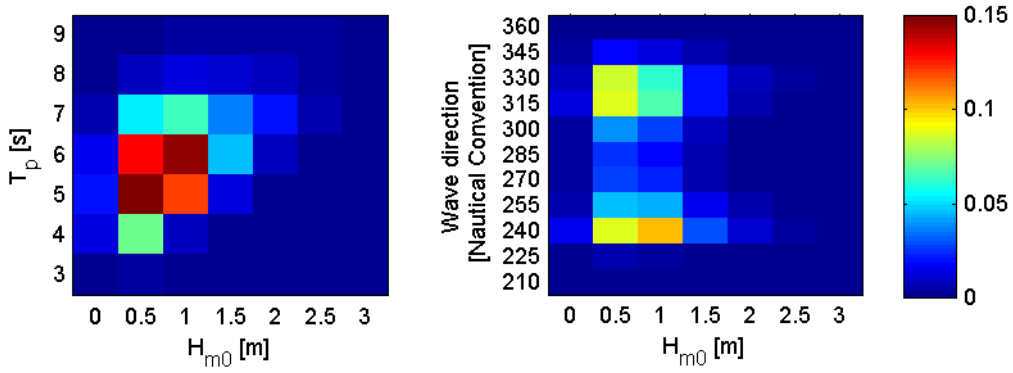

Figure 3.17 Joint probability of wave height and period (left) and for wave height and wave direction (right) for the summer months June, July and August in the years 2001 to 2010.

Stationary waves were applied at the offshore boundaries because their applicability for an accurate prediction of the flow within the rip channel was demonstrated in Section 3.3. The parameters that were tested in the synthetic case study are presented in Table 2.1.

Table 3.2 Parameters that were tested in the synthetic model of Egmond:

Parameter	*Min*	*Step Size*	*Max*
Wave height H_{m0}	0.5 m	0.5 m	2 m
Peak period T_p	4 s	1 s	8 s
Wave angle θ_0 (with shore normal)	0°	10°	50°
Water level	-1 m	0.5 m	+1 m

3.4.3 Methods

In the simulations the drifter option in XBeach was applied (see Figure 3.19) to imitate measurement methods used in the field experiment (see Section 4.3.1). The rip strength was used to compare the modelling results and was defined by the drifter velocities in the rip neck. The drifters in XBeach float with the Generalised Lagrangian Mean (GLM) velocity. The GLM velocity u^L is a measure for the velocities observed at the surface and is defined as the sum of the Eulerian velocity u^E and the Stokes drift:

$$u^L = u^E + u^S \tag{3.17}$$

The implications of this velocity definition for rip current modelling are addressed in Section 6.4. The maximum offshore directed velocity component of each drifter was determined and then averaged over the whole simulation yielded the rip strength. This definition has two advantages. Firstly, simulations have shown that the drifters became concentrated in areas with strong flow velocities. Thus, the strongest flow velocities were captured even for obliquely incident waves and when the strongest offshore flow deviated from the centre line of the rip channel. Secondly, this definition could be applied to the field results where only drifter

data was collected. This enabled the same approach to calculate the rip strength to be used throughout the study.

Calculations with different numbers of drifters showed that the Lagrangian approach was insensitive to the number of drifters used (Figure 3.18). The maximum number of drifters that were used in this approach was 50. The rip strength obtained from 50 drifters was compared to values calculated from 5, 10 and 20 drifters. The amount was reduced by choosing random drifters out of a normal distribution around the rip channel. However, it should be noted that the Lagrangian approach will be more sensitive to the number of drifters when it is applied to a rip that incorporates spatial and temporal fluctuations.

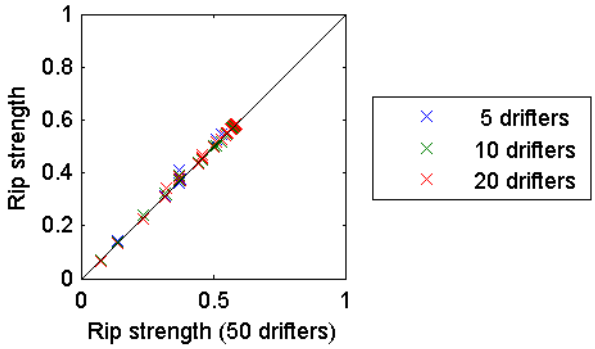

Figure 3.18 Sensitivity of the Lagrangian approach to the number of drifters used. On the x-axis is the rip strength calculated from 50 drifters and on the y-axis calculated from 5, 10 and 20 drifters respectively.

3.4.4 Results

The basic test case was composed of a wave height H_{m0} = 1 m, wave period T_p = 5 s, wave angle θ = 270° (shore normal) and water level NAP +0 m and produced a straight offshore directed rip current that was fed from both feeder currents (Figure 3.19).

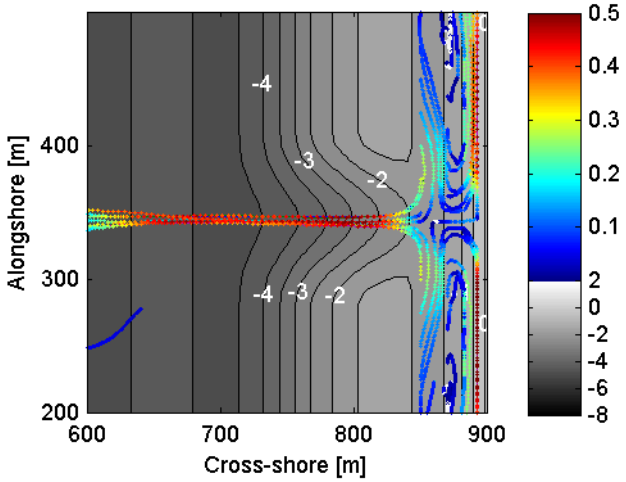

Figure 3.19 Simulated drifter paths for the basic test case with H_{m0} = 1 m, T_p = 5 s, θ = 270° (shore normal) and η = 0 m. The colours indicate drifter velocities and the underlying bathymetry is plotted in grey. The rip is directed offshore and is fed by the upper and lower feeder channel.

Subsequently, wave height, water level, wave period and wave angle were altered according to Table 2.1. The results of this sensitivity analysis are presented in Figure 3.20.

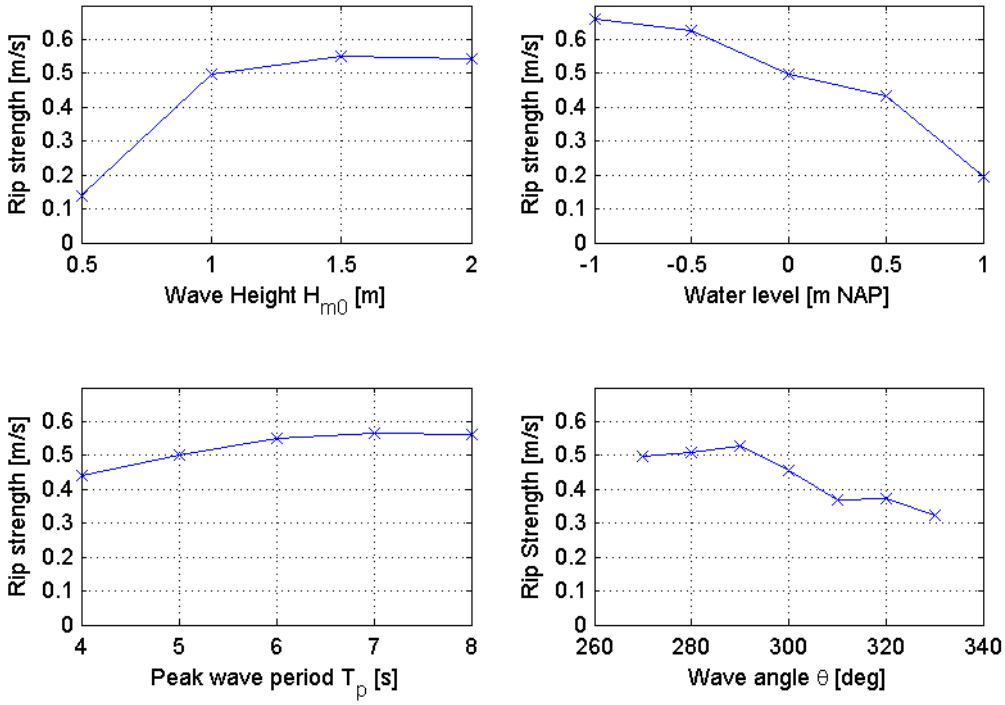

Figure 3.20 From top left to bottom right: Rip strength vs. offshore wave height Hm0, water level, wave period and wave angle. An angle 270° represents shore normal waves.

The rip strength was enhanced with increasing wave height (upper left panel) and decreasing water level (upper right panel). This is consistent with numerous field observations described in literature [*Aagaard et al.*, 1997; *Austin et al.*, 2010; *Brander and Short*, 2000; *De Zeeuw*, 2011; *MacMahan et al.*, 2005; *Sonu*, 1972]. The rip strength does not increase linearly with the wave height, but levels off at around 0.55 m/s. A slight increase of the rip strength was also observed with larger periods. The impact of the wave period was less distinct than the effects of wave height and water level. The offshore velocity was largest for waves under an angle of 20° and decreased rapidly angles larger than 20°. An enhancement of the rip current for small angles of incidence (≤ 10°) was also shown by *Kumar et al.* [2011]. The results of a vanishing rip current for large angles of wave incidence are reinforced by studies by *Svendsen et al.* [2000] and *Kumar et al.* [2011].

3.4.5 Conclusions

The synthetic case study of Egmond aan Zee demonstrated that XBeach is capable of simulating rip currents on a barred beach with site scale dimensions. The effect of various hydrodynamic parameters (wave height, water level, wave period and wave angle) along with previous field observations described in literature were used to constitute the following hypotheses:

The rip strength

- increases with increasing wave height;
- increases with decreasing water level;

- increases slightly with increasing wave period; and
- has its maximum with small angles of wave incidence (10° to 20° with respect to the shore normal) and decays rapidly with larger wave angles.

Interestingly, the surf lifeguards at Egmond aan Zee experienced the strongest rips not with low tide, but just after low water with rising tide. Further they did not observe wave directions that particularly favoured the generation of rip currents. The reasons for this discrepancy are examined in Chapter 7.

The hypotheses along with the experiences of the lifeguards were used to set up a measurement plan for the field campaign that is presented in Section 4.3.

4 Field Study

4.1 Introduction

In August 2011 (yeardays 234 – 238), a five day field experiment SEAREX (Swimmer safety in Egmond aan Zee – A Rip current Experiment) was conducted at Egmond aan zee. The aim of the experiment was to obtain a data set of rip current events. This data was analysed to understand the characteristics and generation of rip currents at Egmond aan Zee and to validate a numerical model. The measurements were performed at two distinct rip channels in the first sub-tidal bar (Figure 4.1). This chapter describes the field site, the field methods and the results. A detailed analysis of the Lagrangian drifter measurements follows in Chapter 5.

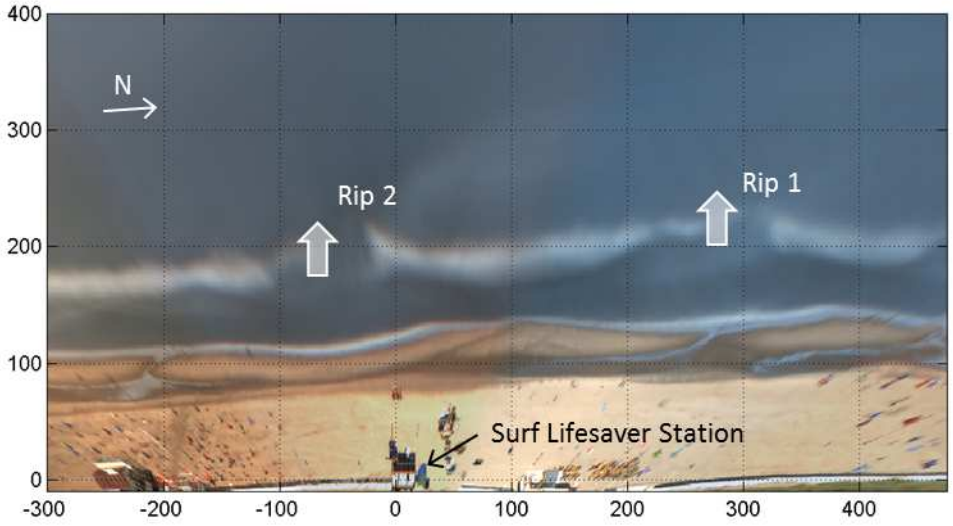

Figure 4.1 Argus plan view of the field site: The Northern (Rip 1) and Southern (Rip 2) rip channel are indicated.

4.2 Study Site

4.2.1 Situation

Egmond aan Zee is located in the province of Northern Holland at coastal km 38. The beach at Egmond is fronted (on average) by three bars, a swash bar in the inter-tidal zone and two bars in the sub-tidal zone. The trough between the swash and the inner surf zone bar is approximately NAP -2 m deep and the trough seaward of the inner bar is up to 5 m deep. The outer bar is located 300 m offshore of the inner bar with a crest level of approximately 3 m below NAP +0 m [*van Duin et al.*, 2004]. Occasionally, a bar shifting is observed [*Reintjes*, 2002], which means that a bar welds towards the beach and the former outer bar then becomes the inner bar. On a large scale the coast can be assumed longshore uniform, however on a smaller scale the coast is characterised by longshore irregularities. The outer bar is broken only by widely spaced rips while the inner bar is highly rhythmic with a rip current spacing of ca. 500 m [*Short*, 1992]. The rip channels on the inner bar are on average 1 m deep [*Reintjes*, 2002].

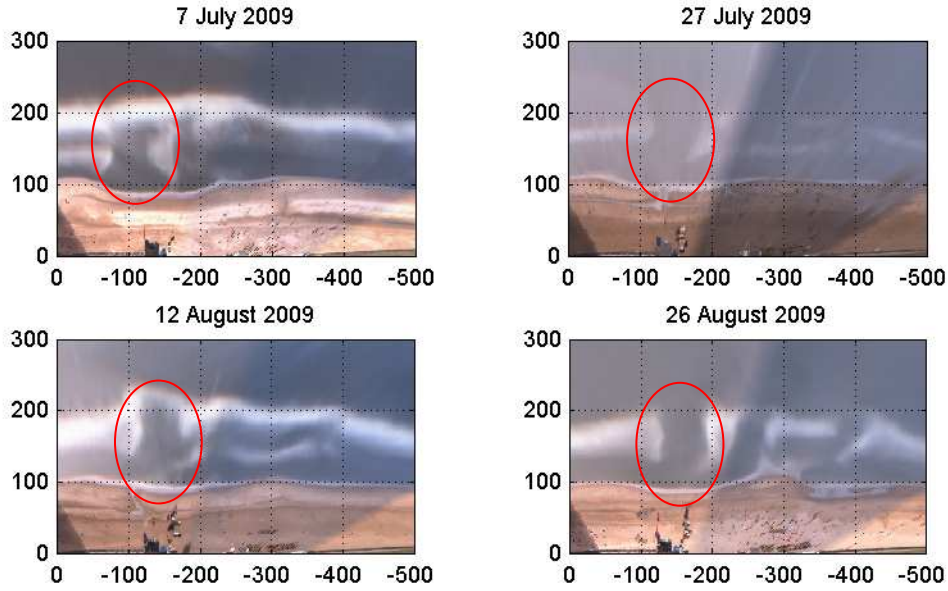

Figure 4.2 Rip location during summer 2009: The rip channel on the left hand side of the picture (red ellipse) is persistent in its location and only migrates slowly along the beach in the period of 7 weeks displayed in the figure.

The study site is situated in a meso-tidal environment with a tidal range in the order of 2 m and strong tidal longshore currents. The wave climate is wind-sea dominated with a modal wave height of 1 m height and 5 s period. During summer the waves are generally low and do not vary considerably. Autumn is a transition period when wave height and variance increase. The winter period is characterised by higher storm intensities with larger waves [*Short*, 1992]. During the calm summer months rip channels stabilise and gradually deepen so that they are usually well defined by the end of summer (Figure 4.2).

4.2.2 Recent nourishment practice

Egmond aan Zee is one of the so-called erosion hot spots along the Dutch coast. This means that the shoreline cannot be maintained at its position of 1990 without regular sand nourishments. Therefore, the Dutch policy is to nourish the beaches that are threatened by structural erosion on a regular basis. The last maintenance work at Egmond aan Zee was performed as a beach nourishment between km 37 and 39 in March 2011 (Figure 4.3). The beach nourishment was carried out along with a shore face nourishment from km 31 to 40 which was completed in August 2011.

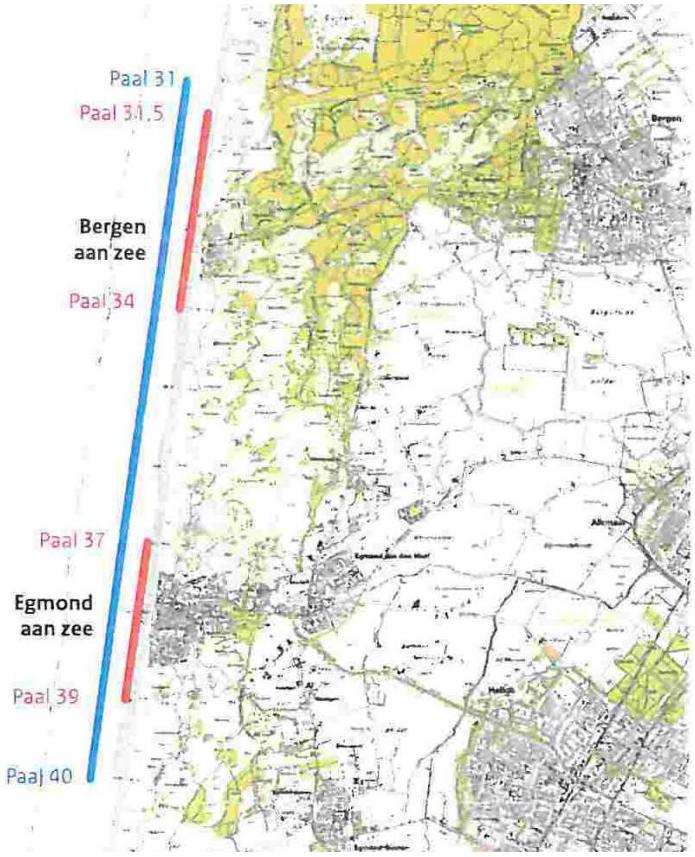

Figure 4.3 Location of the beach nourishments from km 37 to 39 in Egmond (red) and the shore face nourishment from km 31 to 40 (blue) [Rijkswaterstaat, 2011]. The field site is located at km 38.

4.3 Methods

4.3.1 Instruments

The field campaign was conducted at the end of summer when rip channels are usually most developed. Lagrangian velocities in the surf zone were measured with drifter instruments that were similar to the design by *Schmidt et al.* [2003] (Figure 4.6). Following from the hypotheses over rip current activity (see Section 3.4) the experiments were performed with water levels below NAP +0 m (Normaal Amsterdam Peil) only. To distinguish regions of different flow intensities, the drifters were deployed in matrices consisting of two drifter rows either in alongshore or cross-shore direction (Figure 4.5). The drifters were deployed in cross-shore arrays when the updrift feeder was dominating (Figure 4.4).

Figure 4.4 Drifter deployment in two cross-shore arrays. Picture by: www.muien.nl (2011, Willem Verbeek)

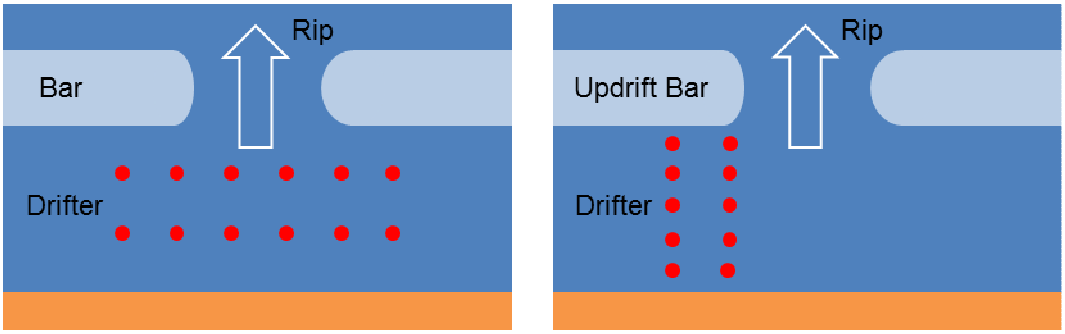

Figure 4.5 Drifter deplyoemnts in alongshore arrays (left) and cross-shore arrays (right).

Throughout the field experiment six measurement sessions were conducted under various wave, wind and tidal conditions. During each deployment up to 12 drifters were released in the surf zone. The deployments were repeated four to five times per session. Drifters were retrieved when they either grounded on the bar or reached a stationary state of drifting shore parallel. In addition to the drifter instruments, human drifters were equipped with the same GPS units on August 24, 25 and 26.

Figure 4.6 Drifter instruments and a volunteer. Picture by: www.muien.nl (2011, Willem Verbeek)

Offshore wave data was recorded by a directional wave rider buoy (instrument 011) offshore of Petten that is installed at a water depth of 19.9 m. The instrument is located 21 km North and 8.3 km offshore of the field site (Figure 4.7). The instrument samples with a frequency of 1.3 Hz. The spectral analysis is performed with an integral ranging from 0.03 Hz to 0.5 Hz and output is produced every 20 min.

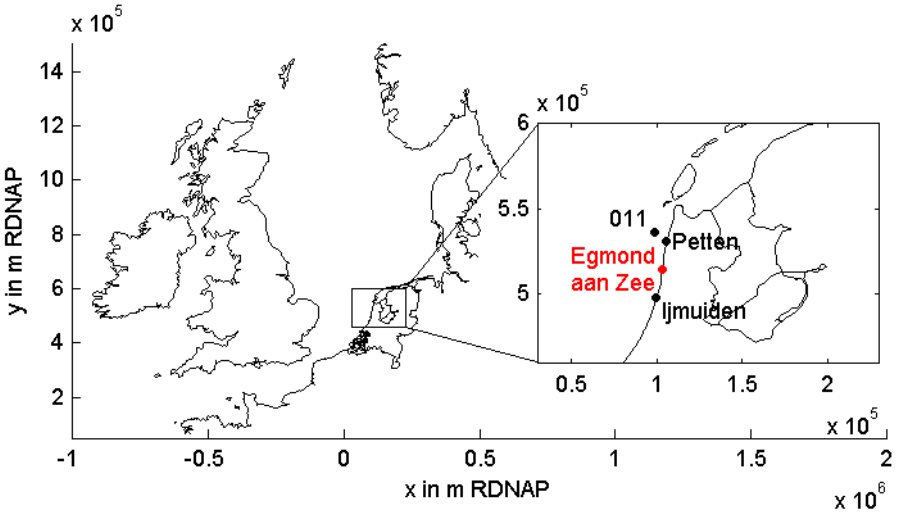

Figure 4.7: Location of the field site Egmond aan Zee and the directional waverider buoy (Instrument 011)

The horizontal and vertical tide were obtained from the Kuststrook model. This is a model of the Dutch coast that is nested into a global ocean model. Output was available every 10 min for a station in Egmond North and South that are set 1300 m apart. Hourly averaged wind data was obtained from a meteorological station located at Ijmuiden Harbour.

A high resolution bathymetry survey was conducted during the field experiment over a length of 2000 m. In the vicinity of the two rip channels, the survey had a longshore resolution of 10 m. For the of sub-tidal and inter-tidal area a PWC [*MacMahan*, 2001] was used. The inter-tidal and super-tidal beach parts were surveyed with wheel-barrel mounted RTK-GPS instruments.

Sediment samples were collected in the feeder channels, the rip channel, on the bar and offshore of the bar (Figure 4.8). On August 23 and 24 samples were taken in and around Rip 1 during low tide and on August 26 in and around Rip 2 during upcoming tide. Samples of approximately 500 g were taken in the feeders, the rip neck, the bar and offshore of the bar to determine the spatial variation of the grain size. After the field campaign the sediment samples were dried and sieved following the Dutch standard NEN5104.

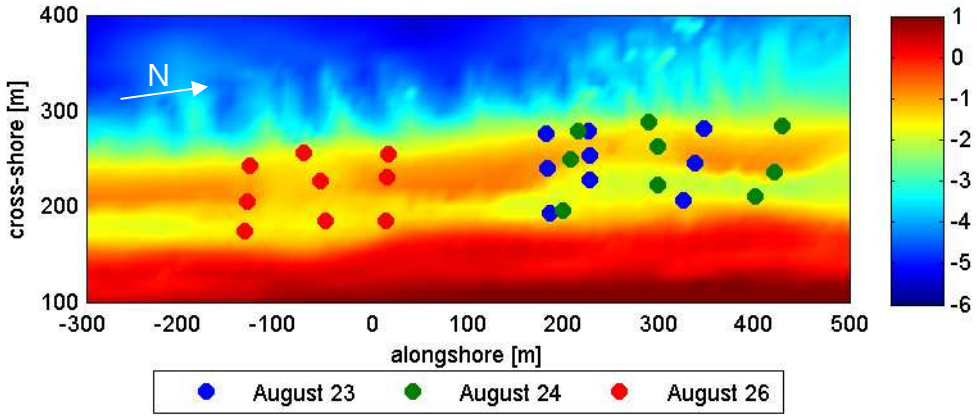

Figure 4.8 Locations where the sediment samples were taken.

4.3.2 GPS drifter data post-processing

The drifter instruments were tracked with GPS data loggers that had a sampling frequency of 0.5 Hz. The raw GPS data was post-processed with data from a static base station (dGPS) to sub-meter accuracy following *MacMahan et al.* [2009]. However, after post-processing the drifter positions still contained scatter associated with the inaccuracy of the GPS signal and from heave and tilt motions of the drifters. Therefore, reasonable drifter velocities could not be calculated directly from the raw data.

A moving average method was applied to the drifter positions that used a robust locally weighted regression [*Cleveland*, 1979] to smooth the drifter trajectory and remove scatter. A first order polynomial was then fit locally to each point (x_i, y_i). In this method, with increasing distance to the initial coordinate x_i the weight of the neighbouring point decreases (referred to as locally weighted regression) and points y_i that deviate strongly from their fitted value $\hat{y}_i$ are allocated less weight. This reduces the impact of outliers on the final result. The whole procedure is referred to as a robust locally weighted regression.

The method was developed for functions, i.e. every argument is assigned exactly one value and does not hold for the x- and y-coordinates of the drifter trajectories where one x-coordinate might be associated with several y-coordinates, e.g. when drifters circulate. To overcome this problem, both coordinates together are treated as a complex number in the time domain and the smoothing algorithm is applied to the complex number:

$$z_i(t) = x_i(t) + iy_i(t) \tag{4.1}$$

A time window for the local polynomial fit was subsequently defined and two aspects needed to be balanced: (1) The window must be sufficiently large to level out no-physical fluctuations. And (2)the window must not be as large as to average out true variations in drifter velocity or to cut off curves in the drifter trajectory. In the field, the drifters were observed to float at low velocities and were released for periods of 15 to 20 minutes. Given these prerequisites a smoothing window of 1 minute was determined to be acceptable.

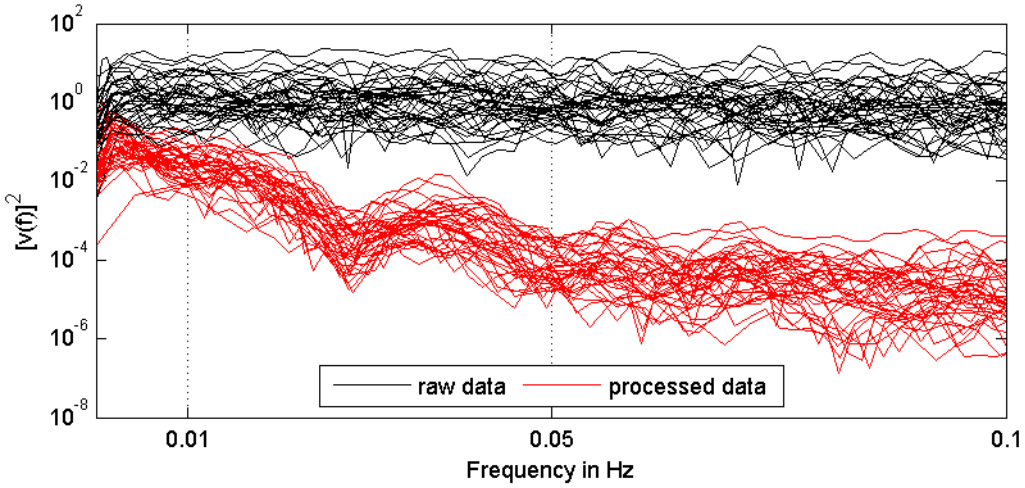

Figure 4.9 Squared velocity spectra of all drifter velocities calculated from the raw data points (black) and the smoothed data points (red). The spectra are produced using two to three Hanning windows (depending on the length of the deployment) with 50% overlap.

MacMahan et al. [2009] analysed the accuracy of data recorded with DeLorme Blueloggers in combination with data from a static base station (as used in the present field work). The calculated signal-to-noise-ratio (SNR) for this set-up was defined as

$$SNR(f) = \frac{S_{xx}(f) - S_{rr}(f)}{S_{rr}(f)} \tag{4.2}$$

where the error spectrum $S_{rr}(f)$ is produced from a stationary GPS logger and $S_{xx}(f)$ is the spectrum obtained from field data that was collected during a rip current experiment (RCEX) in Sand City, Monterey, California in 2007 [*MacMahan et al.*, 2010]. It was concluded that the SNR must be larger than 10 for reliable estimates of the true positions and velocities. In their study, *MacMahan et al.* [2009] found that the SNR was sufficiently large for frequencies below 0.01 Hz. Therefore, motions with frequencies above 0.01 Hz are not necessarily consistent with true drifter movements but can be as well associated with noise in the signal from GPS inaccuracies and heave and tilt motions of the drifters. Figure 4.9 shows the squared velocity spectra calculated from the raw data (black) and from the filtered data (red). The velocities generated with the robust locally weighted regression method reduced the amount of noise significantly so that most energy is contained in the frequency range below 0.01 Hz which is associated with true drifter motions. However, in the frequency band of interest (below 0.01 Hz) the energy is also reduced. This is attributed to the fact that noise is present in all frequency bands and thus, also in the frequency band below 0.01 Hz. As the drifter velocities measured during the field experiment (see Chapter 5) were small the energy associated with noise is relatively large compared to the energy associated with true drifter motions. And therefore, the energy in the frequency band of interest is reduced notably when the noise is filtered out.

4.4 Results

4.4.1 Hydrodynamic conditions and wind

The tide, wave and wind conditions that were present during the field campaign are presented in Figure 4.10. The wave conditions were moderate throughout the experiment with the offshore wave height H_{m0} ranging from 0.35 to 0.7 m and the wave period T_{m02} ranging from 2.4 to 3.8 s. The wave angles varied between 9° and more than 90° (with respect to the shore normal). The experiments coincided with neap tide with the smallest astronomical tidal range of 1.15 m on August 24. The wind speed ranged between 1 and 6 m/s during the experiments and came from various directions.

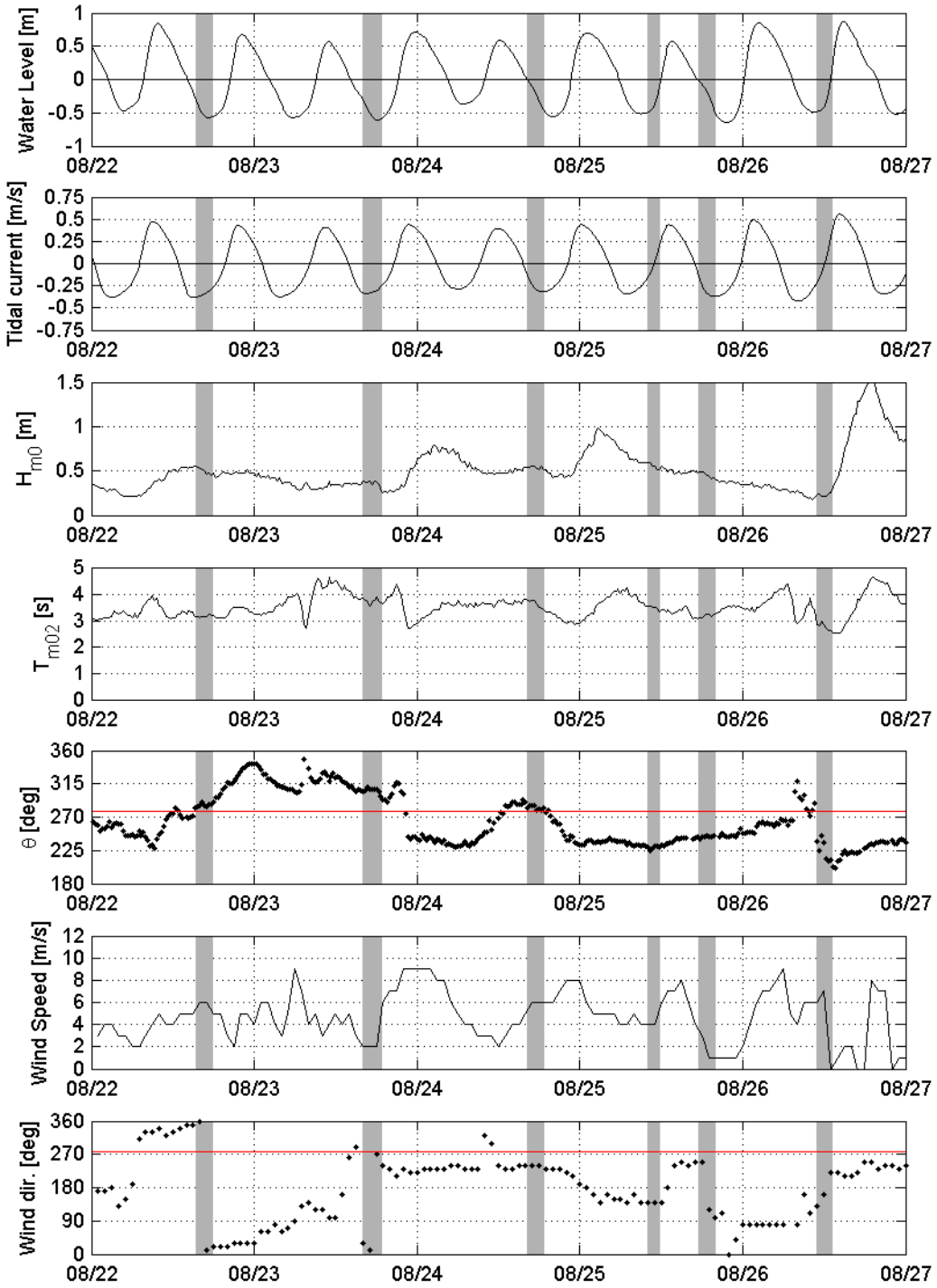

Figure 4.10 Conditions during the field campaign from top to bottom: water level, tidal current from the Kuststrook model at 10 m water depth, wave height H_{m0} , wave period T_{m02}, wave angle θ_h (black and shore normal in red), wind speed and wind direction (black and shore normal in red). The periods of the drifter experiments are indicated in grey.

4.4.2 Morphology

The results of the bathymetry survey have been converted into a local coordinate system that has an origin at the surf lifesaver station and was rotated by 82° so that the shore normal is orientated upwards. The surf lifesaver station of Egmond aan Zee was located at x = 103 050 m RD (Rijksdriehoek) and y = 514 910 m RD. The beach was fronted by three bars [see also *Short*, 1992; *van Duin et al.*, 2004]. The first one, the so-called swash bar, was situated in the intertidal zone and fell dry during low water. It was interrupted by several mini rip channels. The most outer bar was located 320 m offshore from the swash bar and was nearly longshore uniform (Longshore Bar Trough morphology). The bar of interest was the first sub-tidal bar, 70 m offshore from the swash bar. Under accreting conditions that prevailed in the week before and during the field experiment, the morphology shifted towards a Rhythmic Beach and Bar morphology [*Wright et al.*, 1984] (Section 2.3).

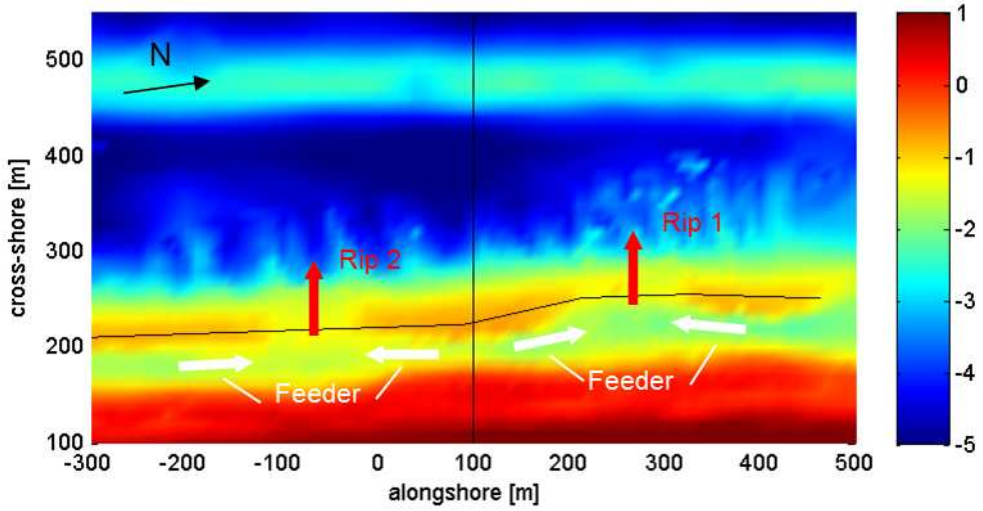

Figure 4.11 Results of the bathymetry survey using PWC and wheel-barrow mounted RTK-GPS instruments. Along the black lines transects are extracted (see below). The feeder channels are indicated by white arrows and the rip channels by red arrows.

The experiments were conducted in two distinct rip channels at x = 280 m (Rip 1) and x = -80 m (Rip 2) that were 400 m apart (Figure 4.11). The feeder channel widened onshore of the rip channels whereas it narrowed onshore of the bar. Between the two rip channels the bar tended to weld towards the beach. The bar North of Rip 1 was only about 150 m long.

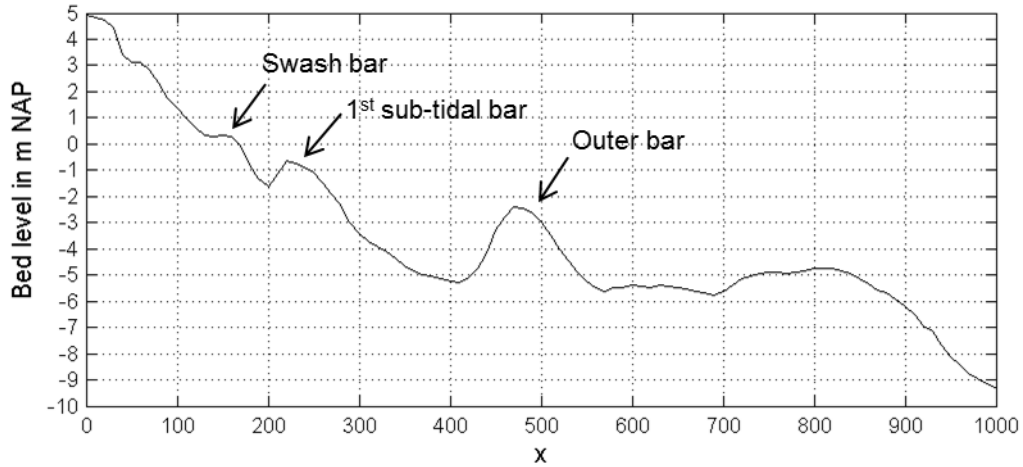

Figure 4.12 Cross-shore transect at x=100 m which represents a typical beach profile at the field site.

The channel width was O(100m). The height of the bar crest between the rip channels was at z = -0.81 m on average. The bar to the South and in particular the one to the North are somewhat lower (z = -0.86 and z = -0.95 respectively). The minimum depth in Rip 1 was z = -1.39 m and in Rip 2 z = -1.35 m. Thus, the channel depth with respect to the bar crest height to the North or to the South was between 40 and 60 cm. This was less than observations in previous years by the lifeguards and a description by Reintjes [2002] about rip channel depths in the order of 1 m.

There are two possible explanations why the channels were less pronounced in summer 2011: Firstly, a beach nourishment was realised in spring 2011 along with a shore-face nourishment that extended over the whole summer. Secondly, the Dutch coast was hit by several storms in early summer that reset the beach profile at Egmond aan Zee efficiently.

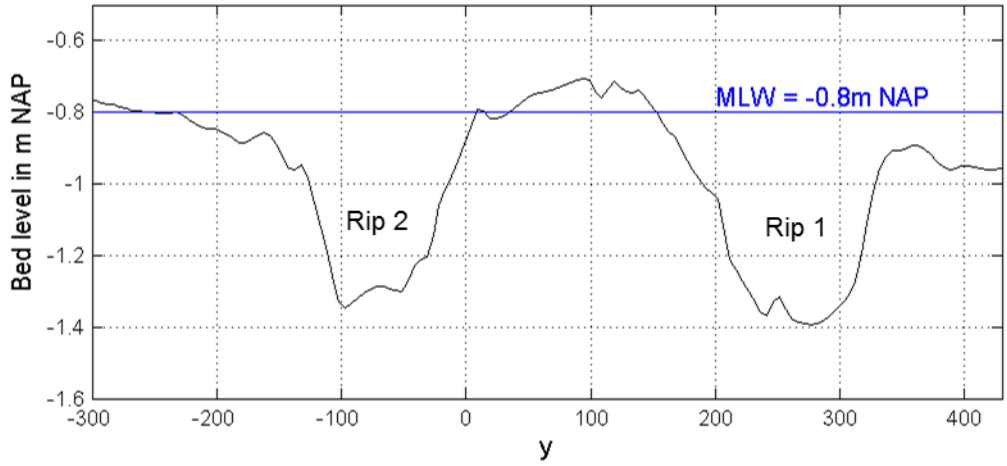

Figure 4.13 Longshore transect through the Northern (Rip 1) and Southern (Rip 2) rip channel

4.4.3 Sediment

D_{50} values were determined from sieve curves of the sediment samples collected during the field experiment (Figure 4.14).

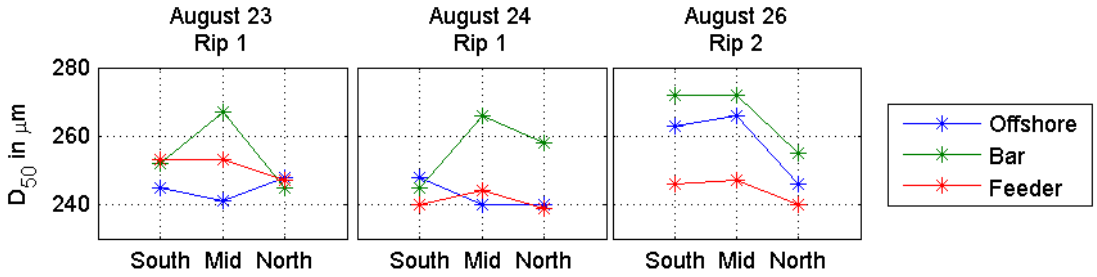

Figure 4.14 The D_{50} values calculated from the sieve curves.

The sediment in the rip channel (Figure 4.14, labelled as 'Bar Mid') was coarser than on the adjacent bars because the higher flow velocities in the channel erode the finer material first. The sediment onshore of the bar in the feeder channels was generally finer than on the bar. The erosion of finer material on the bar was attributed to the stirring of sediment by breaking waves and to the limited flow depth over the bar that leads to higher near bed velocities.

One needs to keep in mind that sediment grain size can vary strongly both in space and in time, as pointed out by *Gallagher et al.* [2011] at Truc Vert (France). These fluctuations could not be captured during this experiment and the results represent only point samples in space and time. But the results of the sediment analysis at Egmond are consistent with observations at Truc Vert (France) where the sediment was also coarser in the rip channel than on the bar.

5 Rip current field data

5.1 Introduction

The Lagrangian measurements obtained during the field experiment were evaluated qualitatively and quantitatively. In total six measurement sessions with four to five deployments each were conducted. The deployments are labelled by the measurement session (indicated by the date, August 25 A and B refer to the morning and evening session respectively) and the deployment number in the session. An overview of all deployments and the observed drifter trajectories is provided in Appendix B.

Initially, a comparison of the drifter instrument and human drifter results was undertaken. The purpose of this comparison was to demonstrate that the results obtained from the drifter instruments suitably represent humans and hence can be considered in the context of swimmer safety. This is followed by a description of the observed flow patterns, their features and their variability. Finally, the measured rip events are quantified and correlated to outside forcing. In this chapter, reference is made to specific deployments which are summarised in Appendix B.

5.2 Lagrangian flow

5.2.1 Suitability of drifter instruments

The suitability of the drifter instruments to represent humans caught in a rip current were investigated by conducting a comparison between the instrument results and humans acting as drifters (monitored via GPS units). The human drifters were observed to follow a similar trajectory as the drifter instruments (Figure 5.1) and to float at a similar cross-shore velocity velocity (Figure 5.2) throughout the rip channel. This comparison demonstrated that the measurements obtained from the drifter instruments were comparable to those that could be expected of a human caught in the same rip current. This comparison enables the results of this study to also be evaluated in the context of swimmer safety.

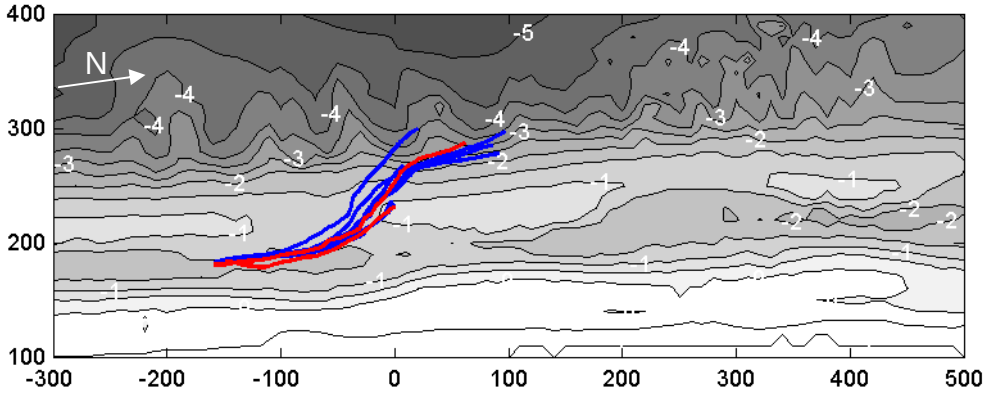

Figure 5.1 Trajectories of drifter instruments (blue) and human drifters (red) on August 26 (dpl.3)

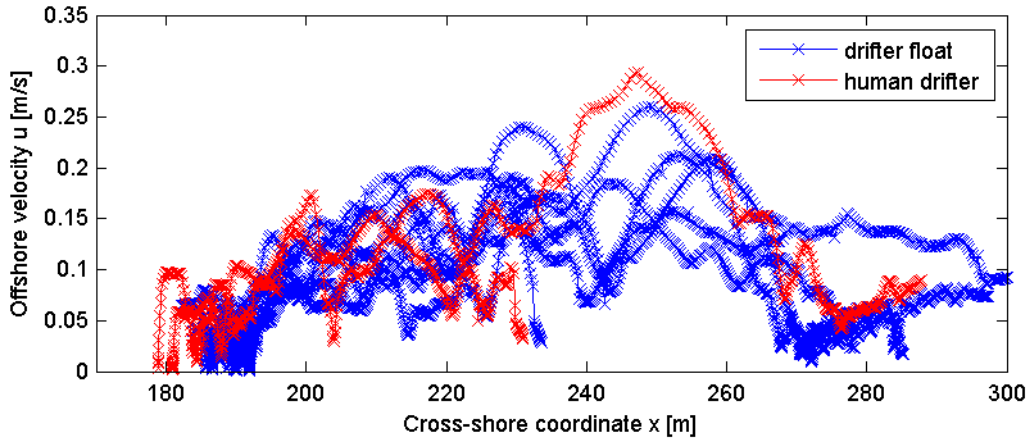

Figure 5.2 Off-shore velocities of drifter instruments (blue) and human drifters (red) in the rip channel on August 26 (dpl.3)

5.2.2 Observed flow patterns

In the experiment three flow patterns were observed: (1) a locally governed circulation cell (2) a pattern in which the drifter initially floats offshore and is then advected by a strong longshore current and (3) a meandering longshore current.

Type 1: Circulation

A local circulation cell was observed on August 22 (dpl.2 and 4), August 23 (dpl.1), August 24 (dpl.1, 2 and slightly in dpl.4 and 5) and August 25 B (dpl.2 and 3) (see Appendix B). The circulation cells were confined to the surf zone and were centred over the end of the Southern bar (see Figure 5.3). Only one counter clockwise circulation was observed downdrift of the channel while at no time during the experiment was a counter rotating eddy updrift of the rip channel observed. Flow pattern type 1 is associated with drifter retention in the surf zone and dominated in 9 out of 28 deployments.

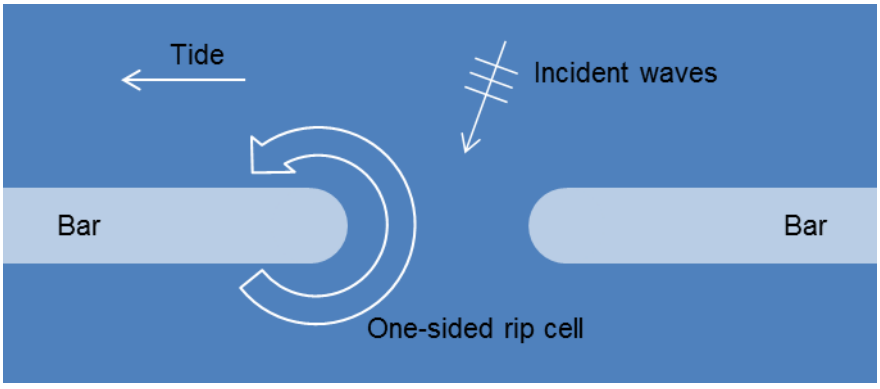

Figure 5.3 Type 1: One-sided circulation cell downdrift of the rip channel.

In most deployments the water depth over the bar was shallow and the drifters became stranded on the bar when they returned shoreward. Whilst this demonstrated a return flux, the existence of a complete circulation cell could be definitively measured only during some deployments. For example on one occasion (August 22, dpl.4), the water level was -0.56 m and a number of drifters were observed to loop within a circulation cell up to three times

(Figure 5.4). The circulation cell was confined to a small area at the tip of the sand bar where the crest is lower than the average bar height.

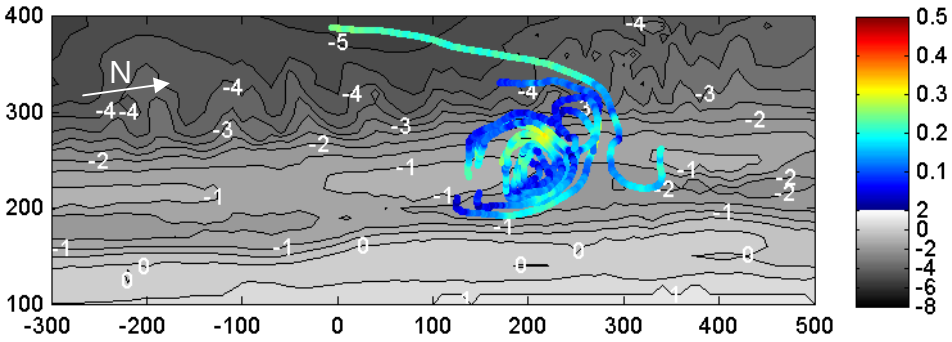

Figure 5.4 Local circulation cell on August 22 (dpl. 4): The velocities are indicated by the colours and the bathymetry is plotted underneath in grey. The tidal water level is -0.56 m.

Type 2: Advection alongshore

On August 22 (dpl.1 and 3), August 23 (dpl.2 to 5), August 24 (dpl.3), August 25 A (dpl.1 to 3), August 26 (dpl.3 and 4) (see Appendix B) the drifters floated through the channel, exited the surf zone and were advected by a longshore current offshore (Figure 5.5). Flow pattern type 2 is associated with drifter ejection from the surf zone and dominated in 12 out of 28 deployments. Surf zone exits were thus the prevailing flow pattern. Note that not all deployments could be attributed unambiguously to exactly one flow type because drifters did not always behave consistently.

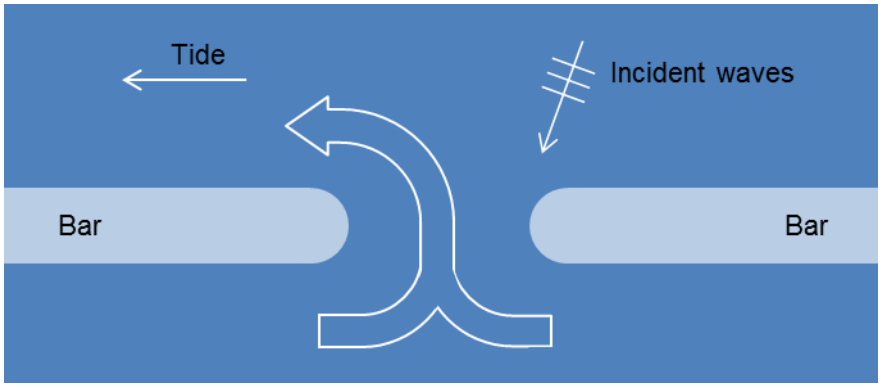

Figure 5.5 Type 2: Alongshore advection

The flow direction offshore of the bar was consistent with the tidal flow during those deployments. For the cases where the tidal currents were weak offshore of the bar, the drift direction was governed by the angle of wave incidence and/or the prevailing wind direction. When the drifters appeared to have reached a stationary state, the deployments were ended. Often any drifter that demonstrated the tendency to turn towards shore had done so by this time. It is possible that the drifters may have ultimately turned shoreward however the drifters did not show a tendency to change their shore parallel floating direction within a practical timeframe (approximately 20-30 minutes). Flow pattern 2 was observed with rather high flow velocities in the rip channel (on average $u_{drifter} = 0.31$ m/s compared to $u_{drifter} = 0.18$ m/s observed with flow pattern 1) and suggests that stronger currents possess enough inertia to enable the current (and the drifter) to exit the surf zone (Figure 5.6).

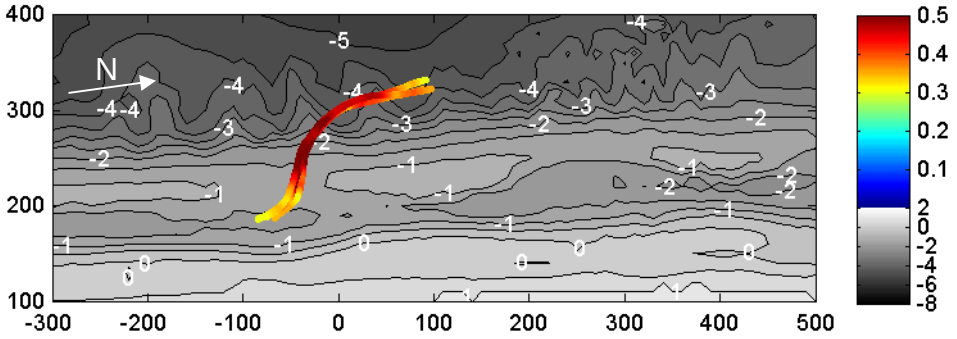

Figure 5.6 Offshore directed drifter paths on August 25 A (dpl.3): The velocities are indicated by the colours and the bathymetry is plotted underneath in grey. The tidal water level is -0.48 m.

Type 3: Meandering longshore current

A meandering longshore current directed northward occurred on August 25 A (dpl.5) and August 26 (dpl.5). This flow pattern is separated from (2) in the way that drifter paths are confined to the zone between the breaker bar and the beach (Figure 5.7). A meandering longshore current was observed only in 4 deployments. This was attributed to the fact the deployments were conducted with water levels around and below NAP +0 m, which favour longshore currents instead of rip currents.

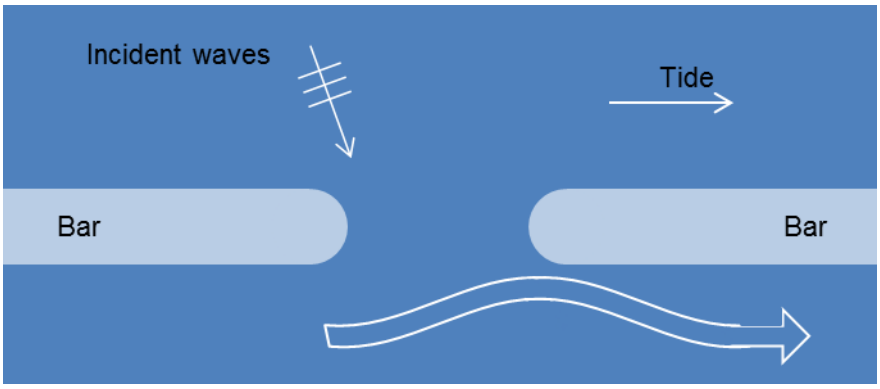

Figure 5.7 Type 3: Meandering alongshore current.

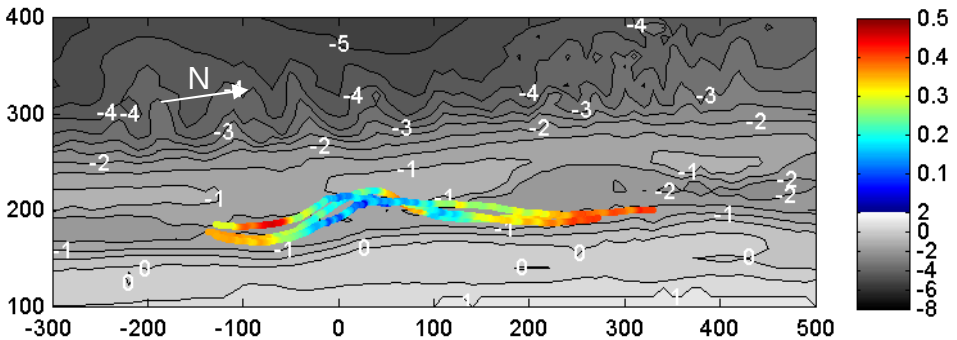

Figure 5.8 Meandering longshore current on August 25 A (dpl.5): The velocities are indicated by the colours and the bathymetry is plotted underneath in grey. The tidal water level is -0.14 m.

The longshore velocities are strongest onshore of the rip channel and from there the drifters float towards the tip of the down drift bar and slow down (Figure 5.8). They then drift back towards the centre line of the feeder channel and continue to travel parallel to the bar. This pattern was observed during morning measurements when the tide was rising and in the presence of a northward directed tidal current along the Dutch coast. Both wind and waves came from Southern directions and were likely to enhance the northward drifter movement.

5.2.3 Rip current features

Apart from the rip current flow patterns, four other rip current features were investigated during the field experiment: the maximum observed rip velocities, location of the maximum offshore velocities, the offshore extension of the rip and the flow behaviour onshore of the rip neck. Each of these features are addressed below.

The maximum drifter velocity measured was 0.60 m/s during deployment 1 on the morning of August 25 (Figure 5.9). This deployment occurred when the highest offshore wave heights were recorded at the site. The wave height H_{m0} was as large as 0.7 m and the offshore wave period was T_{m02} of 3.6 s. A wave angle of incidence of 224°N was measured and the northern feeder was absent. The drifters (generally) reached their maximum velocity just offshore of the bar crest which was also the shallowest point of the rip channel. The rip channel was characterised as a depression in the bar and thus exhibits a berm type appearance in the cross-shore profile (Figure 5.10).

Figure 5.9 Drifters floating offshore in a strong rip current (up to 0.6 m/s) on August 25. Picture by: www.muien.nl (2011, Willem Verbeek)

It was clearly visible from the beach that the drifter velocities were larger on August 25 than during previous deployments. Helpers reported that they had difficulties holding on to the drifters before their release and from the PWC, the sediment laden rip head was visible. No drifters returned over the bar. An onshore mass flux over the bar was observed by a human drifter that was not tracked by GPS at that time. The rip vanished quickly with upcoming tide and within 40 min a longshore meandering current prevailed.

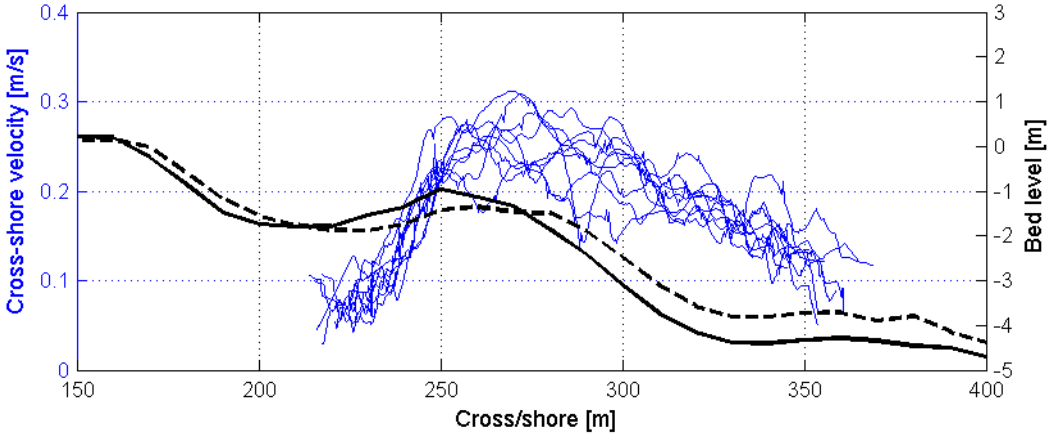

Figure 5.10 Cross-shore drifter velocities in the rip channel of Rip 1 on August 23 during dpl. 4 (positive offshore directed). The solid black line represents the bed profile through the bar at x = 220 m and the dashed black line represents the bed profile through the rip channel at x = 280 m.

The offshore extent of the measured rip currents was in the order of 100 m offshore of the bar crest and stretched as far as 150 m on August 23 (dpl.5) and August 25 A (dpl.1). Large offshore extents were associated with flow pattern (2) in which the drifters exited the surf zone accompanied by larger flow velocities. For this flow pattern, the maximum velocities were found in the rip neck, just offshore of the bar (Figure 5.10). In contrast, on August 22 (dpl.4), August 23 (dpl.1) and August 25 B (dpl.2 and 3) when the drifters were caught in a local circulation cell (flow pattern 1), the offshore extent was only 30 to 60 m offshore of the bar crest.

An area of stagnant or slight onshore flow was identified onshore of the rip neck on August 22 (dpl.1), August 23 (dpl.2) and August 24 (dpl.3 to 5) (see for example Figure 5.11). This phenomenon became most obvious when on August 24 (dpl.3) three human drifters commenced passive floating in the feeder channel. One was located onshore of the rip neck, and one each to the North and to the South. The human drifter onshore of the rip neck was washed ashore while the other two became trapped in the rip.

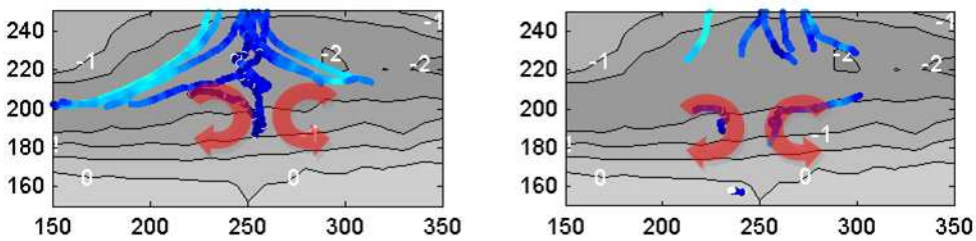

Figure 5.11 Onshore of the rip channel drifters are trapped in an area with stagnant or slightly onshore directed flow during the deployments on August 23, dpl.3 (left) and August 24, dpl.4 (right). The schematised flow pattern of the second circulation is indicated by the red arrows. The velocities are plotted in colours and the bathymetry is plotted underneath in grey. A portion of the drifters is trapped in an area of stagnant or slight onshore flow.

5.2.4 Temporal variations

No fixed instruments were installed during the field experiment that would have allowed monitoring the temporal flow variations at a fixed point. However, on August 23 (dpl.5) all drifters were released at the same location in intervals of 1 minute. This release pattern

presented a limited view of the rip current's dynamic behaviour (Figure 5.12). From 18:07 to 18:13 all drifters travelled offshore where they then turned southward (Pattern 2). From 18:14 to 18:18 the drifters were washed on the bar adjacent to the channel in the North (Pattern 1).

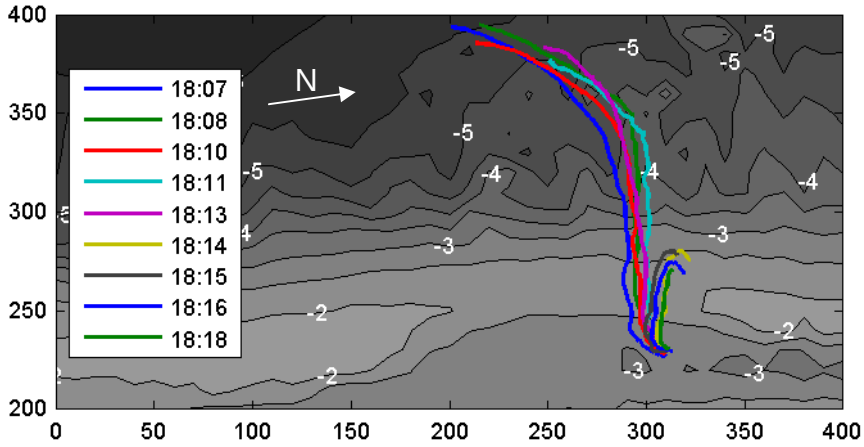

Figure 5.12 Drifter trajectories on August 23 (dpl.5). Each minute one drifter was released in the same location in the rip neck.

This observation suggests that the flow pattern in the rip channel was stationary over a period of at least 6 minutes. This assumption is also supported by flow patterns observed during the other deployments. The drifters tended to cluster together and followed similar trajectories as on August 23, dpl.3 (Figure 5.13) and stayed close together even offshore of the channel. Typically the drifters accumulated at the edge of a sediment plume which was believed to define the outline of the rip head.

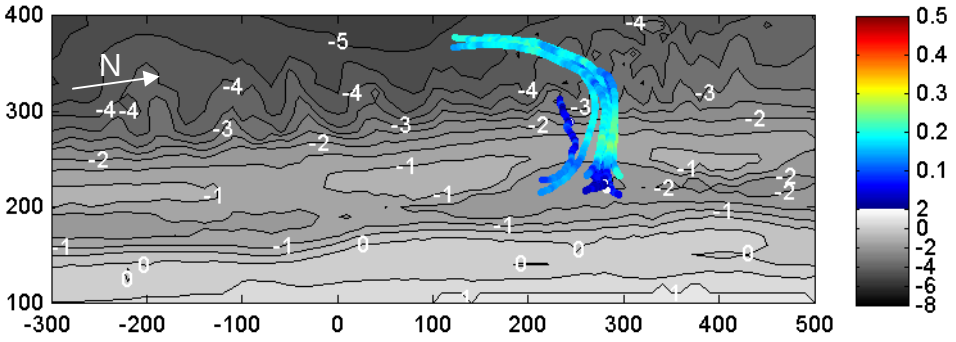

Figure 5.13 Drifter path on August 23 (dpl.3): The velocities are indicated by the colours and the bathymetry is plotted underneath in grey. The drifters do not disperse but accumulate at the edge of the rip head. The tidal water level is -0.37 m.

5.3 Statistical analysis of the rip strength

5.3.1 Introduction

Rip current flow is influenced by a large number of geometrical and hydrodynamic parameters. The field campaign was performed over a period of five days and the geometric conditions are believed not to have changed significantly. The nearly constant geometry

allowed this study to focus on the effect of the hydrodynamic parameters. Initially, the wave dissipation on the bar, which appears to be the main driving force of rip currents, was investigated. Several studies suggest that the rip current is enhanced during low tide [*Aagaard et al.*, 1997; *Austin et al.*, 2010; *Brander*, 1999] because wave dissipation increases with lower water levels over the bar. The ratio of the offshore wave height H_{m0} over the water depth on the bar d indicates the intensity of wave breaking and the amount of wave dissipation. Subsequently, the statistical dependency of the rip strength on the wave period and the wave angle were tested.

5.3.2 Definition of rip current properties

Rip currents exhibit a complex spatial flow pattern and in this study, a measurement was considered a rip event if the offshore flow dominated over the longshore flow. However, in order to correlate the behaviour of a rip current to the hydrodynamic forcing observed, the rip events were quantified. The observations were expressed in one value, the rip strength (see also Section 3.4). The rip strength is defined as the maximum offshore directed velocity component in a rip event. The offshore velocity component was chosen for two reasons: Firstly, the direction as a second variable is disregarded and therefore averaging over all drifters in one deployment is possible. Secondly, the rip strength is an indicator for the strength of the rip circulation cell and does not account for a superimposed longshore current.

The maximum offshore directed velocity component was extracted for every drifter trajectory. For example, the exit of a drifter through the rip channel is one drifter observation. If the drifter loops several times in a rip current cell it is possible that this drifter yields several observations. To account for uncertainties associated with an individual drifter observation, the velocity maxima for each drifter within the deployment were averaged to determine the rip strength. Therefore, each deployment is described by a single rip strength value. Due to the nature of the experiment a complete description of the rip current is not available and therefore the maximum offshore velocity in the rip is deduced from the set of drifters that were used in each deployment.

The boxplot of the rip strengths (Figure 5.14) provides an overview of the observed rip events each day. In general the rip strength was between 0.2 and 0.3 m/s with somewhat lower values on August 25 B (evening session) and August 26. The measurements obtained on August 25 A (morning session) clearly stand out of the dataset as the strongest observed rips, but also the greatest variability in velocity. This variability is associated with varying drifter deployment patterns or with the small number of drifters that logged data during that deployment.

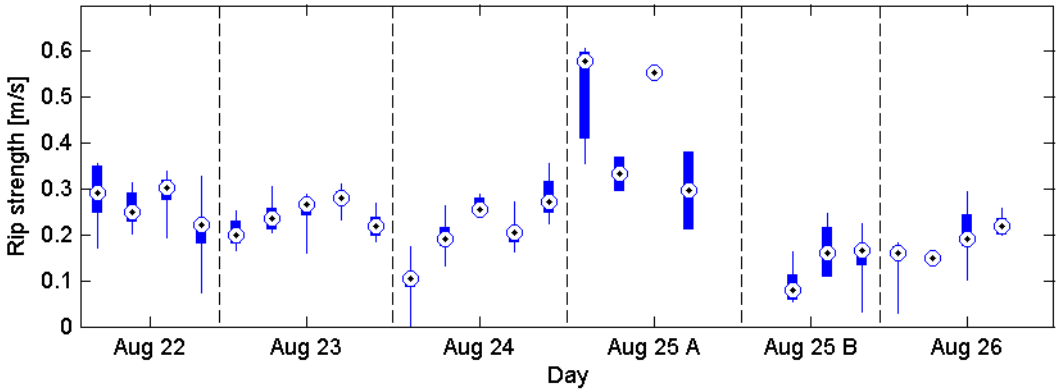

Figure 5.14 Plot of the rip strength for each deployment. The median of the rip strength in m/s is indicated by the black circle, the 50% confidence interval is indicated by the blue box and the blue whiskers mark the 95% confidence interval.

5.3.3 Data analysis

The ratio of wave height over water depth on the bar H_{m0} / d provides an indicator for the intensity of wave breaking and energy dissipation on the bar. The value increases with increasing wave height and decreasing water level respectively. Several definitions for the wave heights are available for this ratio. The breaking wave height incorporates the effects of offshore wave height, period and angle of incidence. Waves with a long period shoal more and thus result in larger breaking wave heights. In contrast, waves with a large angle of incidence refract towards the shoreline and are smaller at the break point.

In this study the offshore wave height H_{m0} was used because it could be obtained immediately from instrument 011 (see Figure 4.7) and thus was more transparent. The water depth over the bar differed for the deployments because the experiments were conducted in different rip channels and the wave direction varied between northern and southern directions. For each deployment the bar crest height updrift of the channel was determined. The mean bar height north of Rip 1 was calculated as -0.95 m, the bar between Rip 1 and 2 as -0.81 m and the bar south to Rip 2 as -0.86 m from the cross-section shown in Figure 4.13.

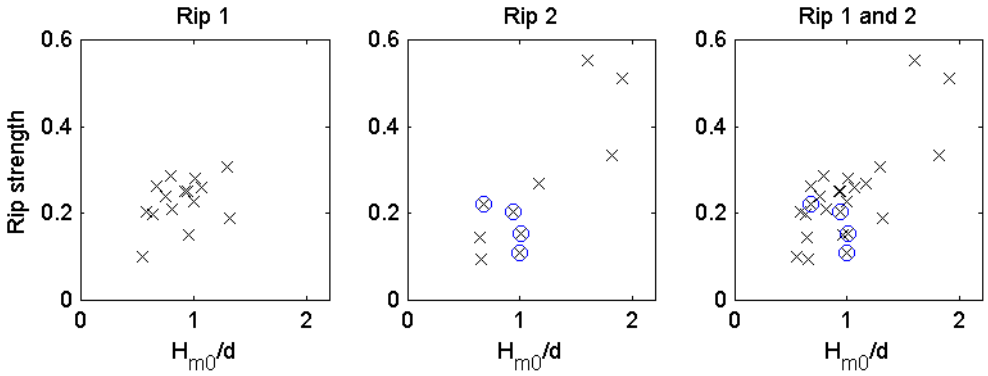

Figure 5.15 Rip strength over H_{m0}/d in Rip 1 (left) and 2 (right). Blue circles indicate measurements with offshore wave angles larger than 90°.

Some measurements were performed when the offshore wave buoy recorded wave angles larger than 90° (Figure 5.15, blue circles). Wave angles larger than 90° imply that waves

propagate offshore at the wave buoy i.e. that they are generated by a local offshore wind. For these samples, the near shore wave heights were not related to the offshore values and were discarded.

The measurements were performed in two distinct rip channels. So first, it needs to be shown that it is a reasonable assumption to treat the data from both rips as one batch. The data sets from both rips suggest an upward trend (see Figure 5.15). In Rip 1 the rip strength does not exceed 0.3 m/s whereas in Rip 2 two strong rip events of approximately 0.55 m/s were measured. It cannot be determined with the available data whether the large velocities measured in Rip 1 are data outliers or indeed show a trend. Furthermore, as the measurements were not performed simultaneously in both channels, those differences cannot be clearly attributed to either the changed hydrodynamic conditions or the geometrical differences of the two rip systems. Rip 1 is somewhat wider than Rip 2 and the bar adjacent to the North of Rip 1 is somewhat lower and shorter than the one adjacent to the South of Rip 2 (see also Section 4.4.2). However, due to the limited size of the data set all measurements are treated as one batch in the following procedure.

Initially, a linear least squares regression was fit to the data. The linear prediction of the data set was given by:

$$f(x) = mx + n \tag{5.1}$$

Where x and $f(x)$ correspond to the ratio H_{m0} / d and the predicted rip strength, respectively. The slope m and the intercept n were chosen such that the sum of the squared residuals became minimal:

$$\sum_{i=1}^{n} (y_i - f(x_i))^2 \tag{5.2}$$

With y_i being the measured rip strength and $f(x_i)$ the predicted value. The regression line was forced through the origin (0,0) because no rip currents are generated with zero wave height.

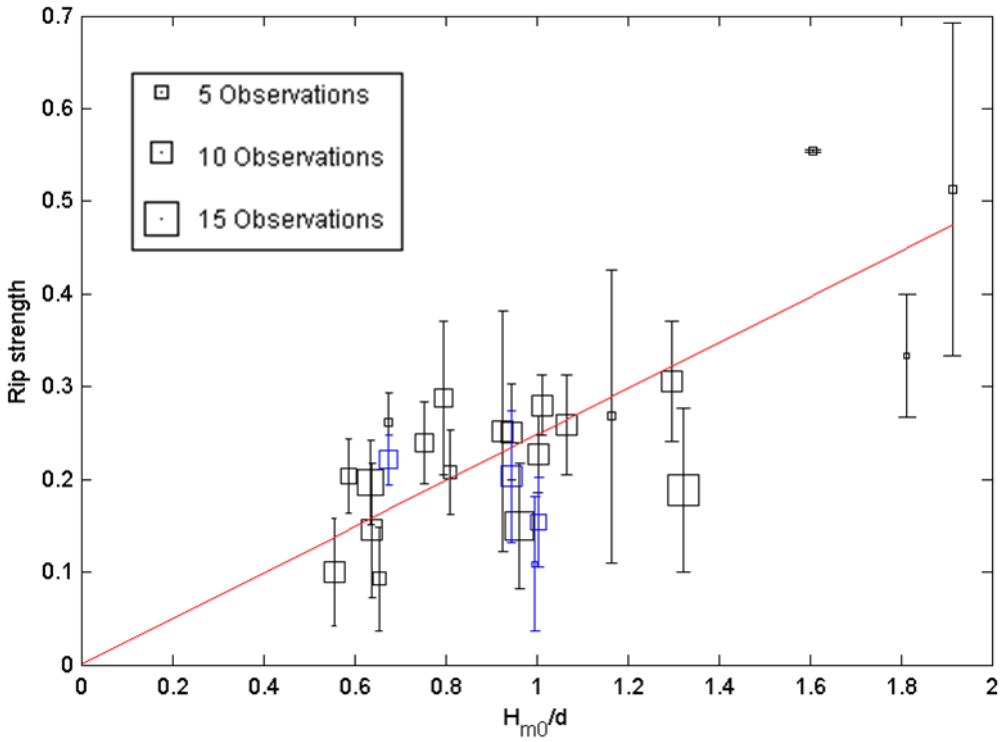

Figure 5.16 Rip strength versus H_{m0}/d. Blue data points indicate outliers with a wave angle above 90° with the shore normal. These points are excluded from the regression model. The error bars specify the 90% confidence interval of each data point. The solid red line is the linear least squares regression.

The coefficient of determination R^2 was used as an indicator for the 'goodness of fit' for the regression model:

$$R^2 = 1 - \frac{\sum_{i=1}^{n}(y_i - f(x_i))^2}{\sum_{i=1}^{n}(y_i - \bar{y})^2} \tag{5.3}$$

For the linear regression model of rip strength versus H_{m0}/d the R^2 value was 0.68 and the p-value was 0.0048. The p-value provides the probability to reject the null hypothesis though it is true. The null hypothesis states that the data is normally distributed around a zero mean. For a confidence interval of 95%, the p value should therefore be smaller than 5%. In that case the correlation between the independent variable and the response variable is statistically significant.

The R^2 and p-value alone do not suffice to assess the goodness of a fit. Furthermore, the residuals between the predicted values and the response values must be random observations from a normal distribution centred on zero with a constant standard deviation.

$$res_i = y_i - f(x_i) \tag{5.4}$$

In the graphical analysis it is observed that the residuals are not normally distributed (Figure 5.17, right). The negative trend of the residuals vs. H_{m0} / d (Figure 5.17, middle) may be interpreted in two ways: (1) The slope of the linear trend line is overestimated due to the large rip velocities measured on August 25 A or (2) the relation between rip strength and H_{m0} / d is not linear but the trend in reality flattens with large values of H_{m0} / d .

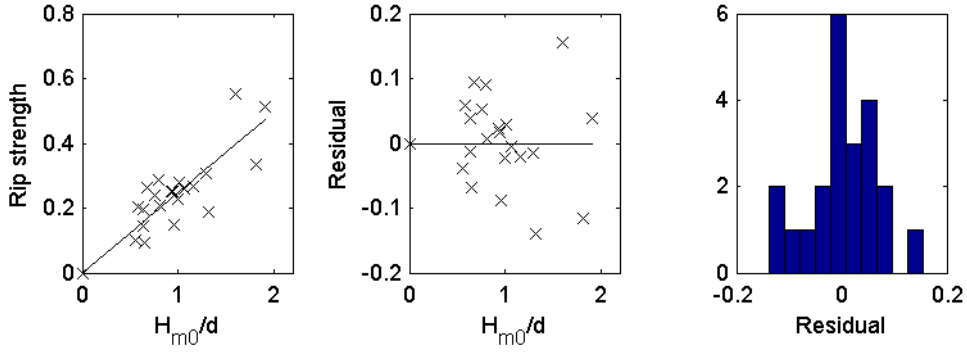

Figure 5.17 Graphical analysis of the least squares linear regression for rip strength versus H_{m0}/d. From left to right: scatter plot with least squares linear regression, scatter plot of the residuals between predicted and measured values versus the ratio of wave height over water depth and histogram of the residuals.

Other wave parameters were tested such as the offshore wave period and the wave angle. The wave period is not independent from the wave height and was therefore investigated in terms of the offshore wave steepness:

$$s_0 = \frac{H_{m0}}{L_0} \tag{5.5}$$

L_0 is the offshore wave length which is estimated from the wave period through the dispersion relationship:

$$\omega^2 = gk \tanh(kd)$$
$$\text{or } L = \frac{gT^2}{2\pi} \tanh\left(\frac{2\pi d}{L}\right) \tag{5.6}$$

No statistically significant relationship was determined between the wave steepness and the rip strength (Figure 5.18, left) despite the hypothesis of a weak dependency (Section 3.4). During the field campaign only a small range of wave periods was recorded with T_{m02} ranging between 2.4 and 3.8 s. This was not sufficient to show any trends related to the wave period.

The offshore velocity was hypothesised to decrease with increasing wave angle but such a trend was not observed in the field (Figure 5.18, right). In contrast, the strongest rip was observed with 50° angle of wave incidence offshore. It is likely that a physical process that was not considered in the study had enhanced the strong rip measured on August 25 A. On that day, a light cross-offshore wind was blowing from 140°N and thus, the wind direction was in favour of the rip current.

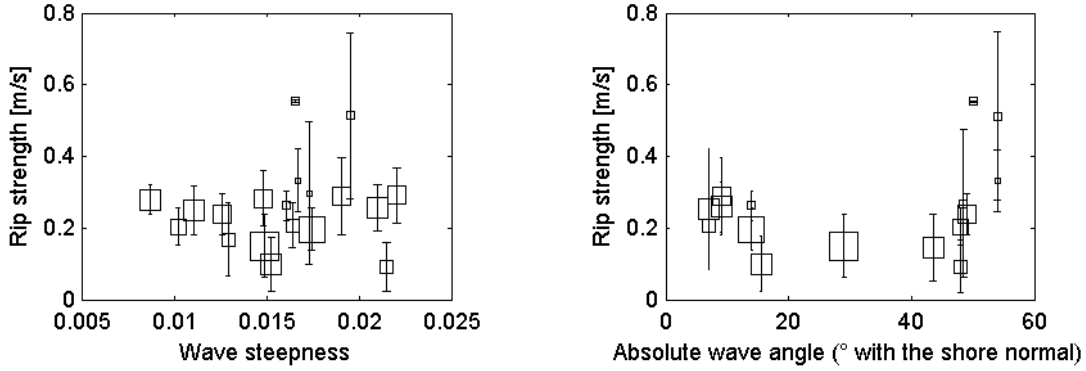

Figure 5.18 On the left: Rip strength vs. wave steepness. And on the right: Rip strength vs. absolute wave angle with the shore normal.

5.4 Discussion

Drifter exit rate

12 out of 28 deployments were dominated by flow pattern 2 (drifter ejection from the surf zone, Section 5.2.2) and exit rates were as high as 100% during some of the deployments. The average exit rate was around 55%. Those values are considerably higher than observed drifter exits during the Rip Current Experiment (RCEX) in Sand City, Monterey, California, which did not exceed 30% [*Reniers et al.*, 2009]. *Reniers et al.* [2009] propose the exit parameter

$$E = \frac{X_w}{H_{rms,0} T_{m01}} \tag{5.7}$$

where X_w is the surf zone width. This suggests that the exit rate increases with increasing surf zone width. However, this parameter is only applicable when the rip current is contained within the surf zone. During the experiments at Egmond, the waves were very small and the surf zone was narrow. Therefore, the rip neck was not confined to the surf zone. The drifters that floated offshore in the channel had already left the surf zone when they reached the end of the rip neck. Outside of the surf zone the onshore mass flux is much smaller due to the lack of wave breaking. Therefore, drifters did not return in most of the cases. At Sand City, the rip current was contained within the surf zone and resulted predominantly in circulation of drifters and their retention within the surf zone.

Temporal behaviour

It was observed that the drifters behaved consistently per deployment and followed the same trajectories. To investigate the temporal behaviour of the rip, drifters were released at a fixed location at intervals of 1 min during one deployment. The flow pattern was stationary for approximately six minutes, changed and remained constant for another four minutes. These temporal variations may be attributed to very low frequency (VLF) motions with a time scale from 250 s to 30 min that have been shown to be associated with oscillations or rip current cells [*MacMahan et al.*, 2004]. However, the temporal variations observed at Egmond aan Zee may also simply be a result of a slight change in the hydrodynamic forcing. The nature of this field experiment does not allow the observations about the temporal rip behaviour to be attributed to either VLF motions or a change in mean hydrodynamic forcing.

Drifter behaviour onshore of the rip neck

With flow pattern 1 and 2 an area of stagnant or slight onshore flow onshore within the rip neck was observed in this experiment and may be an indicator of the second circulation (Section 2.3) as described in *Haller et al.* [2002]. This process may explain the trend of the shore line, which retreats onshore of the rip neck and advances onshore of the bar (see Section 4.4.2). The higher waves onshore of the channel suspend sediment that is then advected longshore towards the area behind the bar where the breaking waves are smaller and thus induce a lower set-up. Behind the bar this sediment surplus contributes to the narrowing of the feeder channel.

With flow pattern 3 the drifters were observed to slow down onshore of the rip neck and to drift towards the tip of the down drift bar. In the channel no wave breaking occurs so the driving force of the longshore current is absent. As a consequence the drifters slowed down. It cannot be explained definitely why the drifters left the centre line and floated towards the tip of the down drift bar. The deployments were conducted with intermediate water levels around NAP +0 m so probably there was still a weak rip current circulation cell present in which the drifters were advected in offshore direction. But the longshore current overruled this rip circulation cell and the drifters remained between the bar and the beach. Furthermore, the meandering drifters followed the curved shoreline onshore of Rip 2 (Figure 5.8).

Rip strength

The rip strength increased with an increasing ratio of wave height over water depth H_{m0} / d. This implies stronger rip activity with low water levels and high waves.

Video images (Argus) indicate that with higher water levels, the waves are not dissipated on the surf zone bar, but on the swash bar (Figure 5.19, bottom panel). This interrupts the driving mechanism for rip currents on the first surf zone bar and explains the low rip activity at times of low values of H_{m0} / d.

However, the linear relation may not hold for very low water levels (large H_{m0} / d) when the waves are also dissipated in the channel. At very low water levels, wave breaking commences in the channel (Figure 5.19, top panel). As a consequence the longshore variation in wave dissipation and water level set up (which drive the rip current circulation) are weakened (Rip 2) or completely absent (Rip 1). The offshore current in Rip 2 is evident from the protuberance in the wave dissipation band. The opposing current causes the waves to refract towards the current and causes a non-uniform wave dissipation band.

It cannot be explained definitively why Rip 2 is stronger and longer active than Rip 1. A possible explanation is given by *Svendsen et al.* (2000). In their numerical study they have worked out that a rip has a region of influence from where it draws in water. A very long bar surrounding the rip does not enhance the current any further. Is is expected that the rip is weaker when the adjacent bar is shorter (as the bar north of Rip 1) and therefore the onshore mass flux over the bar is limited.

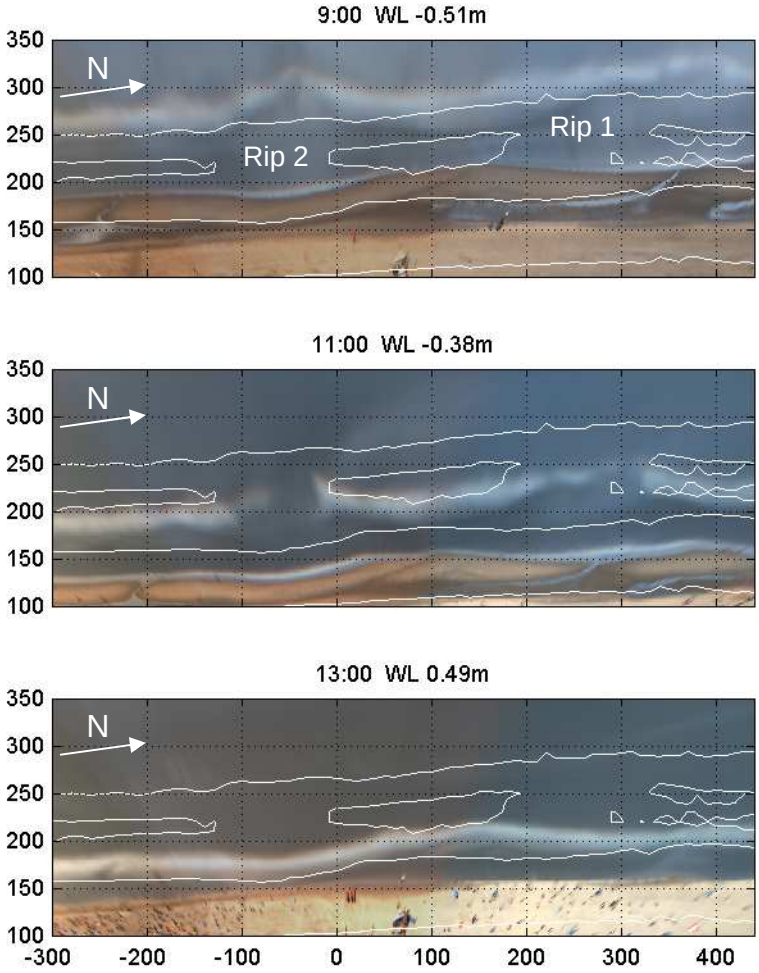

Figure 5.19 Series of Argus images on August 25. The water level increases from top to bottom and therewith the wave breaking shifts from offshore of the first surf zone bar to the swash bar. Wave breaking takes place slightly offshore of the white band that indicates the bores of the broken waves.

5.5 Conclusions

An extensive dataset of rip current measurements in a Lagrangian framework was collected. In total, 28 drifter deployments were performed and 21 of these observations were classified as rip events. The flow pattern and drift velocities of human drifters and drifter instruments were similar and allow using drifter instruments in the context of swimmer safety.

Three flow patterns could be observed:

1. A local one-sided circulation cell that was observed with rather weak rip current flow.
2. A strong offshore movement of the drifters that were then advected by a longshore current offshore of the bar (observed with rather strong rips).
3. A meandering longshore current that prevailed with high water levels.

Offshore directed drifter velocities were on average 0.18 m/s with flow pattern 1 and 0.31 m/s with flow pattern 2. The maximum offshore directed velocities of 0.60 m/s were measured on August 26 when also the highest offshore wave heights were recorded. The wave height H_{m0}

was as large as 0.7 m and the offshore wave period T_{m02} was 3.6 s. However, these large drifter velocities could not be explained by the hydrodynamic conditions only and were presumably supported by a cross-offshore wind.

The offshore extent of the measured rip currents was in the order of 100 m offshore of the bar crest and stretched as far as 150 m. Large offshore extents were associated with strong offshore flows in which the drifters exited the surf zone. When the drifters were retained in the surf zone the offshore extent was only 30 to 60 m offshore of the bar crest.

The surf zone exit rate of drifters was high compared to other field observations [*Reniers et al.*, 2009]. This observation was attributed to the fact that the rip neck was not confined to the surf zone during the field experiments and that drifters got trapped in the tidal longshore current offshore of the rip channel.

Onshore of the rip channel the drifter measurements indicated the existence of a second circulation cell that may have caused the embayment onshore of the rip channels. In case of a meandering longshore current the drifters were observed to slow down onshore of the rip neck. This may be due to the lack of wave breaking in the channel so that the wave forcing in longshore direction that drives the longshore current is absent.

The drifters behaved consistently during the deployments and did not deviate notably from a mean trajectory. Along with the observation that drifters followed the same trajectory when they were deployed at the same location at an interval of one minute, this led to the conclusion that the rip is stationary for a period in the order of a few minutes.

A statistically significant correlation between the measured rip current strength and the ratio of offshore wave height over water depth on the bar H_{m0} / d was identified. Video images indicate that this relation is not linear but stagnates for large values of H_{m0} / d when wave breaking commences in the rip channel. No statistically significant relationship was determined between the wave period and the rip strength or the wave angle and the rip strength.

6 Hindcast Field Measurements

6.1 Introduction

The drifter measurements presented in Chapter 5 were used to validate an XBeach model of Egmond aan Zee. Each day of the field campaign a representative drifter deployment was selected for a hindcast. The chosen deployments comprised flow patterns of type 1 (circulating drifters) and 2 (alongshore advected drifters, see also Section 5.2.2). The measurements on August 26 were excluded from the hindcast model because the waves recorded at the wave buoy were directed offshore. These waves were generated locally by an offshore directed wind and therefore no reliable nearshore wave data could be derived from the buoy.

An overview of the replicated drifter deployments is provided in Table 6.1.

Table 6.1: Overview of the drifter deployments in the hindcast model

Parameter	*August 22 dpl.4*	*August 23 dpl.2*	*August 24 dpl.4*	*August 25 A dpl.3*
Offshore wave height H_{m0} [m]	0.51	0.36	0.50	0.59
Peak period T_p [s]	4	4.4	4.6	5.1
Wave angle θ_0 [°] (shore normal 277°)	288	325	285	229
One-sided directional spreading [°]	19	24	36	18
Tidal elevation [NAP m]	-0.57	-0.43	-0.31	-0.44
Tidal current [m/s] (positive northwards directed)	-0.32	-0.35	-0.34	-0.09
Flow pattern	Type 1	Type 2	Type 1/2	Type 2

In this chapter the key aspects of the XBeach model that were found to have implications on the hindcast of the field experiments are then discussed. These aspects include: the numerical grid, the tidal current and the roller model that was introduced in Section 3.3. The implementation of the tidal current into the XBeach model is discussed in Appendix C. Finally, the results are compared visually on the basis of drifter trajectories and by means of two parameters, which were the rip strength (see Section 3.4 for a definition) and the offshore extent of the rip current (Section 5.2.3).

6.2 Model calibration

The model was calibrated with regard to the numerical grid resolution, tidal driven currents and the roller induced viscosity. The results of the model calibration are presented in

Table 6.2. The measured value is presented first followed by the results of the base case configuration. This configuration consisted of a variable grid size in cross-shore direction, a tidal current and the roller viscosity scale factor set to $\alpha_{roller} = 1$. Subsequent results are then presented for simulations that deviate from this base case.

Table 6.2 Measured and computed rip strength and rip extent for the four representative deployments and the deviation from the measured values in red.

Data set	*Aug. 22, dpl.4*		*Aug. 23, dpl.2*		*Aug. 24, dpl.4*		*Aug. 25 A, dpl.3*	
	Rip str. [m/s]	*Rip extent [m]*	*Rip str. [m/s]*	*Rip extent [m]*	*Rip str. [m/s]*	*Rip extent [m]*	*Rip str. [m/s]*	*Rip extent [m]*
Measurement	0.29	62	0.24	95	0.21	75	0.55	106
Base configuration	0.25 -0.04	60 -2	0.20 -0.04	45 -50	0.26 +0.05	68 -7	0.33 -0.22	60 -36
Resolution 20x20 m	0.14 -0.15	56 -6	0.10 -0.14	29 -66	0.15 -0.06	64 -11	0.04 -0.51	13 -93
Resolution 5x5 m	0.27 -0.02	64 +2	0.16 -0.08	55 -40	0.28 +0.07	72 -3	0.36 -0.19	(118) +12
Without tidal current	0.25 -0.04	144 +82	0.19 -0.05	100 +5	0.25 -0.04	120 +45	0.37 -0.18	68 -38
$\alpha_{roller} = 0.1$	0.27 -0.02	60 -2	0.11 -0.04	46 -49	0.27 +0.06	66 -9	0.35 -0.20	63 -33

Numerical grid

The choice of the numerical grid was highly dependent on the nearshore bathymetry. It was anticipated that at least five grid cells in the cross-section of a channel would be necessary to resolve the flow within the channel. The width of the rip channel was ~100 m. Thus, a grid spacing of 20 m in the alongshore was expected to resolve the flow in the rip channel accurately. However, the feeder channel was only ~30 m wide. As the flow in the channel behind the bar feeds the rip it was crucial to have a sufficient resolution in the feeder channel.

Simulations with various grid resolutions ranging from 5 x 5 to 20 x 20 m indicated that a cross-shore grid spacing as fine as 5 m was required in the nearshore region. Simulations on coarser grids produced weaker rip current flow because the feeder current was not resolved accurately. Furthermore, the bathymetry was altered when it was interpolated on a coarser grid. As a result the bar was less pronounced and the channel was wider. To improve the computational efficiency a grid with varying cross-shore cell size was tested, ranging from 5 m in the nearshore to 10 m at the offshore boundary. The alongshore grid spacing was set to 10 m. This grid produced similar results to a 5 x 5 m grid, but reduced the computational time by factor 8.

Roller induced viscosity

In Section 3.3 it was shown that the roller induced viscosity caused substantial instabilities in the laboratory scale rip current. Because the effect of viscosity is scale dependent its influence was tested again in this model with field site dimensions with $\alpha_{roller} = 0.1$ and $\alpha_{roller} = 1$. The results of these simulations showed that the influence of α_{roller} was negligible for site scale rip currents (for drifter trajectories see Appendix C).

Tidal current

The 'flow hotstart' option introduced into the XBeach model (Appendix C) produced stable results that agreed reasonably well with the velocities from the Kuststrook model (Figure 6.1).

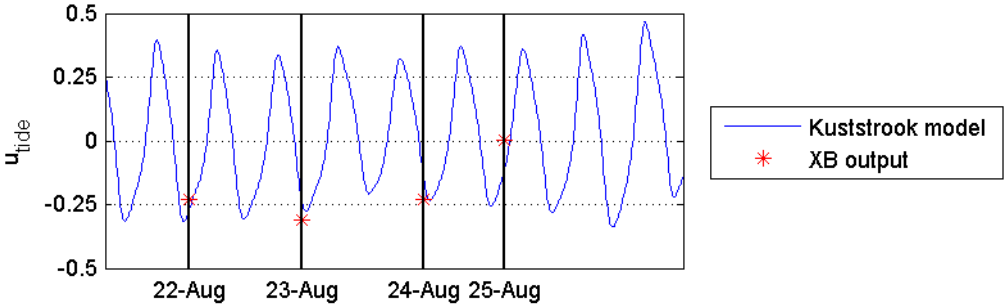

Figure 6.1 Comparison of the tidal current obtained from the Kuststrook model and the XBeach model output of the alongshore current at the offshore boundary.

Simulations for which a tidal current was not implemented did not replicate the alongshore advection of the drifters that was observed in the field. For example, a hindcast of August 23 dpl.2 that consisted of a large (47°with the shore normal) angle of wave incidence resulted in the drifters (once beyond the bar crest) floating offshore rather than floating southward (Figure 6.2).

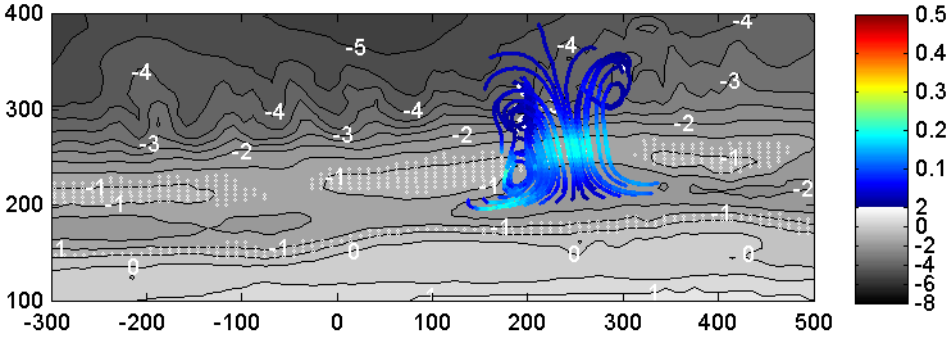

Figure 6.2 Simulated drifter paths for August 23, dpl.2 without tidal current. The white circles indicate areas of wave dissipation.

In simulations with a tidal current the drifters were advected initially alongshore as it was observed in the field (Figure 6.3). This shows that obliquely incident waves alone do not suffice to cause the drifter's deflection offshore of the bar and that it is solely the tide that triggers the alongshore advection of drifters.

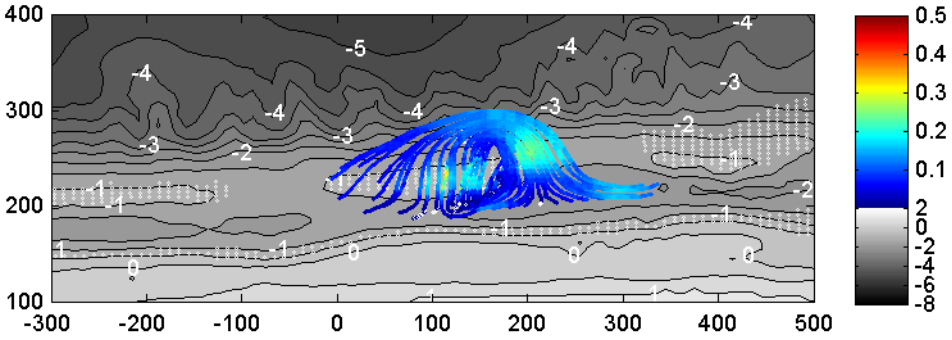

Figure 6.3 Simulated drifter paths for August 23, dpl.2 with tidal current. The white circles indicate areas of wave dissipation.

6.3 Results

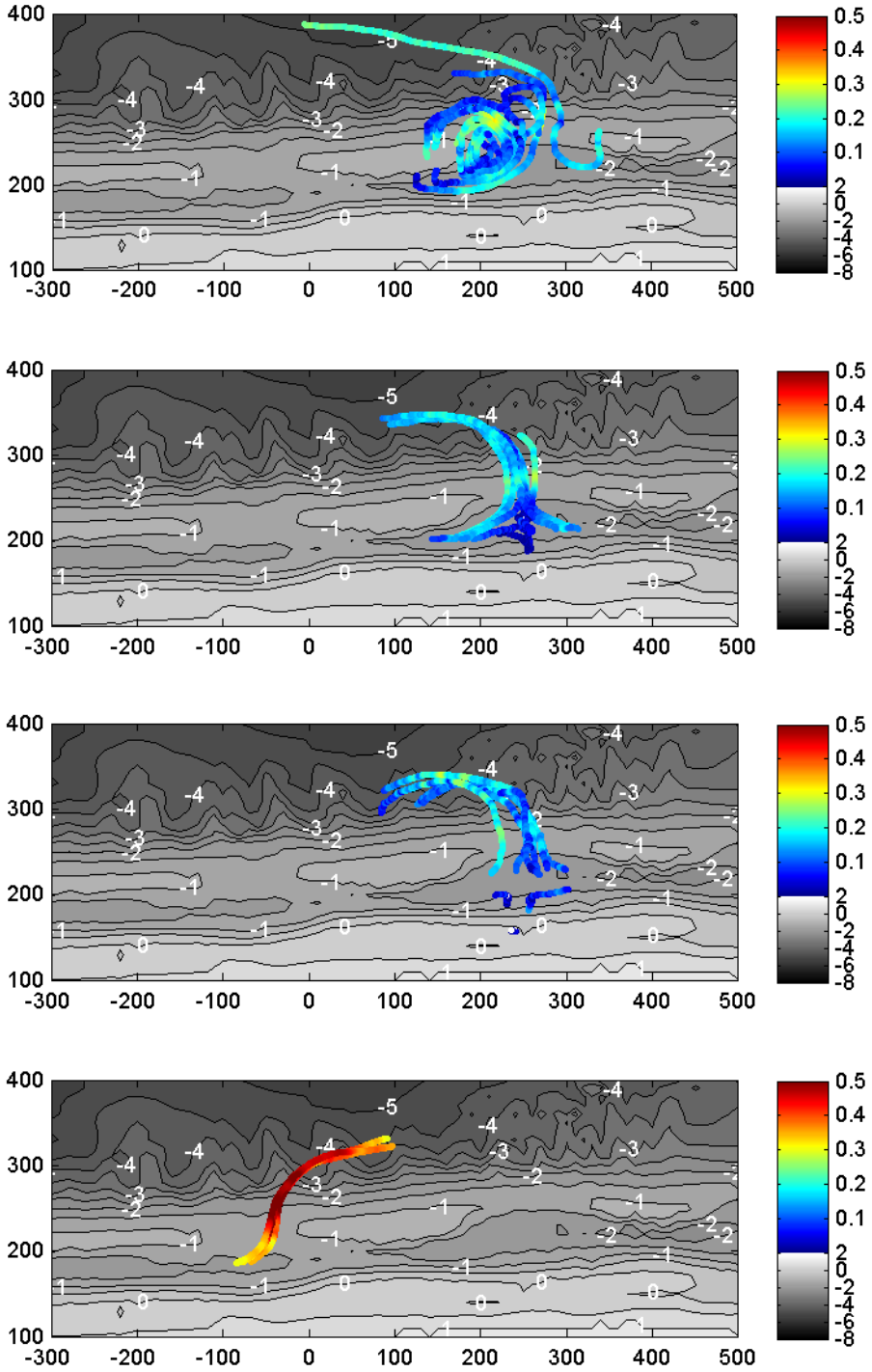

Figure 6.4 Measured drifter paths, from top to bottom: August 22 dpl.4, August 23 dpl.2, August 24 dpl.4, August 25 am dpl.3. The colours indicate drifter velocities in m/s.

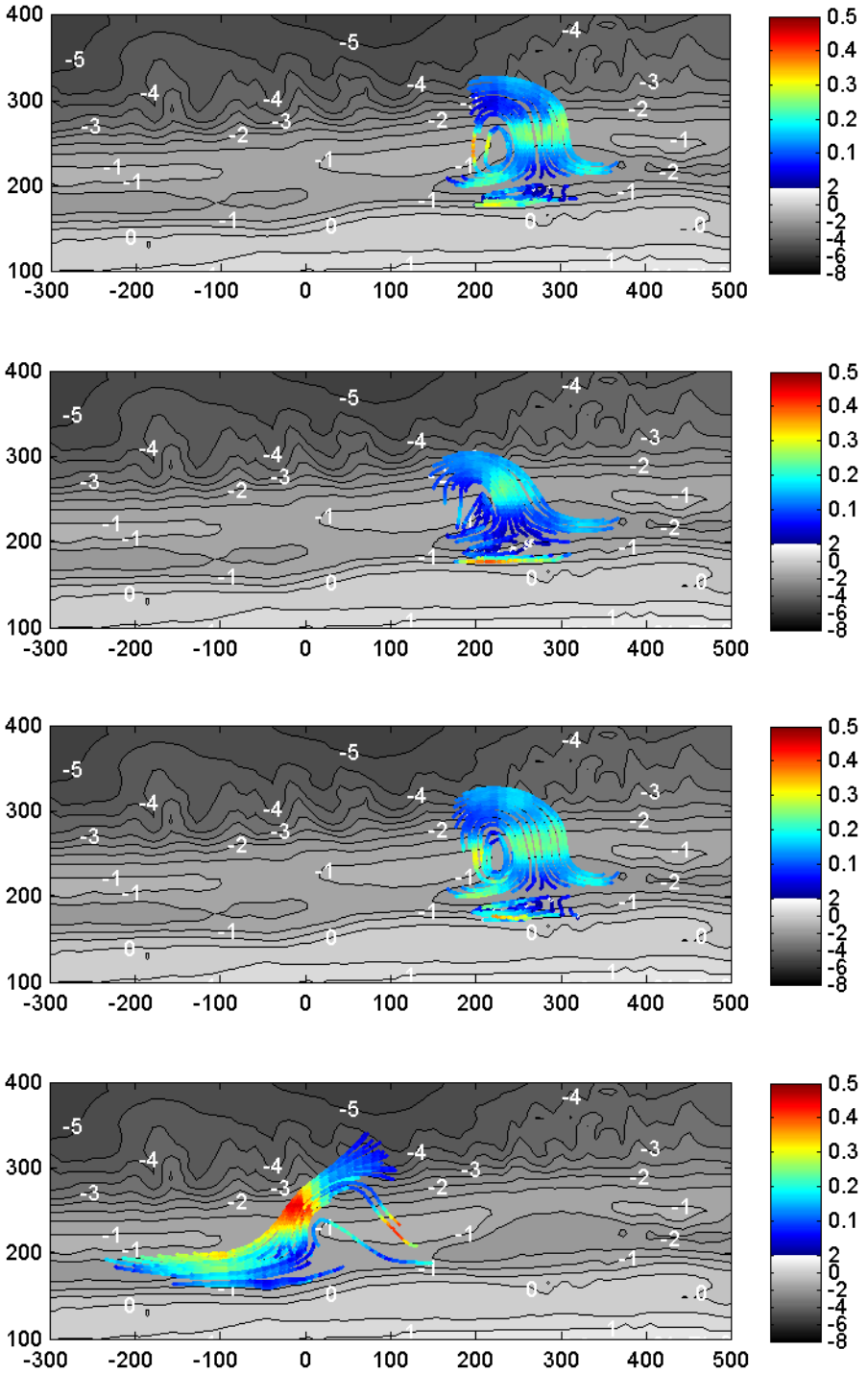

Figure 6.5 Drifter trajectories in the model simulated with the base configuration. The model is driven by stationary waves and comprises tidal currents. The colours indicate drifter velocities in m/s.

The base configuration that comprised a variable grid size in cross-shore direction, tidal current and a roller viscosity with scale factor $\alpha_{roller} = 1$ provided the best agreement with the measured drifter data (Table 6.2). A graphical comparison of the measured trajectories against the base configuration is provided in

Figure 6.4 and Figure 6.5.

The rip current features that were identified in the field study (Section 5.2.2) were reproduced in the hindcast model. The similarities and differences between the modelled and observed features are:

- The circular drifter movement on August 22 during dpl.4 was reproduced (Figure 6.5, top panel) while the exit of the single drifter was not reproduced.

The deflection of the drifters in southward direction on August 23 and 24 was observed in the model (Figure 6.5, 2nd and 3rd panel from the top). But the model suggests a shoreward return of the drifters over the bar that was not observed in the field. This discrepancy was explained by the rip current extending further offshore in the field than in the model (compare measured rip trajectories in

- Figure 6.4 and modelled trajectories in Figure 6.5). As a consequence the drifters in the model remain closer to the surf zone edge where they are subjected to a stronger Stokes drift. The lesser rip extent in the model was associated with the vertical flow structure offshore of the rip channel and is discussed in detail in Section 6.4.
- The area of stagnant or slight onshore directed flow onshore of the rip channel on August 22 and 23 was captured in the model and was identified as a feature of the second circulation cell (Section 2.3).
- On August 25 the drifter trajectory is modelled fairly well, but the strength of the rip current is significantly underestimated (measured: 0.55 m/s, computed: 0.32 m/s). It is likely that the offshore current was enhanced by a cross-offshore wind (140°N, 4 m/s). With the wave-driven current being northwards directed the rip current was orientated north-westwards in the rip channel and thus, in line with the wind direction. Offshore of the bar the weak opposite directed tidal current towards the South may have caused the drifters to move far offshore (106 m from the bar crest).
- The rip strength was slightly underestimated in the hindcast of August 22 and 23. Detailed analysis of the laboratory experiment (Section 3.3) revealed that the wave height evolution in an opposing current was not modelled accurately. The wave breaking was initiated too far offshore and the maximum wave heights were underestimated. As a consequence offshore directed velocities were also slightly underestimated.

6.4 Discussion of the vertical flow structure

The rip strength within the channel was predicted fairly well by the model however the offshore extent of the rip current was consistently underestimated in all simulations (apart from the model results that excluded tidal currents). This was attributed to the vertical flow structure offshore of the rip channel.

In a laboratory experiment, *Haas and Svendsen* [2002] measured velocity profiles offshore and within the rip channel. While the velocity profile was nearly depth uniform within the channel it showed a significant variation with depth offshore of the channel (Figure 6.6, left), with large offshore directed velocities near the surface and slight onshore directed velocities

near the bed. XBeach is a 2DH model and only distinguishes between a depth averaged Generalised Lagrangian Mean (GLM) velocity u^L and the Eulerian velocity beneath wave trough level u^E (Figure 6.6, right). The difference between those two velocities is the Stokes velocity:

$$u^E = u^L - u^s \tag{6.1}$$

The Stokes drift acts in direction of wave propagation and is composed of the net flux of mass between wave trough and wave crest level and the mass flux in the roller:

$$u = \frac{E_w}{\rho h c} + \frac{2E_r}{\rho h c} \tag{6.2}$$

where E_w is the wave energy, E_r the roller energy, ρ the water density, h the water depth and c the wave celerity. The shallow water equations in XBeach are solved for the GLM velocities that are applied to the drifters. The Stokes drift may be close to zero, but is never offshore directed. Thus, offshore of the rip channel, XBeach underestimates the flow velocities in the upper water layer and the drifters float at lower velocities. As a consequence the modelled drifters did not float as far offshore as observed in the field.

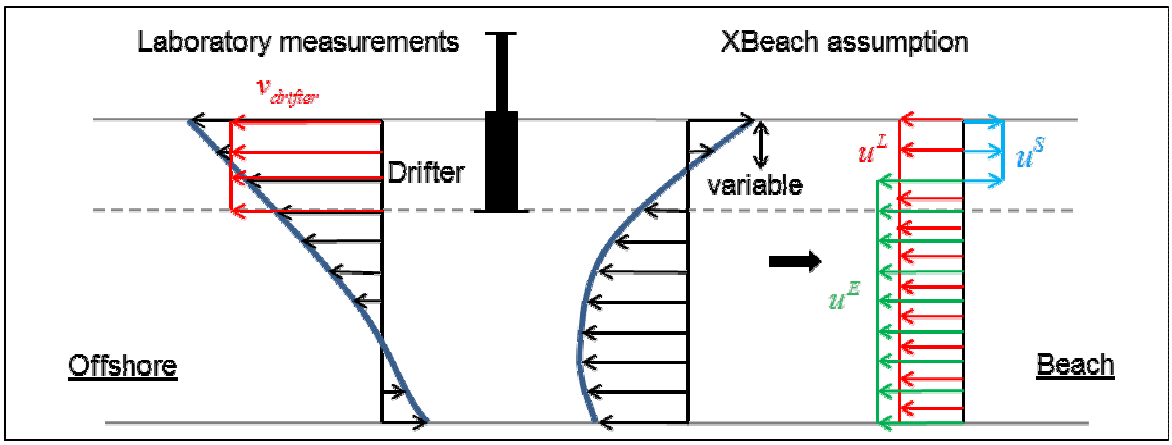

Figure 6.6 Vertical flow structure just offshore of the rip channel. Left: Measurements in the laboratory [Haas and Svendsen, 2002]. Right: Flow assumption and implementation in XBeach. Drifters in XBeach move with the Generalised Lagrangian Mean velocity u^L (red).

The specific vertical flow structure offshore of the rip channel may also have implications for sediment transport modelling. While the near surface velocities are underestimated in XBeach the near bed velocities are overestimated or even directed in the opposite direction. The near bed velocities determine the bottom shear stresses and are approximated in XBeach with the Eulerian velocity. As a result the offshore sediment transport may be overestimated within rip channels. However, sediment transport and bed level changes were not investigated in the present study.

6.5 Conclusions

A stationary wave driver drove the hindcast model and reproduced the field observations with respect to the drifter trajectories, the rip strength and the rip extent reasonably well. The key observations that were made in the set-up and simulation of rip currents with the numerical model XBeach are:

- The cross-shore resolution must be sufficiently high ($\Delta x = 5$ m) in the nearshore zone to resolve the flow in the feeder channel.
- The tidal current has an important impact on the flow pattern (the influence of the tidal current is examined further in Chapter 7).
- The stationary wave driver efficiently and accurately reproduced the rip current velocities within the rip neck observed in the field and measured in the laboratory (Section 3.3).
- In contrast to the simulations of the small scale laboratory experiment, the roller induced viscosity did not notably affect the results. The sensitivity analysis was performed with the default value $\alpha_{roller} = 1$.
- The offshore extent of the rip current is underestimated because the 2DH XBeach model lacks information about the vertical flow structure offshore of the rip channel.

A sensitivity analysis was conducted in XBeach to determine the influence of different geometric and hydrodynamic parameters based upon the successful reproduction of the field observations and is discussed in Chapter 7.

7 Sensitivity Analysis

7.1 Introduction

A sensitivity analysis was conducted with the aim to identify the hydrodynamic and geometric parameters that govern the initiation and mean properties of rip currents at Egmond aan Zee. The numerical model presented in this chapter serves to complement and to understand the observations made in the field. During the field campaign rip currents were measured under a small range of conditions (Section 4.4) and consequently the observed rip current features could not be attributed unambiguously to specific parameters. Therefore, the validated model was used to test a broad range of hydrodynamic and geometric conditions and to examine the influence of various parameters independently.

A large number of hydrodynamic and geometric parameters exist that may influence rip current properties. As a consequence, only a selection of the most prominent parameters was investigated. The hydrodynamic parameters considered were the water level, wave height, wave period and wave angle. While the present wave conditions can be obtained from elaborated wave forecast models, the underlying bathymetry yields large uncertainties in modelling real time rip current conditions. The bathymetry can change at a time scale of weeks, days or even hours. Very detailed surveys of the rip current bathymetry would need to be performed frequently. Therefore, this numerical study treats the sensitivity of rip currents to geometric features. In their study, Svendsen et al. [2000] already pointed out that the cross-shore position of the bar has a significant influence on the rip current strength. The closer to the shore the bar is located the stronger the rip. While the location of surf zone features can be obtained reliably from video images such as Argus [*van Enckevort et al.*, 2004], the depth of the troughs and channels is afflicted with larger uncertainties, in particular in the very nearshore zone [*van Dongeren et al.*, 2008]. The sensitivity of the model to two geometrical features of the rip channel was investigated: the channel depth and width.

7.2 Methodology

A reference case based on findings earlier in this study (Section 3.4) was designed from which one parameter was changed at a time. An overview of the reference settings is given in Table 7.2 Overview of the tested parameters.Table 7.1. The water level was set to NAP -0.3 m because rip currents were favoured with water levels below NAP +0 m during the field campaign. The range of values that were tested for each parameter are summarised in Table 7.2.

Table 7.1 Input for the reference case

Parameter	*Value*
Wave forcing	Stationary
Wave height H_{m0}	0.5 m
Peak period T_p	5 s
Wave angle θ	277°(shore normal)
Water level z_0	NAP -0.3 m
Tidal current u_{tide}	0 m/s
Rip channel depth d_r (relative to bar crest)	0.5 m
Rip channel width w_r	110 m

Bar crest height z_b	NAP -0.83 m

Table 7.2 Overview of the tested parameters.

Hydrodynamic Parameters	
Wave height H_{m0} [m]	0.25 : 0.25 : 2
Peak period T_p [s]	4 : 1 : 10
Wave angle θ [°] (shore normal 277°)	277 : 10 : 327
Water level z_0 [m]	-0.8 : 0.2 : 0.4
Tidal current at the offshore boundary (d=10 m) [m/s]	0 : 0.1 : 0.5
Geometric Parameters	
Channel depth d_r (relative to bar crest height) [m]	0.3 : 0.2 : 1.3
Channel width w_r [m]	50 : 20 : 170

The sensitivity analysis simulations were performed on a smooth and symmetric bathymetry based on Rip 2 as the bar adjacent to this rip was nearly alongshore uniform. The use of this bathymetry excluded the effects or irregularities and asymmetry. The method adopted to develop and alter the smoothed bathymetry is summarised below.

7.2.1 Development of smoothed bathymetry

Initially, mean profiles were determined for the area South of the rip channel, for the channel itself and the area North of the channel. The mean profiles were then replicated in alongshore direction. The transition zones between the mean bar and channel profiles were interpolated cubically on the initial grid. Subsequently, the Northern half of the smooth bathymetry was mirrored so that the bathymetry was symmetric.

The difference between the smoothed bathymetry and the real bathymetry represented the small scale irregularities that were not associated with the channel morphology. The irregularities were in the order of 0.5 m. An irregular but symmetric bathymetry was obtained by adding the small scale irregularities to the smooth symmetric bathymetry. It was shown that the assumption of a smooth symmetric bottom did not influence the model results significantly (Section 7.3.1).

7.2.2 Alteration of smooth bathymetry

Depth

To assess the sensitivity to geometric parameters the rip channel depth was altered by firstly, conducting a linear interpolation of the bed level between the points offshore and onshore of the rip channel. The linear interpolation was then subtracted from the initial profile. The difference profile between the original and the interpolated profile was multiplied with various factors ranging from 0.2 to 1.2 and then summed again to the linearly interpolated profile (Figure 7.1). This resulted in rip channels that were shallower or deeper than the original (Figure 7.2).

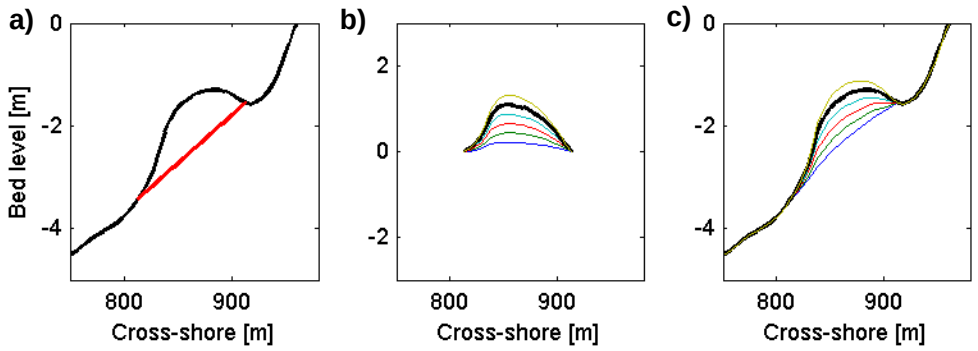

Figure 7.1 Superposition of the rip channel 'berm' from left to right: (a) Original profile (black) and linear interpolation (red), (b) modification of the berm and (c) superposition of the linear profile and the modified rip channel berm

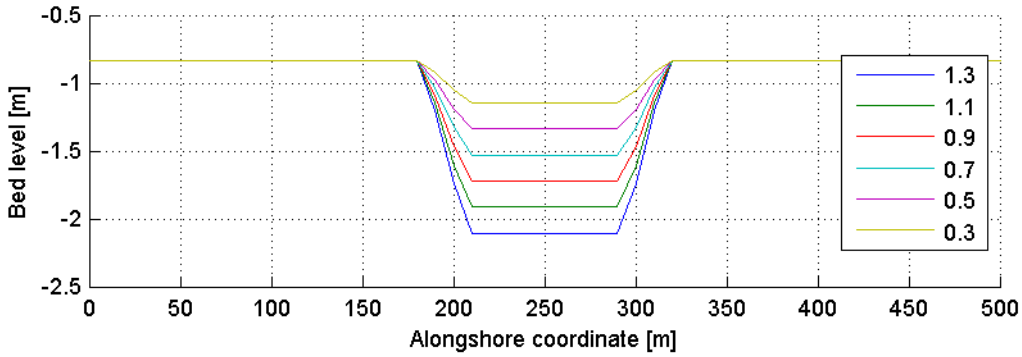

Figure 7.2 Alongshore transect through the bar crest and the rip channel. The plot shows the various tested rip channel depths ranging from 0.1 to 1.3 m.

Width

To alter the channel width the rip channel was extended in alongshore direction. This resulted in bathymetries with a rip channel width ranging from w_r = 50 to 170 m (Figure 7.3). For narrow rip channels (50, 70 and 90 m) the cross-shore grid spacing was reduced to Δx = 5 m to resolve the flow within the rip channel accurately.

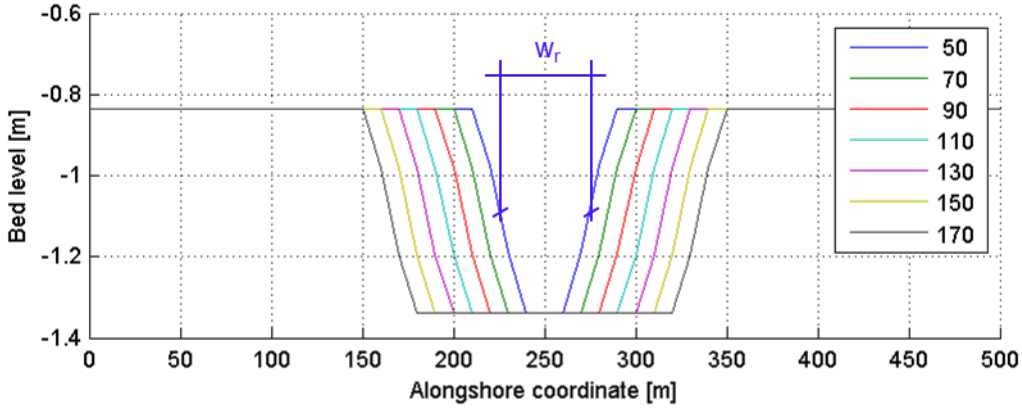

Figure 7.3 Rip channel width ranging from 50 to 170 m

7.3 Results

7.3.1 Small scale bed irregularities

The influence of small scale bed irregularities O(0.5 m) on the rip current flow pattern was investigated by modelling the reference case conditions on a smooth and an irregular bathymetry.

It was observed that the irregular bathymetry induced small spatial fluctuations of the rip current, but did not affect the mean flow (Figure 7.4). The simulated drifter trajectories (Figure 7.5) on a bathymetry with small irregularities O(0.5 m) (left) and a smooth bathymetry (right) did not change significantly and justified the use of the idealised bathymetry. The large scale features measured in the field such as bar and channel location and their depth are preserved in this idealised bathymetry.

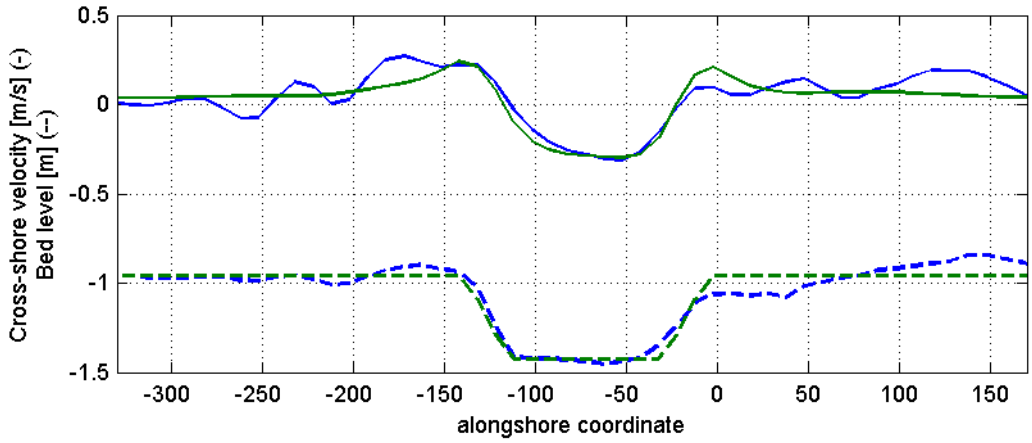

Figure 7.4 Alongshore transect of the cross-shore velocity u (solid line) with smooth bathymetry (green) and irregular bathymetry (blue) and the underlying alongshore bed profile (dashed line).

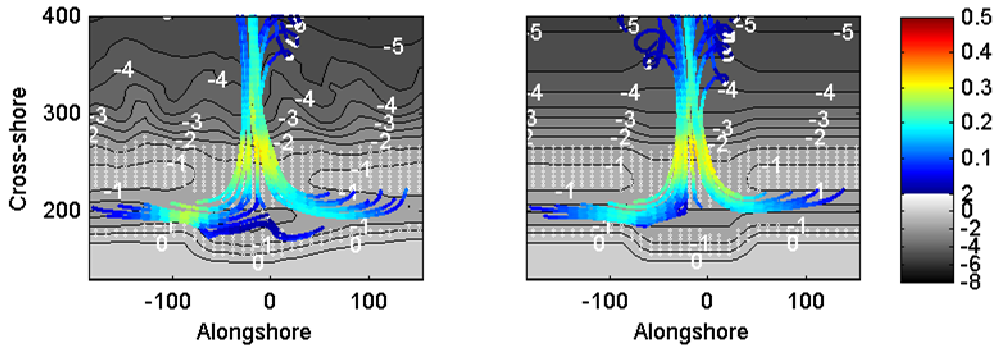

Figure 7.5 Drifter trajectories simulated on an irregular bathymetry (left) and on a smooth bathymetry (right). The colours indicate drifter velocities in m/s.

7.3.2 Water level, wave height and wave period

The influence of wave height, water level and wave period was tested separately. The simulations for each parameter were performed with channel depths that ranged from 0.3 to 1.3 m.

The results of the simulations for differing wave height and channel depth are presented in Figure 7.6. The rip strength increased with increasing wave height; however, the rip channel depth limited the maximum possible rip strength. For channels deeper than 0.9 m, the rip strength was not affected by wave heights up to 0.5 m while in shallower channels, the rip strength was affected significantly for wave heights smaller than 0.5 m.

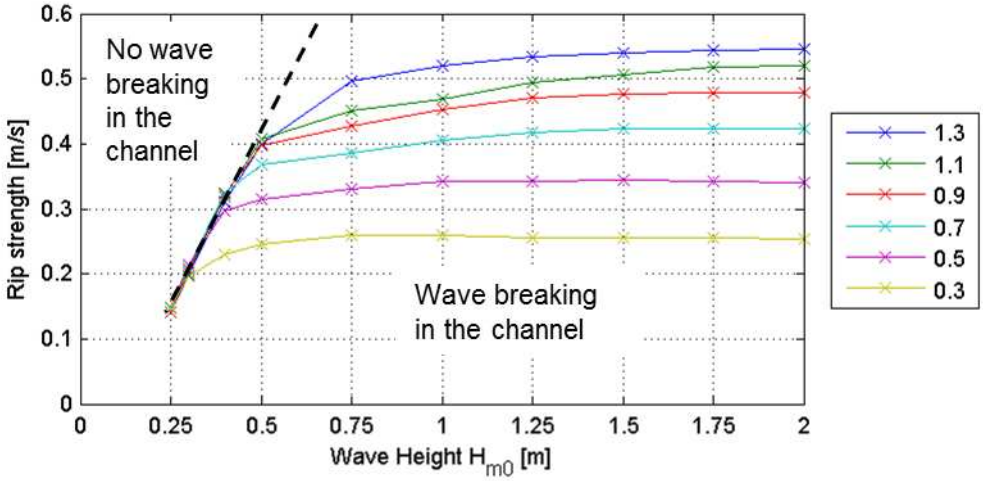

Figure 7.6 Rip strength vs. offshore wave height for various rip channel depths (see legend [m]). The rip channel depth is defined as the height difference between bar crest and rip channel trough.

The rip strength likewise increased with decreasing water level (Figure 7.7) but consistent with the wave height observations, the maximum rip strength was limited by the rip channel depth. Furthermore, the rip strength did not increase monotonously, but reached its maximum at a water level of -0.6 m and decreased again for lower water levels. At a water level of -0.8 m the bar crest (z_b = -0.84 m) is nearly emerged such that the mass transport over the bar is limited.

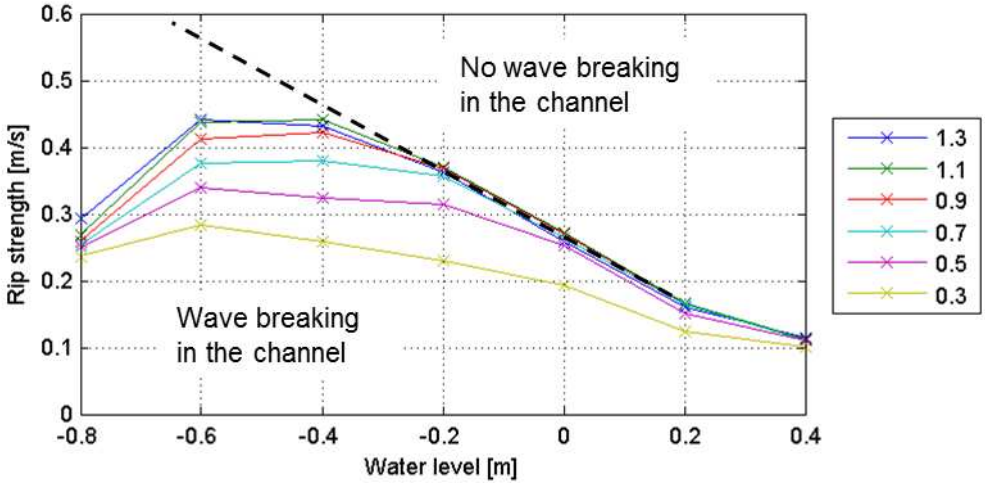

Figure 7.7 Rip strength vs. water level for various rip channel depths (see legend [m]). The rip channel depth is defined as the height difference between bar crest and rip channel trough.

Wind waves, in comparison to swell waves, are characterised by shorter periods and broader directional and frequency spreading. The use of stationary waves disregarded the effect of frequency spreading and the resultant wave grouping. In combination with stationary waves directional spreading only affects the refraction and diffraction at the tip of the bars, but does

not generate an alongshore varying wave field that may have an impact on the hydrodynamic forcing. Therefore, in this study only the influence of the wave period was investigated. An increased wave period resulted in a slight increase in rip strength (Figure 7.8) but this effect was shadowed by the limitation imposed by shallower rip channels (d_r = 0.5 … 0.9 m). However, even in deep channels (d_r > 0.9 m) the impact of the wave period was small in comparison with wave height and water level.

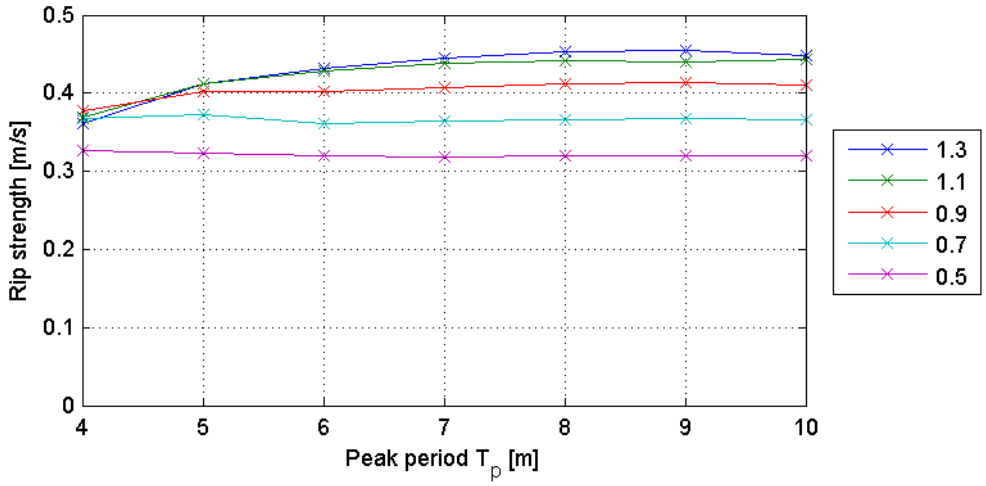

Figure 7.8 Rip strength vs. Peak period for various rip channel depths (see legend [m]). The rip channel depth is defined as the height difference between bar crest and rip channel trough.

7.3.3 Longshore currents

Longshore currents are generated by obliquely incident waves, the tide or by cross-shore winds. The latter was not addressed in this analysis. First, the influence of the wave angle on rip current strength and flow patterns was investigated and then varying tidal velocities were tested.

The effect of the wave angle was investigated in combination with the rip channel width. The rip strength was not significantly affected by the wave angle (Figure 7.9) for a site specific channel width w_r = O(100 m) or wider. Even for very large wave angles (327°N, 50° w.r.t. shore normal) the rip strength was not reduced significantly. In contrast, a subtle rip strength maximum appears with wave angles of 317°N (40° with the shore normal). This is close to a wave angle of 45° for which the alongshore wave for cing is the largest (Section 2.2) and thus wave-driven longshore currents are maximum. However, for a narrow rip channel (w_r = 50 m), the wave angle had a significant negative influence on the rip strength. This was similar to the results obtained from the synthetic model of Egmond aan Zee (see Section 3.4). Provided that the offshore velocities were not negatively influenced by the wave angle, the rip strength was larger in narrow channels due to flow constriction.

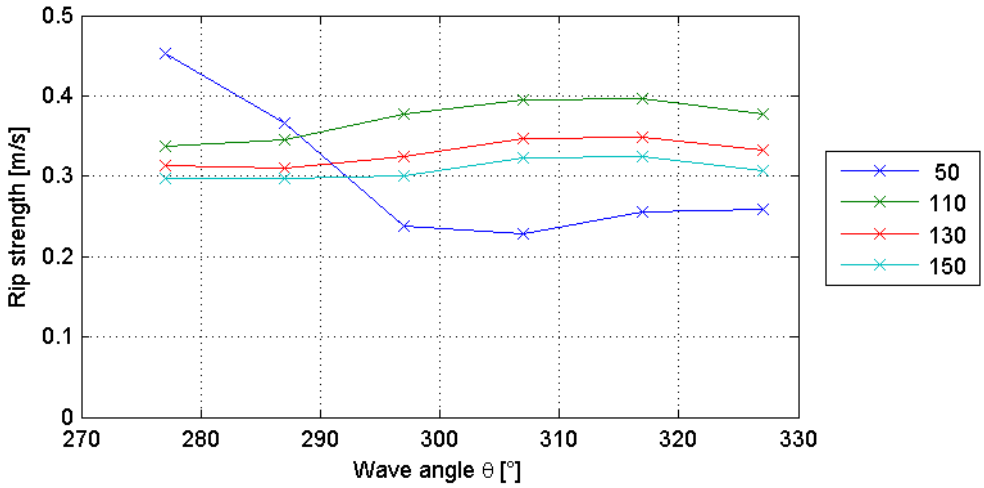

Figure 7.9 Rip strength vs. wave angle for various rip channel widths ranging from w_r = 50 to 150 m.

Along with the rip strength the wave-driven longshore current also modulated the flow pattern. Introduction of the longshore current resulted in the rip no longer being centred in the channel, but biased to the downdrift side of the channel (Figure 7.10). While the rip strength (synonymous for the maximum cross-shore velocity) amplified only slightly with large wave angles, the total velocity increased notably. The increase of the total velocity may be either caused by a streamlining effect along the bar head and/or by the enhancement of the feeder current through wave-driven longshore currents. Obliquely incident waves favoured drifter circulations because the drifters were forced closer to the bar head. There, the roller induced onshore mass flux was larger due to wave dissipation and favoured drifter circulation. Drifters that floated along the centre line of the channel were found to be less prone to return shoreward.

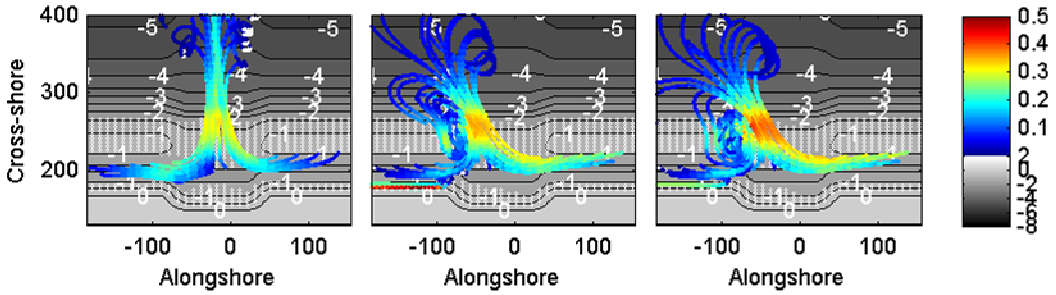

Figure 7.10 From left to right: Drifter trajectories for simulations with θ_0 = 277°(shore normal), θ_0 = 297°and θ_0 = 317°. The white circles indicate area of wave di ssipation and the colours indicate drifter velocities in m/s.

Longshore currents can also originate from the tide. The tidal velocity in the model was defined at the offshore boundary of the numerical domain at a water depth of 10 m and was modelled with the 'flow hotstart' option (Appendix C).

The tidal current did not modify the strength of the rip current, but had a significant influence on the behaviour of the rip offshore of the bar. The tidal current forced the rip to deflect in alongshore direction once it had passed the bar. While the drifters floated along the bar they remained closer to the surf zone edge. There they were subject to a stronger Stokes drift (induced by shoaling waves in the shoaling zone or by the bore of broken waves in the surf zone) and tended to return over the bar (Figure 7.11, middle). In stronger tidal currents the drifters were advected over a larger longshore distance before they eventually returned

shoreward (Figure 7.11, right). The model results with tidal longshore currents resembled the flow pattern type 2 of an advection alongshore observed in the field (Section 5.2.2). A strong tidal current was also observed to restrain the downdrift feeder current (Figure 7.11, right).

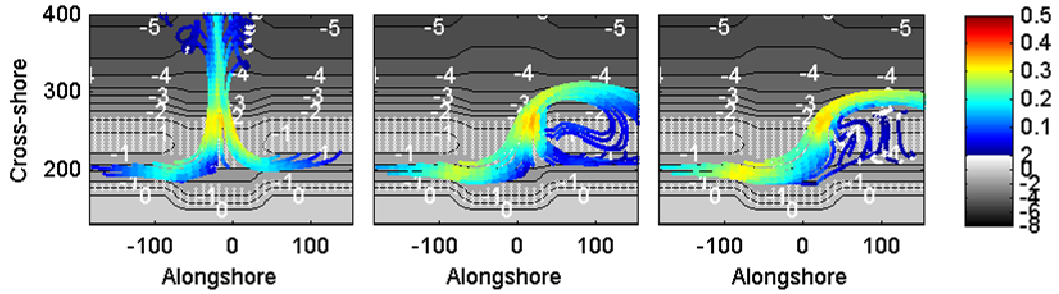

Figure 7.11 From left to right: Drifter trajectories for simulations with u_{tide} = 0 (shore normal), u_{tide} = 0.3 m/s and u_{tide} = 0.5 m/s (tidal velocities at 10 m depth). The white circles indicate area of wave dissipation and the colours indicate drifter velocities in m/s.

7.4 Discussion

7.4.1 Wave dissipation

It was shown that the rip strength increased with increasing wave height and decreasing water level. This is consistent with the field observations that showed evidence of a positive dependence of the rip strength on the wave height over water depth on the bar ratio H_{m0} / d. The field results also suggested that there was an upper limit to the rip strength (Section 5.4). However, due to the small range of measured conditions this hypothesis could not be verified directly from field data. In the model two mechanisms could be identified that explain an upper limit to the rip strength.

Firstly, with large wave heights H_{m0} and a limited rip channel depth, wave breaking commences in the rip channel (see Figure 7.13). In Section 2.2 the generation of rip currents was explained by the wave forcing that is balanced by a water level set-up behind the bar:

$$\frac{F_x}{\rho h} = -g\frac{d\eta}{dx} \tag{7.1}$$

The water level set-up results in the movement of water alongshore that converges at the rip neck (where the water level set-up is usually smaller) into an offshore directed flow. When wave breaking commences in the channel, the water level set-up in the channel will also be higher (Figure 7.12) and the alongshore water level gradient that drives the rip current does not increase any further.

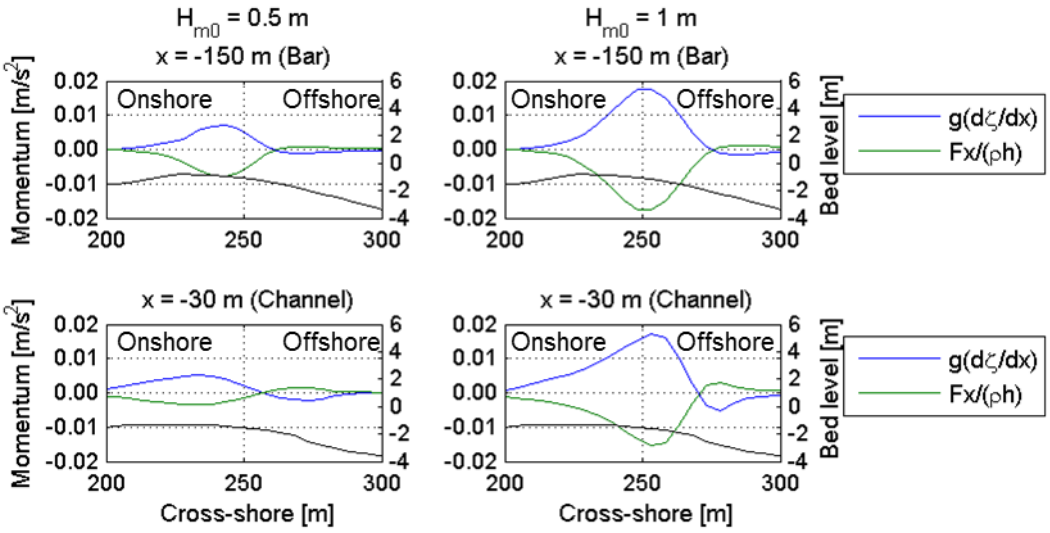

Figure 7.12 Momentum balance of the pressure gradient g(dη/dx) and the wave forcing $F_x/\rho h$ over the bar (upper panel) and in the channel (lower panel) for H_{m0} = 0.5 m (left) and H_{m0} = 1 m (right). With H_{m0} = 1 m the water level set-up is higher on the bar, but also in the channel.

Deeper channels allow waves to propagate closer to the shore line before they break (Figure 7.14) and thus no set up is induced in the channel. Consequently, it is the dissipation gradient from the bar to the rip channel that determines the alongshore water level gradient and the strength of the offshore current. The wave dissipation gradient is determined by three parameters, the wave height, the water depth over the bar and the depth of the rip channel with respect to the bar crest.

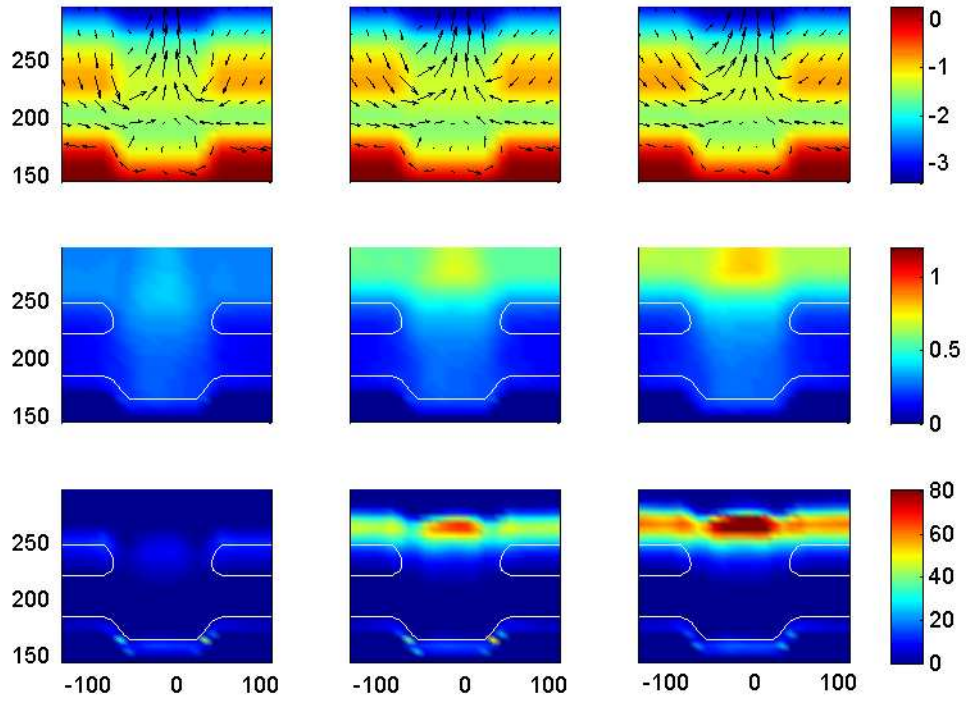

Figure 7.13 From top to bottom: Bed level and Lagrangian velocity vectors, wave height and wave dissipation for various wave heights. From left to right: H_{m0} = 0.5 m, 1.0 m and 1.5 m. The rip channel depth is d_r = 0.5 m.

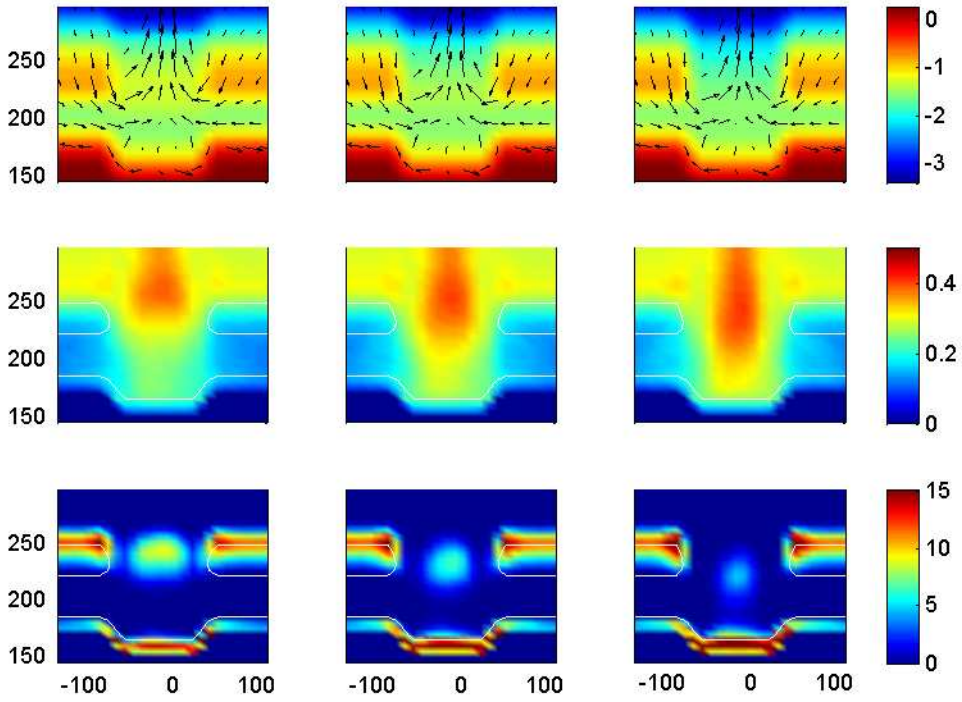

Figure 7.14 From top to bottom: Bed level and Lagrangian velocity vectors, wave height and wave dissipation for various channel depths. From left to right: d_r = 0.5 m, 0.7 m and 0.9 m. The wave height is H_{m0} = 0.5 m.

Secondly, the rip strength did not increase for very large waves because waves larger than 1.5 m are filtered out by the outer bar so that they result in the same breaking wave height at the inner bar.

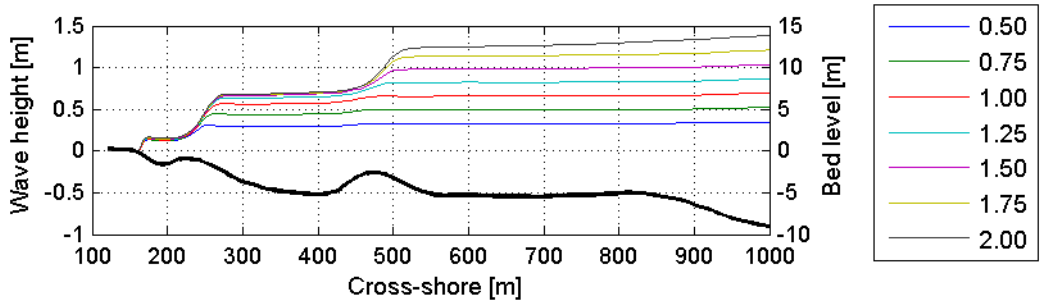

Figure 7.15 Cross-shore wave height evolution in a bar transect for offshore wave height ranging from 0.5 m to 2 m (see legend).

7.4.2 Wave shoaling

A minor increase in rip current strength was also observed for long period waves. The wave energy flux offshore equals the energy flux in the shoaling zone if there is no energy transfer with currents. This assumption holds for the bar profile where no offshore current opposes the incoming waves. The energy flux is the product of the wave group velocity and the wave energy and can be expressed in terms of the wave height:

$$\begin{aligned} \left[Ec_g \right]_0 &= \left[Ec_g \right]_{sh} \\ \Rightarrow \frac{1}{8}\rho g H_0^2 c_{g,0} &= \frac{1}{8}\rho g H_{sh}^2 c_{g,sh} \end{aligned} \tag{7.2}$$

Rearranging eq. (7.2) yields:

$$H_{sh} = \sqrt{\frac{c_{g,0}}{c_{g,sh}}} H_0 \tag{7.3}$$

and the group velocity c_g is given by:

$$\begin{aligned} c_g &= nc = n\frac{g}{\omega}\tanh(kd) \\ \text{or } c_g &= nc = n\sqrt{\frac{g}{k}\tanh(kd)} \\ \text{and } n &= \frac{1}{2}\left(1+\frac{2kd}{\sinh(2kd)}\right) \end{aligned} \tag{7.4}$$

and c is the phase velocity. In deep water ($\tanh(kd) \to 1$ and $n \to \frac{1}{2}$ for $kd \to \infty$) the group velocity simplifies to:

$$c_{g,0} = \frac{1}{2}\frac{g}{\omega} = \frac{1}{2}\frac{g}{2\pi}T \tag{7.5}$$

Whereas in shallow water ($\tanh(kd) \to kd$ and $n \to 1$ for $kd \to 0$) waves become less dispersive. That means that the group velocity depends less on the frequency and more on the local depth:

$$c_{g,sh} = \sqrt{\frac{g}{k}(kd)} = \sqrt{gd} \tag{7.6}$$

Substituting eq. (7.5) and eq.(7.6) in eq. (7.2) yields:

$$H_{sh} = \sqrt{\frac{g}{4\pi}T}\,\frac{H_0}{(gd)^{1/4}} \tag{7.7}$$

From eq. (7.7) it follows that the nearshore wave height increases for waves with larger periods. Thus, a larger period has a similar effect as larger wave heights. But the effect of the wave period is small with respect to the wave height, e.g. a duplication of the wave period has the same effect as a 25% increase in wave height. In Figure 7.8 the increase in rip strength with increasing wave period is only visible for the simulations done on a bathymetry with channels of 1.1 m and 1.3 m depth. In shallower channels the positive dependency of the rip strength on the wave period is shadowed by the effect of wave breaking in the channel.

7.4.3 Obliquely incident waves

The wave angle was not found to have an influence on the cross-shore velocity for channel widths observed at Egmond that were w_r = O(100 m). The cross-shore velocity was even slightly enhanced by large wave angles. Only for narrow rip channels (w_r = 50 m) did the rip strength decrease with wave angles ≥ 297° (20° with the shore normal).

An increase for small wave angles (up to 10° with the shore normal) was reported by *Aagaard et al.* [1997] who attributed their observation to an enhancement by wind-driven currents. Furthermore, *Haller et al.* [2002] recorded larger rip velocities with an angle of wave incidence of 10° in the laboratory. Consistent results were obtained by *Kumar et al.* [2011] in a numerical study. Thus, the observations described in literature are consistent with the results that were obtained with a narrow rip channel in this model. *Svendsen et al.* [2000] argued that with large wave angles the longshore current possesses enough inertia to bypass the rip channel and the circulation cells are not maintained anymore.

Previous studies were performed with rather narrow rip channels with respect to the wave height that together with the wave angle determines the strength of the wave-driven longshore current. The present study suggests that the inertia of the longshore current is not sufficient to bypass wider channels and that drifters still float offshore even with large wave angles.

Firstly, the behaviour of the wave-driven longshore current on a rip channelled beach was examined. When obliquely incident waves break they induce a wave forcing in alongshore direction F_y that drives an alongshore current following from the longshore NSWE:

$$\frac{dv}{dt} + u\frac{dv}{dx} + v\frac{dv}{dy} + DIFF + g\frac{d\eta}{dy} + \frac{\tau_{by}}{\rho h} - \frac{F_y}{\rho h} = 0 \tag{7.8}$$

It was assumed that the conditions are stationary and that the advection in cross-shore direction, the diffusion terms and the water level gradient in alongshore direction are negligible. The bottom stress was substituted by a quadratic friction term so that eq. (7.8) simplified to:

$$v\frac{dv}{dy} + c_f\frac{v|v|}{h} - \frac{F_y}{\rho h} = 0 \tag{7.9}$$

In the channel the water is deeper so that wave breaking is absent and the alongshore current can be determined analytically [see also *Smit et al.*, 2008]:

$$v(y) = \hat{v}\exp(-Cy) \tag{7.10}$$

where C is an integration constant and $\hat{v}$ is the alongshore velocity updrift of the channel. Thus, the alongshore current reduces exponentially in the channel (Figure 7.16).

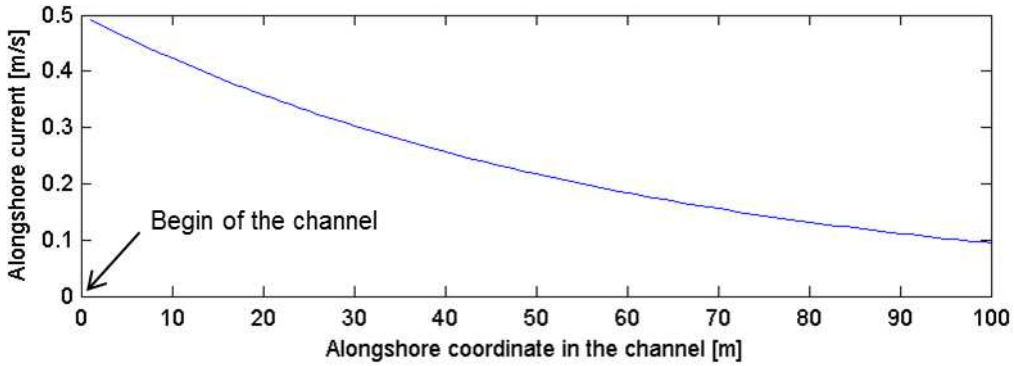

Figure 7.16 Analytically calculated alongshore velocity vs. alongshore coordinate in the channel. In the absence of wave breaking in the channel the longshre current reduces exponentially.

The modelled alongshore current did not follow exactly the analytical solution (Figure 7.17) mainly because of the assumptions made in the analytical solution. In particular the advection in cross-shore direction is not negligible in the rip channel. However, the alongshore velocities definitely decreased in the channel and they did so at the same rate for both, a narrow and a wide channel. The longshore current possessed enough inertia to bypass a narrow, but not a wide channel.

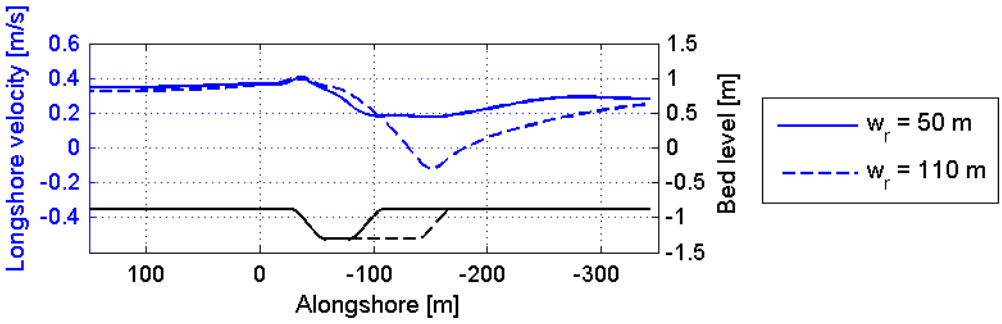

Figure 7.17 Simulated alongshore velocity vs. alongshore coordinate over a narrow channel (solid line) and wide channel (dashed line).

Figure 7.18 shows the velocity magnitude and vectors on a barred beach with incised rip channel (top) and a straight barred beach (middle). The discrepancy of the two velocity fields for each channel width is plotted in the bottom panel. This indicates that next to the wave-driven longshore current a circulation cell was still present in the total velocity field for both, a narrow and a wide rip channel. However, a wide channel (left) interrupted the longshore current completely such that longshore velocities on the downdrift bar were zero and only picked up in strength again further away from the rip channel. The plots of the velocity difference (bottom panel) show that in a wider channel the circulation cell was better maintained. Furthermore, the plot indicates that on a rip channelled beach the longshore current on the bar is weaker which may be attributed to part of the longshore flow being carried as feeder current in the trough between the bar and the beach.

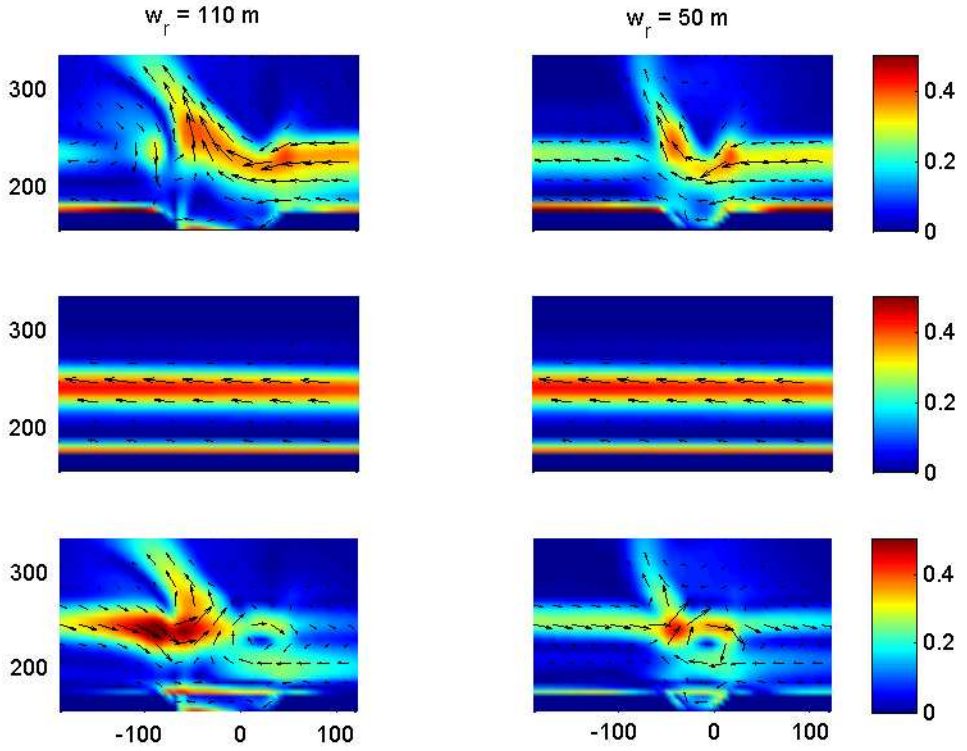

Figure 7.18 From top to bottom each width a channel width $w_r = 110$ m (left) and $w_r = 50$ m (right): Velocity magnitude and vectors on a barred beach with incised rip channel, on a straight barred beach and the velocity difference between a rip channelled beach and a straight barred beach. Note that the rightward directed current on the downdrift bar (bottom left) only indicates the lack of a longshore current over the bar downdrift of a wide channel.

The total flow field is thus, a balance between the wave-driven longshore current and the rip current circulation cell. In a wide channel the longshore current decreased to a greater extent and the rip circulation cell governed the total flow field. In contrast, in a narrow channel the longshore current decreased less and thus, dominated the total flow field.

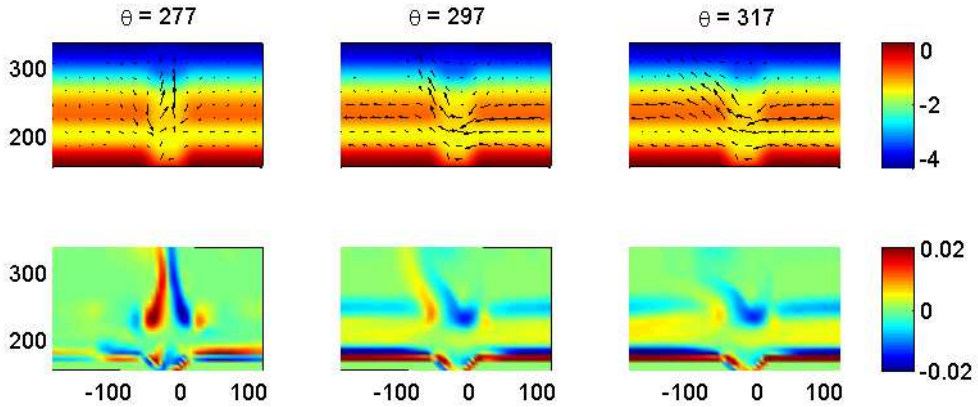

Figure 7.19 Simulations with a channel width $w_r = 50$ m. From top to bottom: Bed level and Lagrangian velocity vectors, wave height and vorticity. From left to right: $\theta = 277°$ (shore normal), $\theta = 297°$ and $\theta = 317°$. The wave height is Hm0 = 0.5 m and the channel depth $d_r = 0.5$ m.

The balance between the longshore current and the rip circulation cell is shown in the vorticity plots in Figure 7.19 (bottom panel). With normally incident waves and a narrow channel, the circulation cells were located close to each other and thus promoted a strong narrow offshore flow. With increasing wave angles the circulation cells vanished and the rip current ceased as the longshore current dominated. This is in line with the results of previous studies [*Kumar et al.*, 2011; *Svendsen et al.*, 2000].

The simulations showed that rip circulation cells in wide channels are maintained even with large wave angles so that the offshore velocities in the rip are not affected (Figure 7.20). In the field, the rip channel was 110 m wide and thus relatively wide with respect to the wave forcing (H_{m0} = 0.35 .. 0.7 m). The results of the numerical model explain why there was no correlation identified in the field data with respect to the wave angles. In contrast, the strongest rip was measured with an angle of wave incidence of 54°.

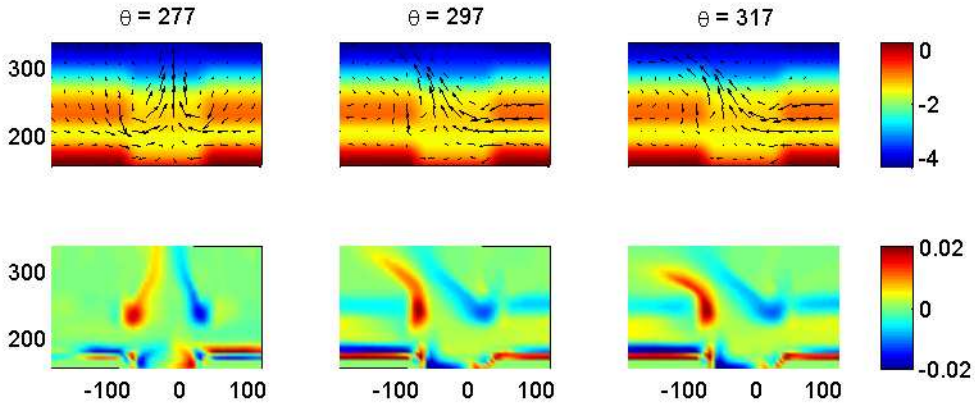

Figure 7.20 Simulations with a channel width w_r = 110 m. From top to bottom: Bed level and Lagrangian velocity vectors, wave height and vorticity. From left to right: θ = 277° (shore normal), θ = 297° and θ = 317°. The wave height is H_{m0} = 0.5 m and the channel depth d_r = 0.5 m.

The results of this sensitivity analysis show that the influence of the wave angle on the rip current depends on the balance between strength of the rip current circulation cell and the strength of the longshore current. The longshore velocity is determined not only by the wave angle, but also by the wave height. The tests have been conducted with a single wave height and the findings suggest that stronger longshore currents triggered by larger waves may possess enough inertia to bypass even wide channels.

7.4.4 Tidal longshore current

In the simulations conducted, the rip current was generally directed straight offshore and no drifters were retained in the surf zone. Drifter returns were only favoured by longshore currents that originated either from obliquely incident waves or the tide. The high exit rate of drifters without longshore currents is attributed to the rather steep beach slope at the offshore side of the bar. Therefore, the surf zone edge was very close to the bar crest. As a consequence, drifters that floated offshore in the rip channel had left the surf zone just after they had passed the bar head. Outside the surf zone the drifters were not subjected to a strong onshore mass flux and did not return shoreward.

Once the drifters had exited the rip channel, the tidal current caused the drifters to be deflected in alongshore direction. This limited the offshore extent of the rip current and the drifters remained closer to the breaker line where they are subject to a stronger Stokes drift. The onshore mass transport associated with the Stokes drift caused drifters to return shoreward and favoured drifter retention in the surf zone. In contrast, in the absence of tidal

currents, drifters floated further offshore. Relatively low water levels coincide with small tidal velocities around low water slack which occurs approximately 2 hours after low tide (Figure 7.21, black vertical lines). This may explain why the lifeguards report most rip activity just after low water (with the upcoming tide).

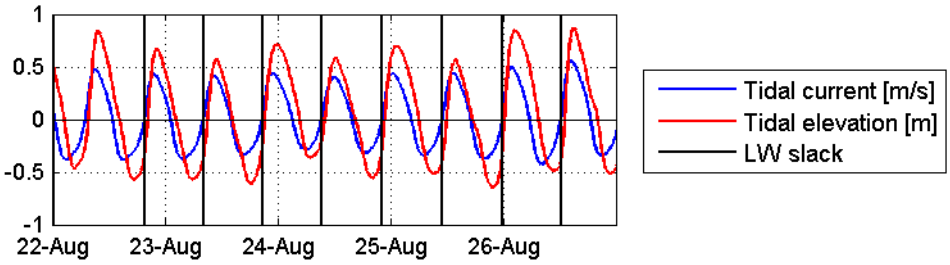

Figure 7.21 Tidal current and Tidal water level. The vertical black lines indicate low tide slack water when the tidal current is zero and the water level is relatively low.

7.5 Conclusions

The governing parameters in the generation of rip currents at Egmond aan Zee have been identified. The most prominent are:

- the wave height;
- the water depth over the bar (dependent on the crest height of the updrift bar and the water level); and
- the rip channel depth (with respect to the bar crest).

These three parameters together determine the wave dissipation gradient from the bar to the rip channel.

The rip strength depends positively on the wave period, but its impact is less strong than the effect of the wave height and water level.

The wave angle does not influence the strength of the cross-shore velocity for typical rip channel widths at Egmond aan Zee, which is consistent with field observations at Egmond. Only in narrow rip channels does a large wave angle have a negative impact on the rip strength. Likewise, the wave angle may have a negative impact for larger wave heights that generate stronger longshore currents and may possess enough inertia to bypass the channel. This was not tested in the present study.

The extent of the rip current is limited by the tide. At low water slack, zero tidal velocities coincide with relatively low water so that relatively strong rip currents may be created that extend far offshore. This may have implications for swimmer safety and indicates that the most dangerous conditions develop around low water slack and not with the lowest water levels.

Vertical bed irregularities in the order of 0.5 m and smaller with little spatial extent (so that they do not represent a rip channel) do not affect the flow pattern and strength and therefore, knowledge about them is not required to model rip current flow accurately.

7.6 Validation of a rip strength model with field data

The sensitivity analysis identified three parameters that govern rip current strength: wave height, water depth over the updrift bar and rip channel depth (w.r.t. to the bar height). The proposed parameters were combined in a parametric model that is presented in Figure 7.22. This model is a modification of the conceptual coastal engineering rip current model by *de Zeeuw* [2011] that suggested an increase in rip activity for increasing H_{m0} / d and increasing vertical bottom variations, but a decrease in rip activity with increasing longshore currents.

The variables in the proposed model were quantified from the data obtained during the sensitivity analysis. Furthermore, longshore currents were excluded from the input because a dependency could not be established in the field or in the model for site typical channel dimensions. However, longshore currents may have a significant impact when their flow velocities are larger due to larger wave heights or when the rip channels are narrower. The impact of large obliquely incident waves was not addressed in this study.

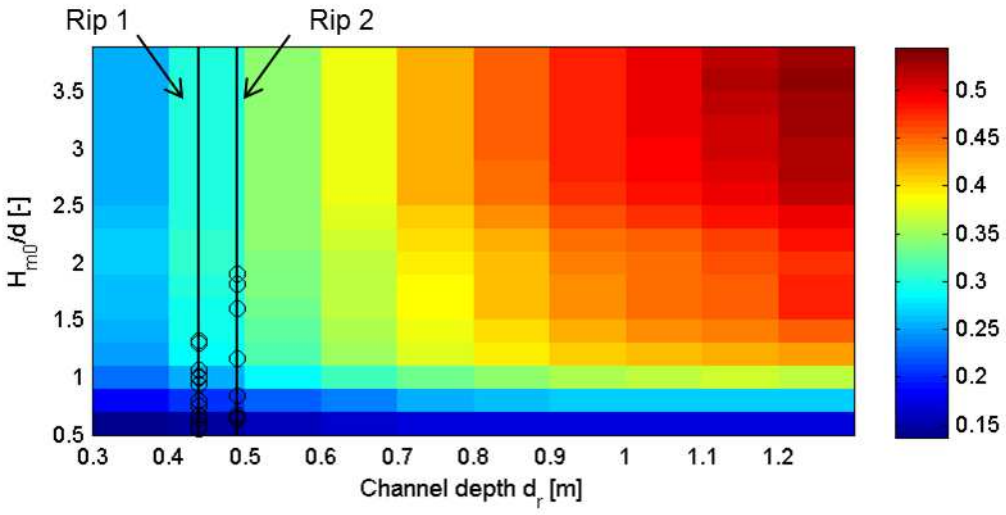

Figure 7.22 Parametric model for the rip current strength with the Channel depth d_r on the x-axis and the ratio wave height over water depth on the updrift bar on the y-axis. The colors indicate the rip strength in m/s and the black circles in the lower left corner mark the conditions during the field observations.

The model was validated against field data measured in Rip 1 (d_r = 0.44 m) and Rip 2 (d_r = 0.49 m). The results of the sensitivity analysis were interpolated on the channel depths of Rip 1 and 2 (Figure 7.22, black lines) and were compared to field data from both rips (Figure 7.23).

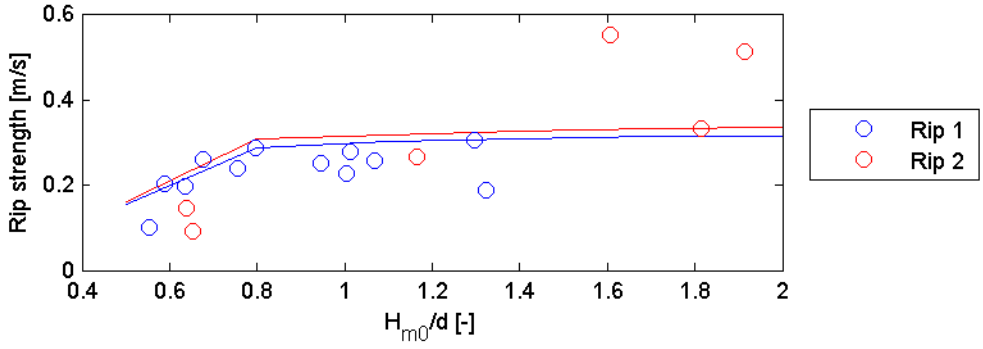

Figure 7.23 Validation of the results from the sensitivity analysis against field data

The data from Rip 1 is in good agreement with the results of the sensitivity analysis. That implies that most of the variance in the field data can indeed be explained by those three parameters. However, the data from Rip 2 agrees less with the results of the sensitivity analysis and the deviation is mostly attributed to the large velocities measured on August 25. This suggests that the values from the August 25 deployments are indeed caused by processes that are not addressed in this study (e.g. wind-driven currents, fluctuations of the rip current). The upper limit to the rip strength proposed in the present model is valid for stationary conditions and does not exclude the possibility that rip currents may be stronger temporarily due to velocity fluctuations in the infragravity or very low frequency band (see also Section 2.4).

It is acknowledged that the available field data only suffices to validate a small part of the proposed rip strength model and more field experiments with different forcing and beach configuration are required to verify this model.

8 Conclusions and Recommendations

8.1 *Introduction*

This study investigated the mean flow characteristics of rip currents at Egmond aan Zee and the prominent parameters that drive these currents. The applicability of the numerical model XBeach for this study was assessed in a hindcast of a laboratory rip current experiment. The same model was applied for field scale rip currents and the results were in line with observations described in literature. A field study was undertaken with drifter instruments and human drifters that were tracked via GPS to measure rip currents in the field and to correlate their behaviour to outside forcing. The hindcast of the experiment in XBeach was in good agreement with the field data and justified the use of this model in a sensitivity study. Along with the field data the results of the sensitivity analysis were used to identify the governing parameters of rip currents at Egmond aan Zee and to describe their particularities compared to rip currents in other environments.

8.2 *Conclusions*

Field Observations

An extensive dataset of rip current measurements in a Lagrangian framework was collected. In total, 28 drifter deployments were performed and 21 of these observations were classified as rip events. Three flow patterns were observed:

1. A local one-sided circulation cell that was observed with rather weak rip current flow.
2. A strong offshore movement of the drifters that were then advected by a longshore current offshore of the bar (observed with rather strong rips).
3. A meandering longshore current that prevailed with high water levels.

Offshore directed drifter velocities were on average 0.18 m/s in flow pattern 1 and 0.31 m/s in flow pattern 2. The maximum offshore directed velocities of 0.60 m/s were measured on August 26 when also the highest offshore wave heights were recorded. The wave height H_{m0} was as large as 0.7 m and the offshore wave period T_{m02} was 3.6 s. However, these large drifter velocities were presumably supported by a cross-offshore wind.

In contrast to previous field observations the surf zone exit rate of the drifters was high. This was attributed to the fact that the rip neck was not confined to the surf zone during the field experiments and that drifters got advected by the tidal longshore current offshore of the rip channel.

Onshore of the rip channel the drifter measurements indicated the existence of a second circulation cell that may have caused the embayment onshore of the rip channels. In case of a meandering longshore current the drifters were observed to slow down onshore of the rip neck. This may be due to the lack of wave breaking in the channel so that the wave forcing in longshore direction that drives the longshore current is absent.

The drifters behaved consistently during the deployments and did not deviate notably from a mean trajectory. Along with the observation that drifters followed the same trajectory when they were deployed at the same location at an interval of one minute, this led to the conclusion that the rip is stationary for a period in the order of a few minutes.

A statistically significant correlation between the measured rip current strength and the ratio of offshore wave height over water depth on the updrift bar H_{m0} / d was identified. Video

images indicate that this relation is not linear but stagnates for large values of H_{m0} / d when wave breaking commences in the rip channel. No statistically significant relationship was determined between the wave period and the rip strength or the wave angle and the rip strength.

Capability and limitations of XBeach in rip current modelling

The 2D hydrostatic XBeach model was used in stationary mode (no wave groups) to hindcast a laboratory experiment [*Haller et al.*, 2002] and the field measurements presented in this study. The time averaged behaviour of rip currents was replicated well while the simplicity of the model allowed for relatively short run times and thus the model is suited for an operational forecast model.

Based on the hindcast of the laboratory experiment and the field measurements at Egmond aan Zee presented in this study the following model properties were found to play a key role in the numerical simulation of rip currents:

- The stationary wave driver efficiently and accurately reproduced the rip current velocities within the rip neck observed in the field and measured in the laboratory.
- Wave current interaction is crucial to accurately simulate the shoaling and refraction of the incoming waves due to an opposing rip current.
- In combination with wave-current interaction the directional resolution must be sufficiently high to capture wave refraction towards the rip channel. A resolution of $d\theta = 20^\circ$ was determined to be sufficient in this study.
- The dynamic behaviour of laboratory scale rip currents is very sensitive to the viscosity that is induced by the turbulence of the roller. In field scale and with stationary boundary conditions (no wave groups) the rip current is not affected by an increase in viscosity.
- The cross-shore resolution must be sufficiently high ($\Delta x = 5$ m) in the nearshore zone to resolve the flow in the feeder channel and to depict the dimensions of the large scale rip bathymetry features with sufficient accuracy.
- The tidal longshore current may not be neglected as it has an important impact on the flow behaviour offshore of the rip channel and on the flow in the feeder channel.
- The offshore extent of the rip current is underestimated because the 2DH XBeach model lacks information about the specific vertical flow structure offshore of the rip channel.

Sensitivity of the rip current to hydrodynamic and geometric parameters

The governing parameters in the generation of rip currents at Egmond aan Zee have been identified. The most prominent are:

- the wave height;
- the water depth over the bar (dependent on the crest height of the updrift bar and the water level); and
- the rip channel depth (with respect to the crest height of the updrift bar).

These three parameters together determine the wave dissipation gradient from the bar to the rip channel and determine the strength of the offshore directed velocities.

The rip strength depends positively on the wave period, but its impact is less strong than the effect of wave height and water level.

The wave angle does not influence the strength of the cross-shore velocity for typical rip channel widths and wave heights at Egmond aan Zee. Only in narrow rip channels does a large wave angle have a negative impact on the rip strength. Likewise, the wave angle may have a negative impact in combination with larger wave heights that generate stronger longshore currents with enough inertia to bypass the channel. Large waves were not tested in the context of obliquely incident waves.

The extent of the rip current is limited by the tide. At low water slack, zero tidal velocities coincide with relatively low water so that rip currents extend far offshore.

Small scale vertical bed irregularities in the order of 0.5 m and smaller that do not represent a rip channel do not affect the flow pattern and rip current strength and therefore, knowledge about them is not required to model rip current flow accurately. This allows building forecast models based on bathymetries with less spatial resolution given that the main geometric features of the rip current system (bar height, channel depth, channel width and feeder channel) are available.

Rip strength model

Based on the results of the sensitivity analysis the conceptual coastal engineering rip current model by *de Zeeuw* [2011] was modified and the parameters in the model were quantified. The modified model allows estimating the rip strength based on wave height, water depth over the bar and rip channel depth. The results of this model agreed well with the field data apart from the high velocities measured on August 25 A when the drifter velocities were believed to be enhanced by a cross-offshore wind.

This simple tool could assist lifeguards to estimate typical rip current velocities based on wave and tide forecasts and given that information about bar height and channel depth are at their disposal. To use the tool further as a rip current hazard indicator the rip current velocities estimated from the model need to be translated into hazard levels based on typical swimmer capabilities (see Section 2.4).

8.3 Recommendations

Field data

In the present field experiment the beach configuration was characterised by unusually shallow rip channels for the end of summer which may be attributed to a beach nourishment that was conducted prior to the campaign or to a stormy early summer. Field data from a more typical beach configuration is needed to verify the findings of the present experiment.

Rip current oscillations

The objective of the present study was to investigate the mean flow properties of rip currents at Egmond aan Zee while their temporal behaviour was addressed only insufficiently. But rip current velocity may be greatly altered by infragravity and very low frequency motions that are induced by wave group interactions (see Section 2.4). Another field campaign is recommended to measure continuous time series of rip currents with in situ current meters. This will offer valuable information about the existence and importance of these fluctuations.

Wind-driven currents

Cross-offshore winds were believed to have contributed to the maximum measured drifter velocities. However, wind-driven currents were not subject of the present study and their influence on rip currents remains unclear. Drifter instruments and swimmers both float in the

upper water layer so that wind-driven surface currents may have a significant impact on drift velocities. It is suggested to conduct drifter measurements also in the absence of waves to investigate the impact of wind-driven currents on drifter velocities.

Statistical and Probabilistic Analysis

The sensitivity analysis in this study treated parameters separately. A larger set of field and numerical data would enable the use of a principal component analysis (PCA) to identify the relative importance of the influencing parameters. A PCA provides a more comprehensive picture of rip current governing parameters because it can be used to interpret data related to inter-dependent variables. Furthermore, a larger data set (both field and numerical data) allows the construction of a Bayesian Model that can be used to predict rip currents associated with an occurrence probability.

Laboratory tests

The influence of the wave angle on rip currents has not received much attention to date. Their exploration in the field is difficult due to other factors that influence rip currents in the field such as wave height, wind and tide. The impact of wave angles on rip currents has been investigated mainly numerically and only insufficiently in the laboratory. Although a laboratory study is costly and physical modelling of longshore currents is difficult due to the lateral boundaries of the wave tank, it is suggested that a physical experiment would add valuable knowledge about the effect of various wave angles. A physical experiment would allow to distinguish between the regime (channel width and wave height) where wave angles have an impact and the regime where they do not have an impact on rip currents.

XBeach development

A necessity was identified to improve the wave dissipation formulation in the presence of an opposing current. A spatially varying formulation for γ is suggested that is calibrated against wave data in a rip current. Furthermore, for accurate drifter simulations the vertical structure of the flow field needs to be accounted for in order to model the flow behaviour offshore of the channel. Likewise, wind-driven currents also vary greatly with depth. Thus, the wind stress formulation in combination with the drifter option in XBeach needs to be validated against drifter velocities to hindcast field measurements more accurately and to include wind-driven currents in forecast models.

Rip current forecast models

A model was proposed to determine the rip strength from the prominent parameters (wave height, water level and channel depth). However, the model could be validated only against a data set collected in a small range of conditions. To verify this model more field data obtained under a large range of conditions is required. Furthermore, it is recommended to extend this model with processes that were not addressed in the sensitivity analysis (e.g. rip current oscillations and wind-driven currents).

References

Aagaard, T., B. Greenwood, and J. Nielsen (1997), Mean currents and sediment transport in a rip channel, *Marine Geology*, *140*(1-2), 25-45.

Austin, M., T. M. Scott, J. W. Brown, J. A. Brown, J. H. MacMahan, G. Masselink, and P. Russell (2010), Temporal observations of rip current circulation on a macro-tidal beach, *Continental Shelf Research*, *30*(1149-1165).

Baldock, T. E., P. Holmes, S. Bunker, and P. Van Weert (1998), Cross-shore hydrodynamics within an unsaturated surf zone, *Coastal Engineering*, *34*(Compendex), 173-196.

Battjes, J. A. (1988), Surf-Zone Dynamics, *Annual Review of Fluid Mechanics*, *20*, 257-293.

Battjes, J. A., and M. J. F. Stive (1985), Calibration and Verification of a Dissipation Model for Random Breaking Waves, *Journal of Geophysical Research*, *90*(C5), 9159-9167.

Bowen, A. (1969), Rip Currents 1. Theoretical Investigations *J. Geophys. Res.*, *74*(23), 5467-5478.

Brander, R. W. (1999), Field observations on the morphodynamic evolution of a low-energy rip current system, *Marine Geology*, *157*(3-4), 199-217.

Brander, R. W., and A. D. Short (2000), Morphodynamics of a large-scale rip current system at Muriwai Beach, New Zealand, *Marine Geology*, *165*(Compendex), 27-39.

Brander, R. W., and J. H. MacMahan (2011), Future Challenges for Rip Current Research and Outreach, in *Rip Currents: Beach Safety, Physical Oceanography and Wave Modeling*, edited by S. Leatherman and J. Fletemeyer, CRC Press, Boca Raton, FL.

Bruneau, N., B. Castelle, P. Bonneton, R. Pedreros, R. Almar, N. Bonneton, P. Bretel, J.-P. Parisot, and N. Sénéchal (2009), Field observations of an evolving rip current on a meso-macrotidal well-developed inner bar and rip morphology, *Continental Shelf Research*, *29*(14), 1650-1662.

Callaghan, D. P., T. E. Baldock, and P. Nielsen (2004), Pulsing and Circulation in Rip Current System, in *International Conference Coastal Engineering*, edited by J. M. Smith, pp. 1493-1505, American Society of Civil Engineers, Lisbon.

Chen, Q., R. A. Dalrymple, J. T. Kirby, A. B. Kennedy, and M. C. Haller (1999), Boussinesq modeling of a rip current system, *J. Geophys. Res.*, *104*(C9), 20617-20637.

Cleveland, W. S. (1979), Robust Locally Weighted Regression and Smoothing Scatterplots, *Journal of the American Statistical Association*, *74*(368), 829-836.

Dalrymple, R. A. (1978), Rip currents and their causes, in *International Conference on Coastal Engineering*, edited, pp. 1414-1427, American Society of Civil Engineers, Hamburg.

Dalrymple, R. A., J. H. MacMahan, A. J. H. M. Reniers, and V. Nelko (2011), Rip Currents, *Annual Review of Fluid Mechanics*, *43*(1), 551-581.

Daly, C. (2009), Low Frequency Waves in the Shoaling and Nearshore Zone, Delft University of Technology.

De Zeeuw, R. C. (2011), Nearshore currents and swimmer safety in the Netherlands, Delft University of Technology, Delft.

Dette, H. H., K. Peters, and F. Spignat (1995), About rip currents at a meso-tidal coast, in *Coastal Dynamics '95*, edited, pp. 477-488, American Society of Civil Engineers, Gdansk, Poland.

Engle, J. A. (2003), Formulation of a rip current forecasting technique through statistical analysis of rip current-related rescues, University of Florida.

ERB (2010), Egmondse Reddingsbrigade, Jaarverslag 2010, edited.

Gallagher, E. L., J. MacMahan, A. J. H. M. Reniers, J. Brown, and E. B. Thornton (2011), Grain size variability on a rip-channeled beach, *Marine Geology*, *287*(Compendex), 43-53.

Haas, K. A. (2012), Low-pass filtered time series of the cross-shore velocity in a laboratory scale rip current, 09/02/2012 *pers. comm.*

Haas, K. A., and I. A. Svendsen (2002), Laboratory measurements of the vertical structure of rip currents, *J. Geophys. Res.*, *107*(C5), 3047.

Haas, K. A., I. A. Svendsen, M. C. Haller, and Q. Zhao (2003), Quasi-three-dimensional modeling of rip current systems, *J. Geophys. Res.*, *108*(C7), 3217.

Haller, M. C., and R. A. Dalrymple (2001), Rip current instabilities, *Journal of Fluid Mechanics*, *433*, 161-192.

Haller, M. C., R. A. Dalrymple, and I. A. Svendsen (2000), Experiments on rip currents and nearshore circulation: data report, *Res. Rep. CACR-00-04*, Center for Applied Coastal Research, University of Delaware, Newark.

Haller, M. C., R. A. Dalrymple, and I. A. Svendsen (2002), Experimental study of nearshore dynamics on a barred beach with rip channels, *J. Geophys. Res.*, *107*(C6), 3061.

Holthuijsen, L. (2007), *Waves in Oceanic and Coastal Waters*, Cambridge University Press Cambridge.

Jacobs, R. P. M. (2010), Non-Hydrostatic Computations of Nearshore Hydrodynamics, Delft University of Technology, Delft.

Johnson, D., and C. Pattiaratchi (2004), Transient rip currents and nearshore circulation on a swell-dominated beach, *J. Geophys. Res.*, *109*(C2), C02026.

Kumar, N., G. Voulgaris, and J. C. Warner (2011), Implementation and modification of a three-dimensional radiation stress formulation for surf zone and rip-current applications, *Coastal Engineering*, *58*(12), 1097-1117.

Lascody, R. L. (1998), East central Florida rip current programme, *Natl. Weather Dig.*, *22*(2), 25-30.

Longuet-Higgins, M. S., and R. w. Stewart (1964), Radiation stresses in water waves; a physical discussion, with applications, *Deep Sea Research and Oceanographic Abstracts*, *11*(4), 529-562.

Lushine, J. B. (1991), A study of rip current drownings and related weather factors, *Natl. Weather Dig.*, *16*(3), 13-19.

MacMahan, J. H. (2001), Hydrographic surveying from a personal watercraft, *Journal of Surveying Engineering*, *127*(1).

MacMahan, J. H., E. B. Thornton, and A. J. H. M. Reniers (2006), Rip current review, *Coastal Engineering*, *53*(2–3), 191-208.

MacMahan, J. H., J. Brown, and E. Thornton (2009), Low-Cost Handheld Global Positioning System for Measuring Surf-Zone Currents, *Journal of Coastal Research*, 744-754.

MacMahan, J. H., A. J. H. M. Reniers, E. B. Thornton, and T. P. Stanton (2004), Surf zone eddies coupled with rip current morphology, *J. Geophys. Res.*, *109*(C7), C07004.

MacMahan, J. H., E. B. Thornton, T. P. Stanton, and A. J. H. M. Reniers (2005), RIPEX: Observations of a rip current system, *Marine Geology*, *218*(Compendex), 113-134.

MacMahan, J. H., E. B. Thornton, A. J. H. M. Reniers, T. P. Stanton, and G. Symonds (2008), Low-Energy Rip Currents Associated With Small Bathymetric Variations, *Marine Geology*, *255*(3-4), 156-164.

MacMahan, J. H., et al. (2010), Mean Lagrangian flow behavior on an open coast rip-channeled beach: A new perspective, *Marine Geology*, *268*(1-4), 1-15.

Nelko, V., and R. A. Dalrymple (2008), Rip Currents: Mechanisms and Observations, in *Coastal Engineering 2008 - 31st International Conference on Coastal Engineering, 31 August to 5 September 2008*, edited by H. S. Rainer Lehfeldt, American Society of Civil Engineers, Hamburg.

NOAA (2011), http://www.ripcurrents.noaa.gov/, 17.12.2011.

Ranasinghe, R., G. Symonds, K. Black, and R. Holman (2004), Morphodynamics of intermediate beaches: A video imaging and numerical modelling study, *Coastal Engineering*, *51*(Compendex), 629-655.

Reintjes, C. M. (2002), IMAU Report R 02-02 Muilocaties voor de kust bij Egmond aan Zee*Rep.*, Universiteit Utrecht; Rijkswaterstaat.

Reniers, A. J. H. M., J. A. Roelvink, and E. B. Thornton (2004), Morphodynamic modeling of an embayed beach under wave group forcing, *J. Geophys. Res.*, *109*(C1), C01030.

Reniers, A. J. H. M., J. H. MacMahan, E. B. Thornton, T. P. Stanton, M. Henriquez, J. W. Brown, J. A. Brown, and E. Gallagher (2009), Surf zone surface retention on a rip-channeled beach, *J. Geophys. Res.*, *114*(C10), C10010.

Rijkswaterstaat (2011), Zandsuppleties kust Bergen aan Zee en Egmond aan Zee, edited.

Roelvink, D., A. Reniers, A. van Dongeren, J. van Thiel de Vries, R. McCall, and J. Lescinski (2009), Modelling storm impacts on beaches, dunes and barrier islands, *Coastal Engineering*, *56*(11-12), 1133-1152.

Roelvink, J. A. (1993), Surf beat and its effect on cross-shore profiles, TU Delft.

Ruessink, B. G., D. J. R. Walstra, and H. N. Southgate (2003), Calibration and verification of a parametric wave model on barred beaches, *Coastal Engineering*, *48*, 139-149.

Schmidt, W. E., B. T. Woodward, K. S. Millikan, R. T. Guza, B. Raubenheimer, and S. Elgar (2003), A GPS-tracked surf zone drifter, *Journal of Atmospheric and Oceanic Technology*, *20*(Compendex), 1069-1075.

Shepard, F. P., K. O. Emery, and E. C. L. Fond (1941), Rip Currents: A Process of Geological Importance, *The Journal of Geology*, *49*(4), 337-369.

Short, A. D. (1992), Beach systems of the central Netherlands coast: Processes, morphology and structural impacts in a storm driven multi-bar system, *Marine Geology*, *107*(1-2), 103-132.

Smit, M. W. J., A. J. H. M. Reniers, B. G. Ruessink, and J. A. Roelvink (2008), The morphological response of a nearshore double sandbar system to constant wave forcing, *Coastal Engineering*, *55*(10), 761-770.

Sonu, C. J. (1972), Field Observation of Nearshore Circulation and Meandering Currents, *J. Geophys. Res.*, *77*(18), 3232-3247.

Svendsen, I. A., K. A. Haas, and Q. Zhao (2000), Analysis of Rip Current Systems, in *29th International Conference on Coastal Engineering*, edited by B. L. Edge, pp. 1127-1140, American Society of Civil Engineers, Sydney.

Van Dongeren, A., A. Reniers, J. Battjes, and I. Svendsen (2003), Numerical modeling of infragravity wave response during DELILAH, *J. Geophys. Res.*, *108*(C9), 3288.

van Dongeren, A., N. Plant, A. Cohen, D. Roelvink, M. C. Haller, and P. Catalán (2008), Beach Wizard: Nearshore bathymetry estimation through assimilation of model computations and remote observations, *Coastal Engineering*, *55*(12), 1016-1027.

van Duin, M. J. P., N. R. Wiersma, D. J. R. Walstra, L. C. van Rijn, and M. J. F. Stive (2004), Nourishing the shoreface: observations and hindcasting of the Egmond case, The Netherlands, *Coastal Engineering*, *51*(8-9), 813-837.

van Enckevort, I. M. J., B. G. Ruessink, G. Coco, K. Suzuki, I. L. Turner, N. G. Plant, and R. A. Holman (2004), Observations of nearshore crescentic sandbars, *J. Geophys. Res.*, *109*(C6), C06028.

Voulgaris, G., N. Kumar, and J. C. Warner (2011), Methodology for Prediction of Rip Currents Using a Three-Dimensional Numerical, Coupled, Wave Current Model, in *Rip Currents: Beach Safety, Physical Oceanography and Wave Modeling*, edited by S. Leatherman and J. Fletemeyer, CRC Press, Boca Raton, FL.

Willmott, C. J., S. G. Ackleson, R. E. Davis, J. J. Feddema, K. M. Klink, D. R. Legates, J. O'Donnell, and C. M. Rowe (1985), Statistics for the Evaluation and Comparison of Models, *Journal of Geophysical Research*, *90*(C5), 8995-9005.

Wright, L. D., S. K. May, A. D. Short, and M. O. Green (1984), Beach and Surf Zone Equilibria and Response Times, in *Coastal Engineering 1984 - 19th International Conference on Coastal Engineering, 3 to 7 September 1984*, edited by B. L. Edge, pp. 2150-2164, American Society of Civil Engineers, Houston, Texas.

Appendix

A. The Roelvink wave dissipation formulation in an opposing current

For in-stationary waves the wave dissipation in XBeach is calculated according to the Roelvink breaker formulation [*Roelvink*, 1993]. The wave dissipation rate per unit area D_w is given by:

$$D_w = 2\alpha f_{rep} Q_b E_w \tag{1.1}$$

with α in the order of 1, f_{rep} a representative intrinsic frequency and E_w the total wave energy integrated over all directional bins. The probability of a wave to break in an irregular wave field is estimated by:

$$Q_b = 1 - \exp\left(-\left(\frac{H}{\gamma h}\right)^n\right) \tag{1.2}$$

with the wave breaking parameter γ and an exponent n. Default values for γ and n are 0.55 and 10 respectively. To account for the effect of an opposing current γ is scaled with a term dependent on the local water depth h and the wave number k as follows:

$$\gamma = \gamma_0 \frac{\tanh(kh)}{kh} \tag{1.3}$$

This implies that γ reduces with increasing wave number k or increasing water depth h, respectively. In the presence of an opposing current the wave number k increases due to current-induced shoaling and therefore, γ decreases. Likewise, γ decreases with increasing water depth. It is noted, that the effect of an opposing current on the wave breaking parameter γ is opposite in the empirical formulation by *Ruessink et al.* [2003] that is used for stationary waves. This implies that wave breaking commences in deeper water in the presence of an opposing current for two reasons: (1) Due to current induced shoaling the wave reaches its breaking height in deeper water already and (2) the wave breaking parameter γ is smaller in the presence of an opposing current. A small γ is usually associated with spilling breakers and the breaking process in spilling breakers is less intense. However, Haller et al. [2002] propose that a rip current will shift the breaking more towards the plunging regime. This hypothesis is supported by their observations in the wave tank of more intense wave breaking and higher H/h ratios in the presence of a strong rip. But present wave breaking formulations do not readily account for the type of wave breaking. In the Roelvink formulation the probability of wave breaking can be tuned by the exponent n. The formulation was calibrated best against a large set of lab data with $n = 10$. A larger n will constrict wave breaking to a narrower range of γ so that wave breaking commences later and takes place over a narrower cross-shore stretch. In fact, the wave breaking manner is then shifted more towards a plunging regime (Figure A.1).

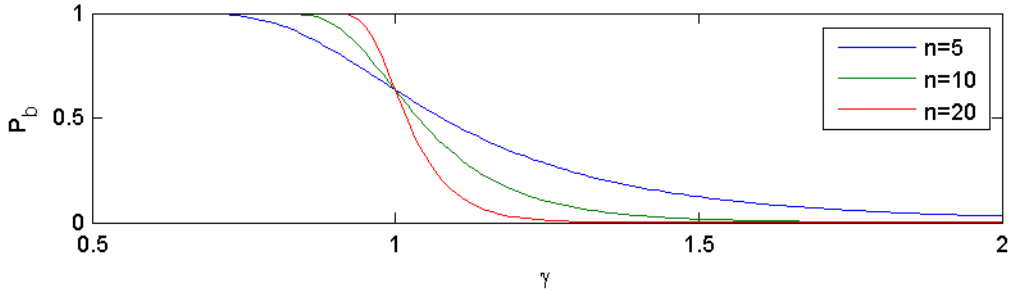

Figure A.1 Probability Q_b for a wave to break vs. wave breaking parameter γ with n=5, n=10, n=20.

The Roelvink wave dissipation formulation was applied to the laboratory experiment (presented in Section 3.3) to test it with $\gamma_0 = 0.55$ and 0.7 and $n = 10$. The cross-shore wave height evolutions in the channel and over the bar for those two simulations are depicted in Figure A.2.

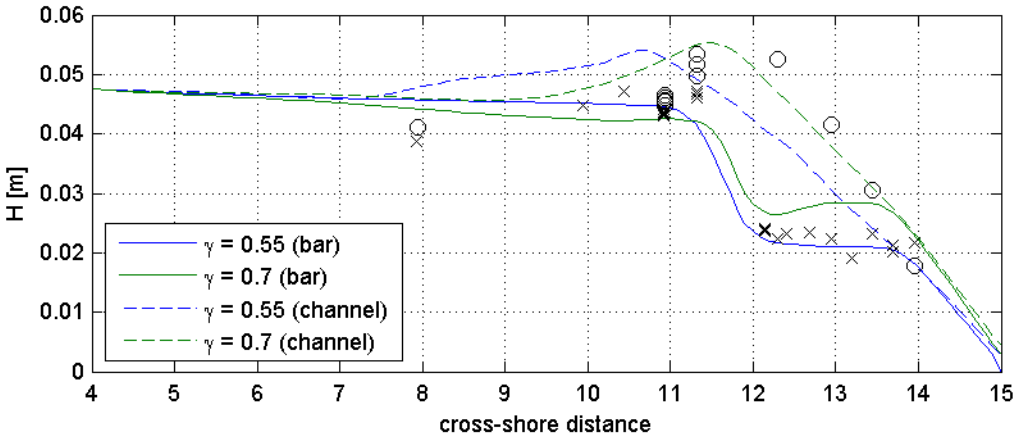

Figure A.2 Cross-shore transect of modelled wave height with wave current interaction (blue) and without (green) over the bar (solid line) and in the rip channel (dashed line) and the experimental data over the bar (crosses) and in the rip channel (circles).

The default value $\gamma_0 = 0.55$ agreed very well with the measured wave heights in the bar transect, but performed less well in the channel transect where a better agreement with the measured values was achieved with $\gamma_0 = 0.8$. These results suggest that the wave breaking parameter γ should be increased in an opposing current and not reduced as it is done at present. Further research on the wave dissipation formulation according to *Roelvink* [1993] in the presence of an opposing current is required.

B. Record of the field experiment

B.1. Hydrodynamic conditions and calculated rip strength per deployment

Table B.1 Overview of the hydroynamic conditions and rip current observations during the field experiments: Date, deployment number (Dpl.), measurement location (North = Rip1, South = Rip 2), Start and end time of the deployment, tidal water elevation (WL), Tidal current (Tide), offshore wave height (H_{m0}), offshore wave period (T_{m02}), offshore wave angle (T_{h0}), offshore directional spreading (s_0), offshore wave height over water depth on the updrift bar (H_{m0}/d), wind speed (WIND), wind direction (DIR), calculated rip strength, Nr. Of logged drifters (Nr drifters) and observed flow pattern.

Date	Dpl.	Rip	Start	End	WL	Tide	H_{m0}	T_{m02}	T_{h0}	s_0	H_{m0}/d	WIND	DIR	Rip strength	Nr drifters	Flow pattern
					[m NAP]	[m/s]	[m]	[s]	[°N]	[°]	[1/s]	[m/s]	[°N]	[m/s]	[-]	type
22.08.2011	1	North	15:23	15:44	-0.32	-0.38	0.50	3.1	287	44	0.80	6	360	0.288	8	2
22.08.2011	2	North	15:51	16:20	-0.46	-0.36	0.53	3.2	287	42	1.07	6	360	0.259	9	1
22.08.2011	3	North	16:27	16:49	-0.53	-0.35	0.55	3.3	287	39	1.30	6	10	0.306	9	2
22.08.2011	4	North	17:02	17:47	-0.57	-0.30	0.51	3.4	289	40	1.32	5	20	0.189	15	1
23.08.2011	1	North	15:57	16:15	-0.30	-0.34	0.38	3.7	326	50	0.59	2	30	0.204	7	1
23.08.2011	2	North	16:30	16:58	-0.45	-0.35	0.38	3.5	327	51	0.75	2	10	0.240	8	2
23.08.2011	3	North	17:09	17:33	-0.55	-0.34	0.38	3.7	316	51	0.95	2	270	0.251	9	2
23.08.2011	4	North	17:44	18:06	-0.60	-0.32	0.35	3.7	318	50	1.01	2	270	0.280	9	2
23.08.2011	5	North	18:07	18:43	-0.61	-0.30	0.35	3.8	312	54	1.00	6	240	0.227	9	2
24.08.2011	1	North	16:15	16:41	0.00	-0.20	0.53	3.7	294	43	0.56	6	240	0.100	9	1
24.08.2011	2	North	16:50	17:08	-0.09	-0.27	0.55	3.6	292	41	0.64	6	240	0.197	12	1
24.08.2011	3	North	17:15	17:31	-0.17	-0.31	0.53	3.6	292	42	0.88	6	240	0.262	3	2
24.08.2011	4	North	17:40	18:04	-0.28	-0.34	0.54	3.5	285	41	0.81	6	240	0.208	6	1
24.08.2011	5	North	18:14	18:39	-0.40	-0.35	0.51	3.4	285	43	0.93	6	230	0.252	9	1
25.08.2011 A	1	South	10:00	10:14	-0.49	-0.17	0.70	3.6	224	32	1.91	4	140	0.513	3	2
25.08.2011 A	2	South	10:18	10:33	-0.47	-0.12	0.70	3.6	224	32	1.81	4	140	0.333	2	2
25.08.2011 A	3	South	10:37	10:47	-0.44	-0.08	0.67	3.6	228	31	1.61	4	140	0.554	3	2
25.08.2011 A	4	South	10:54	11:26	-0.33	0.05	0.62	3.5	230	31	1.17	4	140	0.268	3	3
25.08.2011 A	5	South	11:21	11:48	-0.17	0.17	0.58	3.4	233	32	0.84	6	140	0.000	0	3
25.08.2011 B	1	South	17:30	17:51	-0.03	-0.18	0.56	3.0	231	35	0.67	3	250	0.000	0	3
25.08.2011 B	2	South	17:59	18:24	-0.08	-0.28	0.51	3.2	230	39	0.65	3	250	0.093	6	1
25.08.2011 B	3	South	18:31	19:07	-0.20	-0.35	0.43	3.3	235	39	0.64	1	120	0.145	10	1
25.08.2011 B	4	North	19:27	19:51	-0.41	-0.38	0.39	3.4	249	37	0.96	1	100	0.150	13	1 / 2
26.08.2011	1	South	11:00	11:21	-0.48	-0.19	0.38	2.5	150	52	1.01	7	160	0.154	7	1 / 2 / 3
26.08.2011	2	South	11:10	11:21	-0.48	-0.18	0.38	2.5	150	52	1.00	7	160	0.109	2	-
26.08.2011	3	South	11:30	11:52	-0.46	-0.11	0.38	2.5	163	49	0.95	7	160	0.203	9	2
26.08.2011	4	South	12:11	12:34	-0.33	0.08	0.36	2.5	174	56	0.68	0	220	0.221	8	2
26.08.2011	5	North	12:46	13:05	-0.07	0.27	0.47	2.4	185	46	0.64	0	220	0.000	0	3

B.2. Measured drifter trajectories

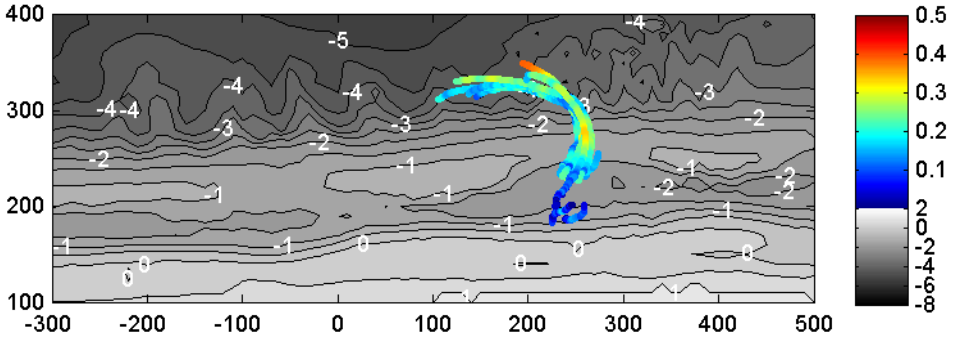

Figure B.1 Drifter trajectories measured on August 22 during dpl.1.

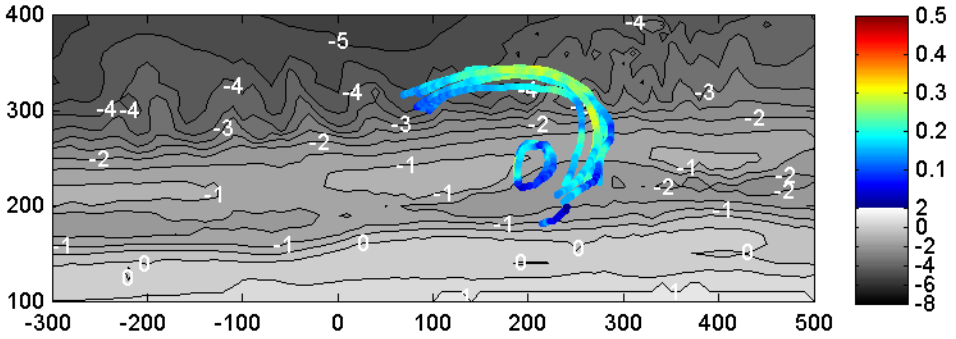

Figure B.2 Drifter trajectories measured on August 22 during dpl.2.

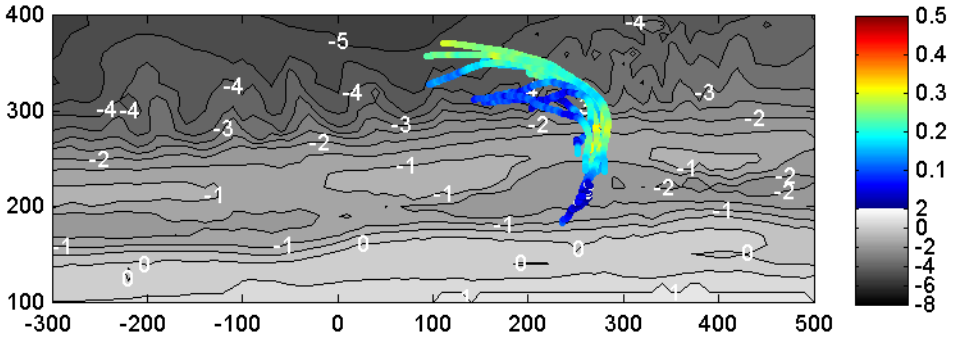

Figure B.3 Drifter trajectories measured on August 22 during dpl.3.

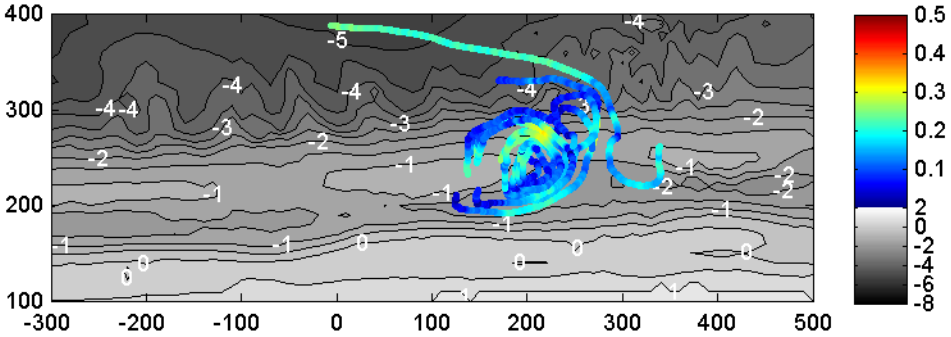

Figure B.4 Drifter trajectories measured on August 22 during dpl.4.

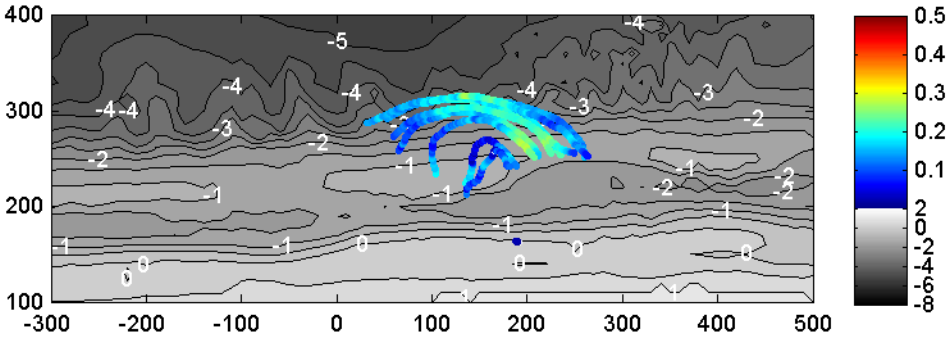

Figure B.5 Drifter trajectories measured on August 23 during dpl.1.

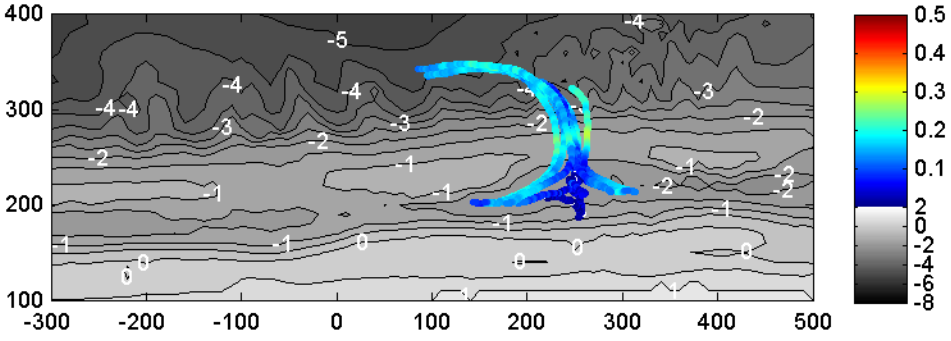

Figure B.6 Drifter trajectories measured on August 23 during dpl.2

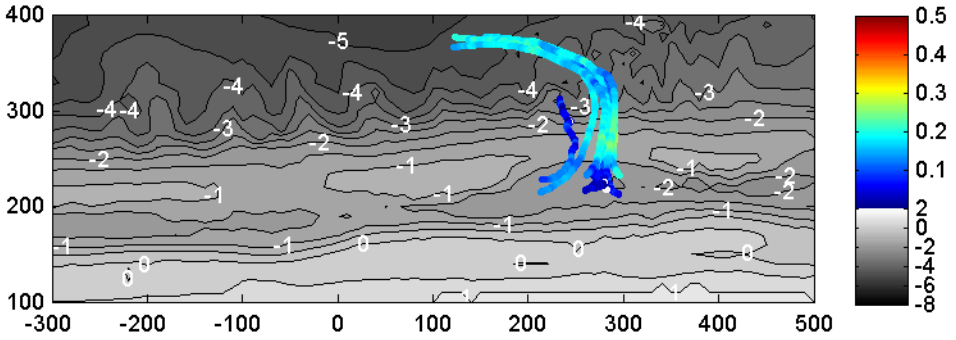

Figure B.7 Drifter trajectories measured on August 23 during dpl.3.

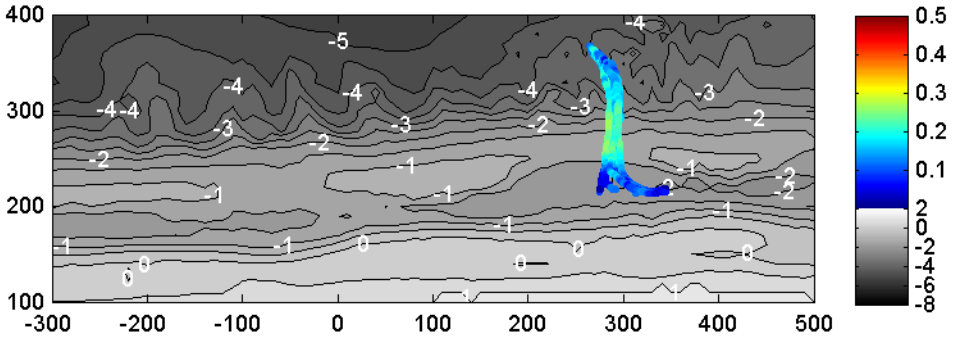

Figure B.8 Drifter trajectories measured on August 23 during dpl.4.

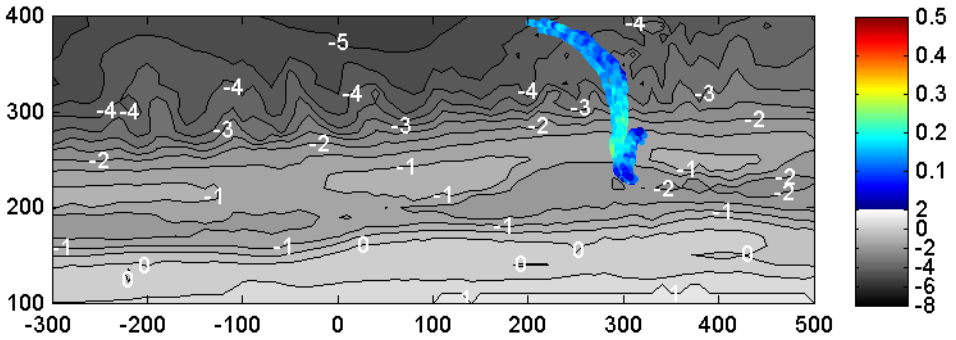

Figure B.9 Drifter trajectories measured on August 23 during dpl.5.

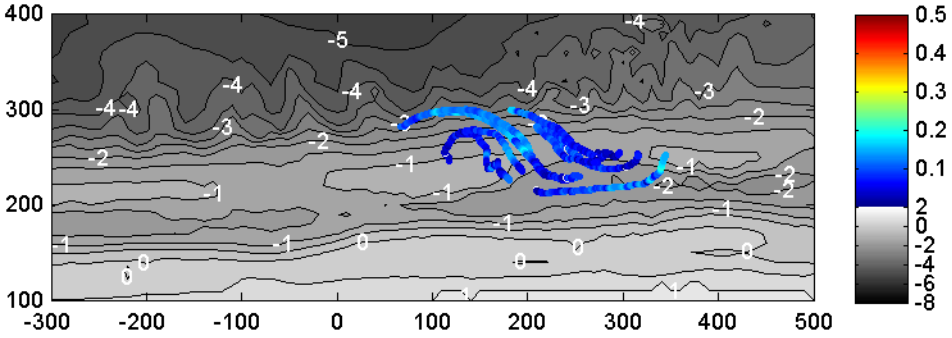

Figure B.10 Drifter trajectories measured on August 24 during dpl.1.

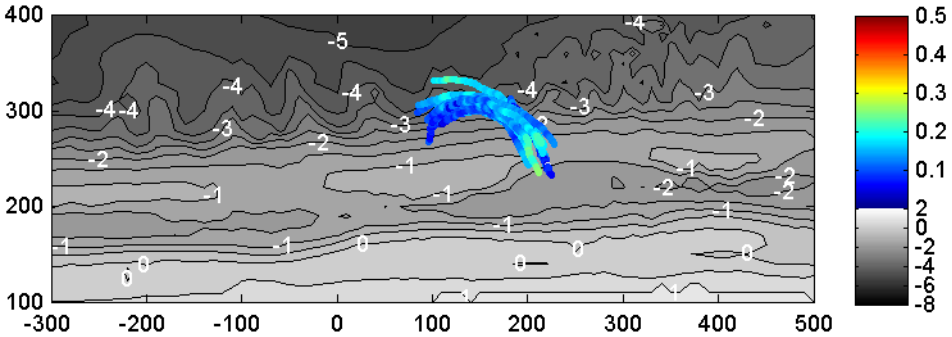

Figure B.11 Drifter trajectories measured on August 24 during dpl.2.

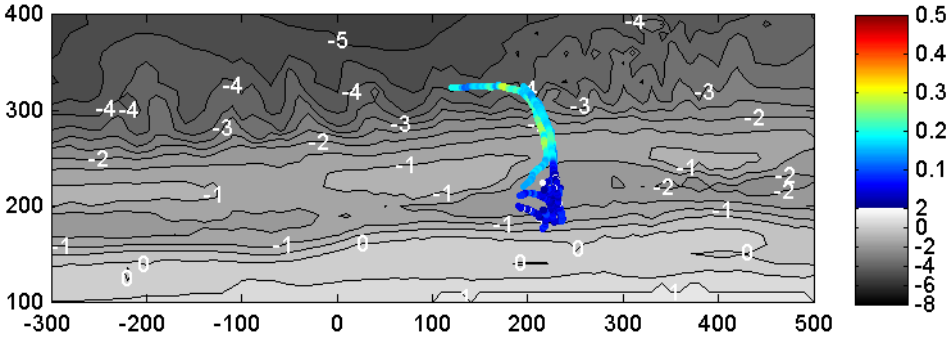

Figure B.12 Drifter trajectories measured on August 24 during dpl.3.

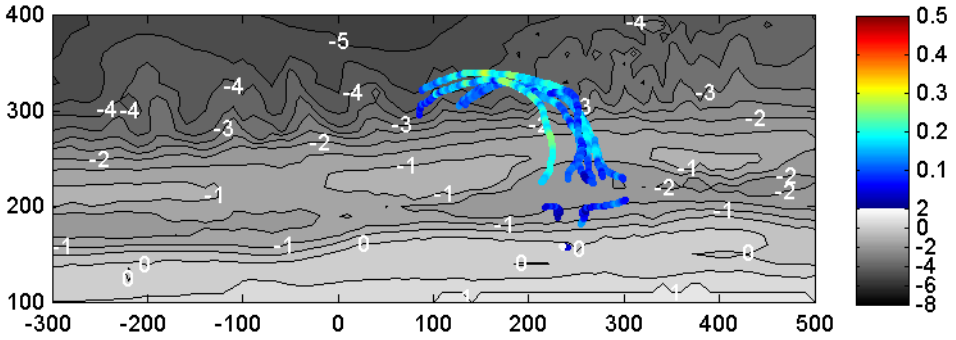

Figure B.13 Drifter trajectories measured on August 24 during dpl.4.

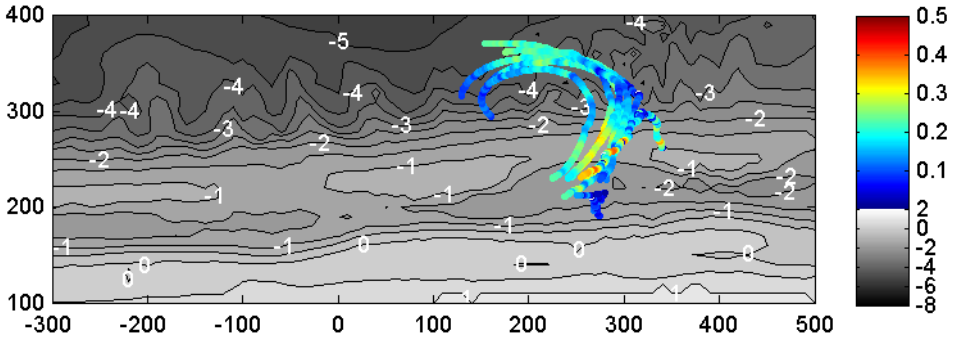

Figure B.14 Drifter trajectories measured on August 24 during dpl.5.

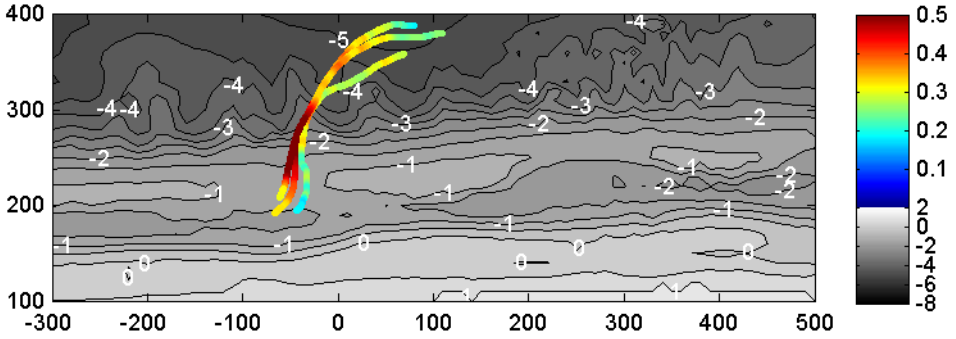

Figure B.15 Drifter trajectories measured on August 25 A during dpl.1.

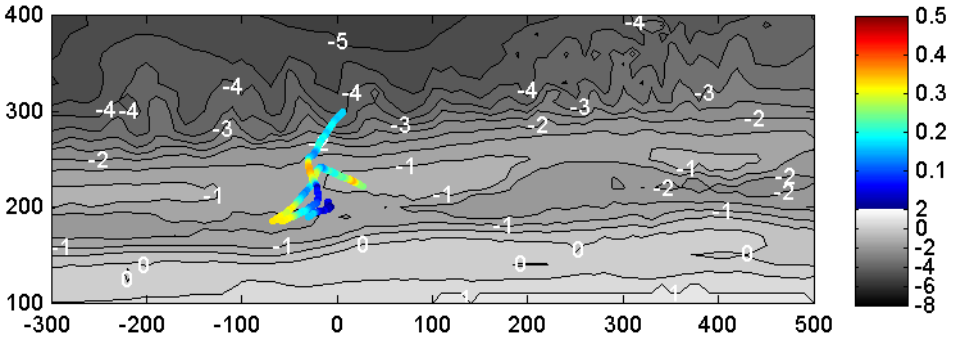

Figure B.16 Drifter trajectories measured on August 25 A during dpl.2.

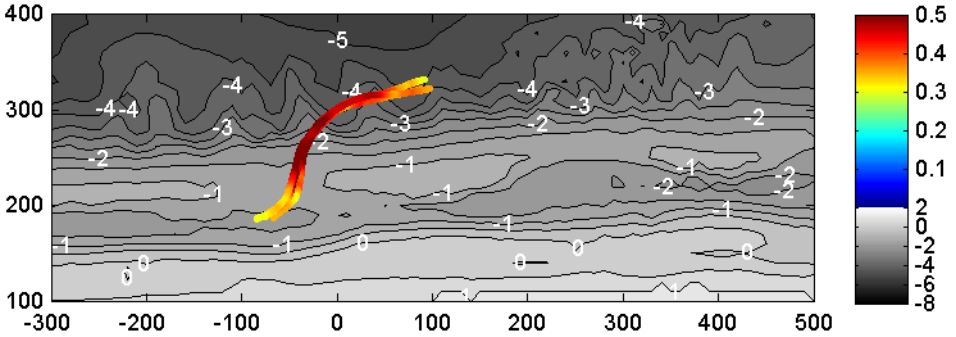

Figure B.17 Drifter trajectories measured on August 25 A during dpl.3.

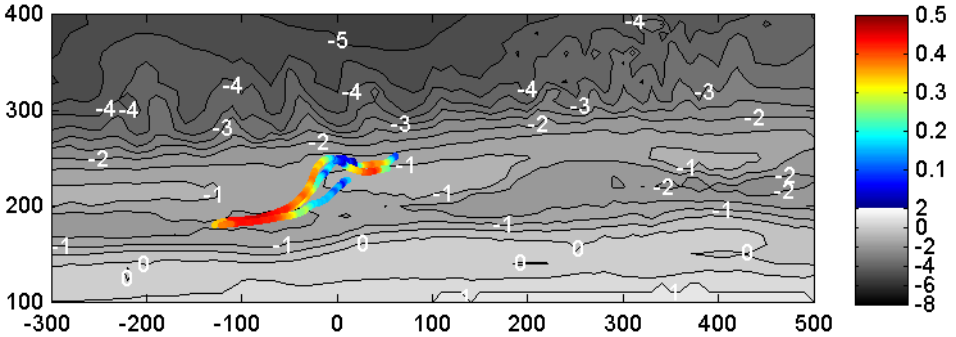

Figure B.18 Drifter trajectories measured on August 25 A during dpl.4.

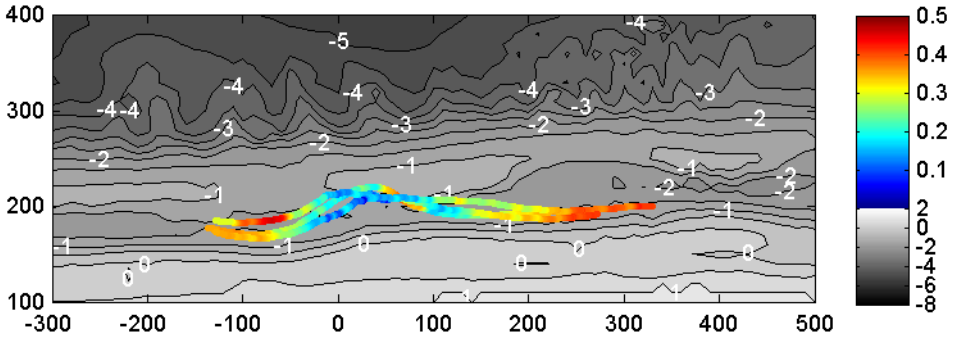

Figure B.19 Drifter trajectories measured on August 25 A during dpl.5.

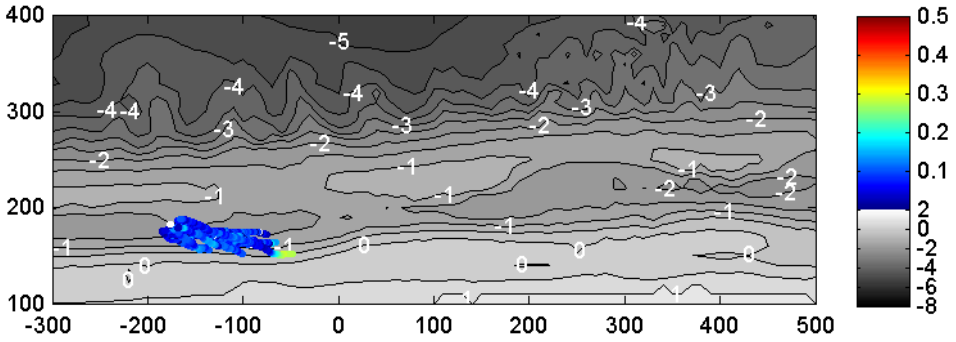

Figure B.20 Drifter trajectories measured on August 25 B during dpl.1.

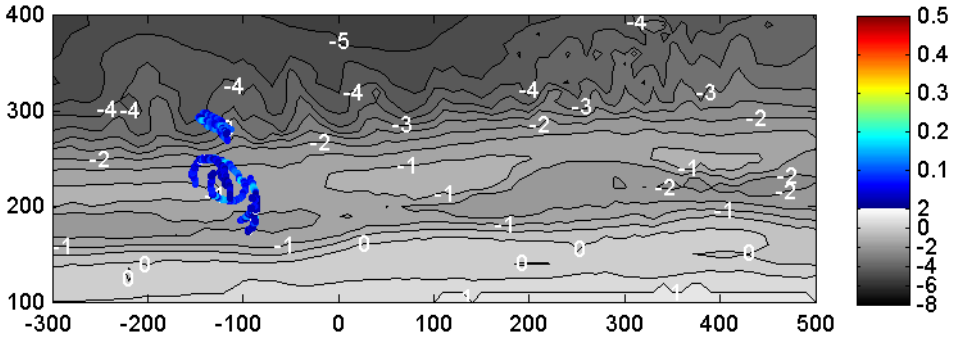

Figure B.21 Drifter trajectories measured on August 25 B during dpl.2.

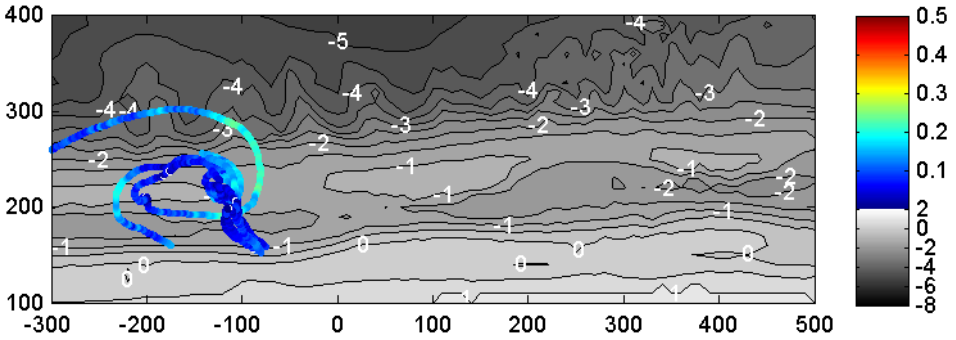

Figure B.22 Drifter trajectories measured on August 25 B during dpl.3.

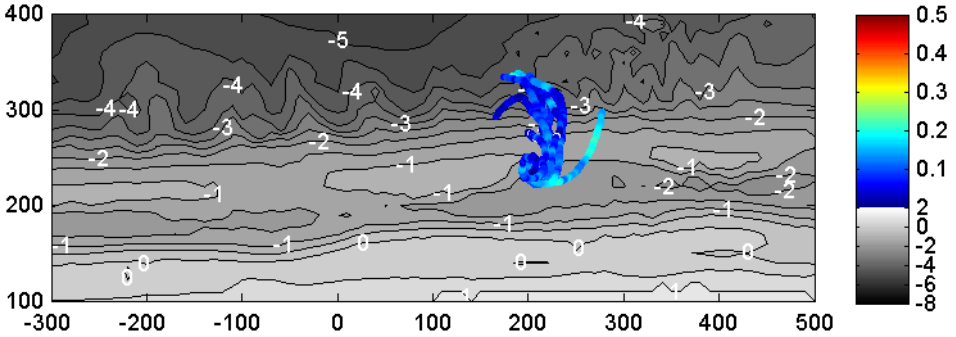

Figure B.23 Drifter trajectories measured on August 25 B during dpl.4.

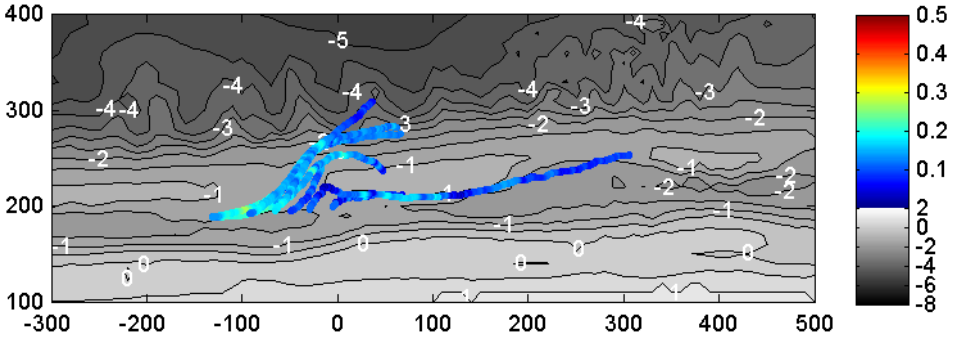

Figure B.24 Drifter trajectories measured on August 26 during dpl.1.

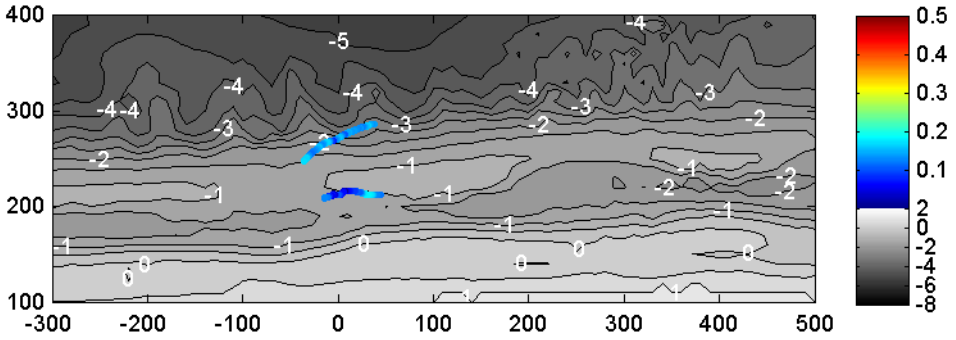

Figure B.25 Drifter trajectories measured on August 26 during dpl.2.

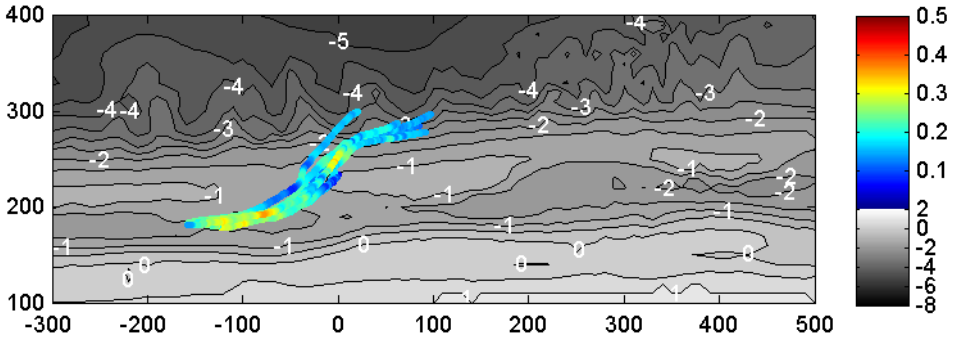

Figure B.26 Drifter trajectories measured on August 26 during dpl.3.

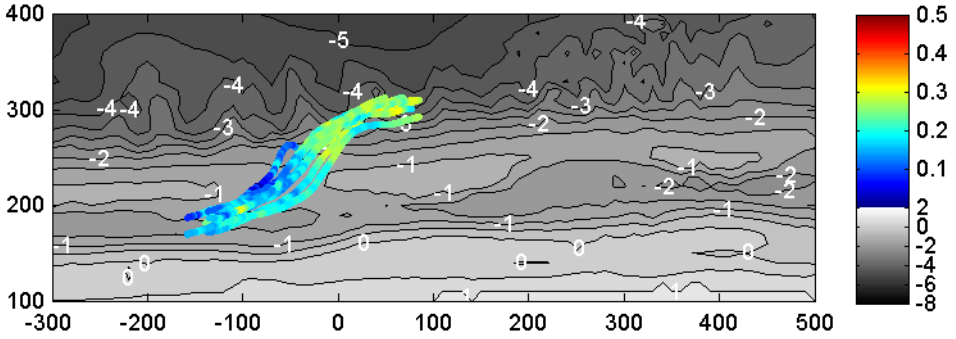

Figure B.27 Drifter trajectories measured on August 26 during dpl.4.

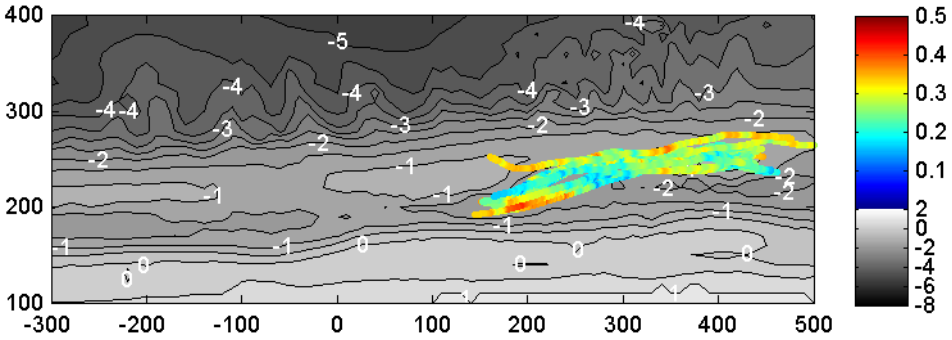

Figure B.28 Drifter trajectories measured on August 26 during dpl.5.

B.3. Sieve curves for the sediment samples

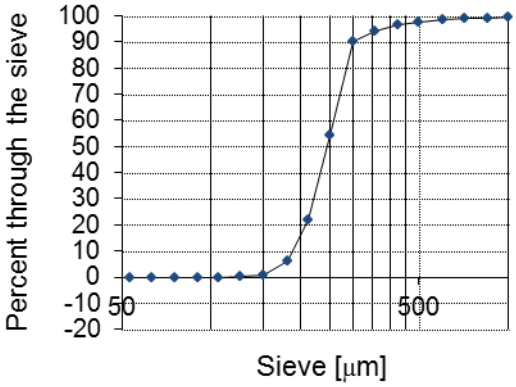

Figure B.29 Sieve curve of the sample taken on August 23 offshore of the southern bar ('South offshore')

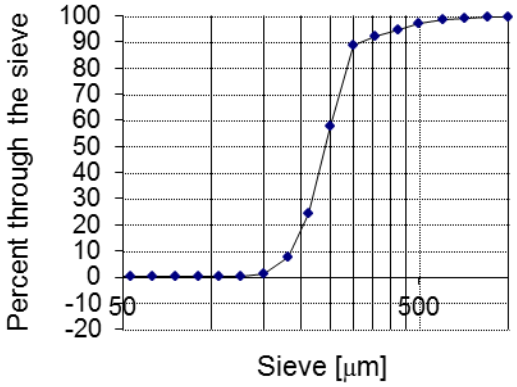

Figure B.30 Sieve curve of the sample taken on August 23 offshore of the rip channel ('Mid offshore')

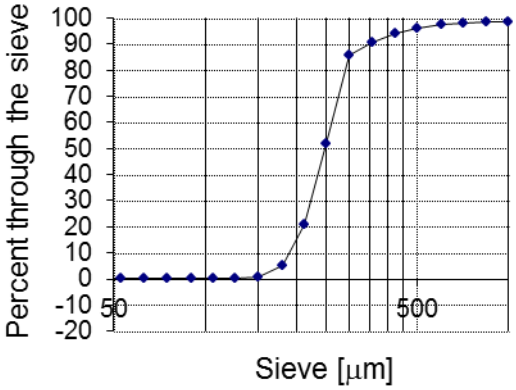

Figure B.31 Sieve curve of the sample taken on August 23 offshore of the northern bar ('North offshore')

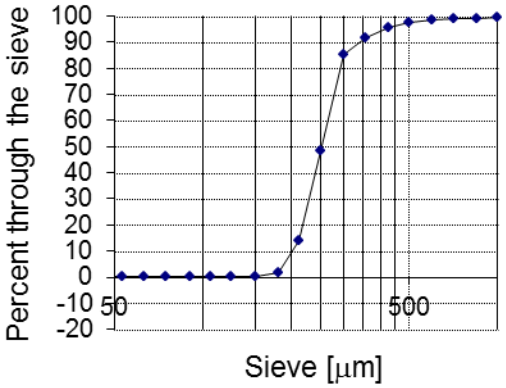

Figure B.32 Sieve curve of the sample taken on August 23 on the southern bar ('South bar')

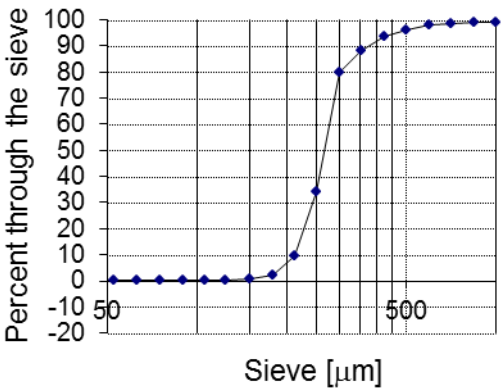

Figure B.33 Sieve curve of the sample taken on August 23 in the rip channel ('Mid bar')

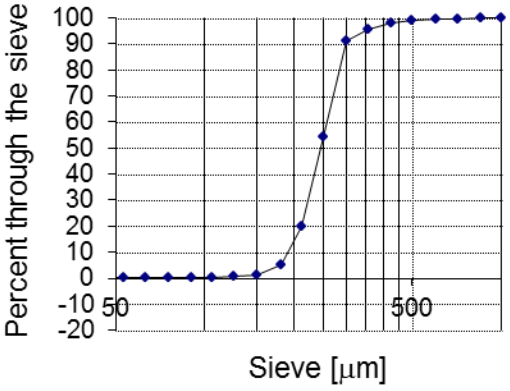

Figure B.34 Sieve curve of the sample taken on August 23 on the northern bar ('North bar)

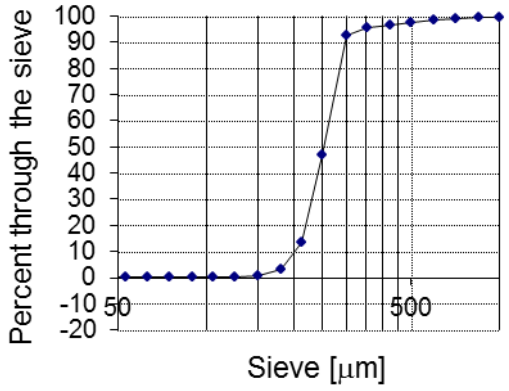

Figure B.35 Sieve curve of the sample taken on August 23 in the southern feeder ('South feeder)

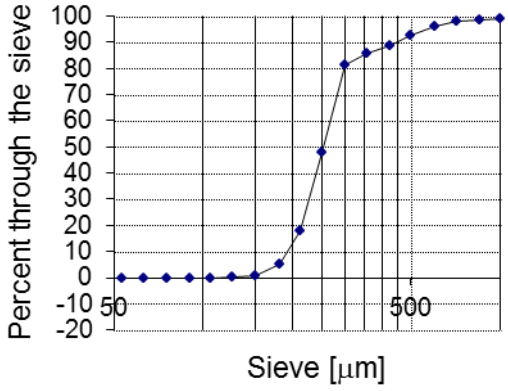

Figure B.36 Sieve curve of the sample taken on August 23 onshore of the rip channel ('Mid feeder')

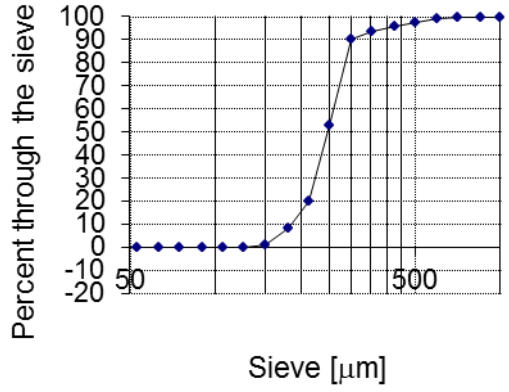

Figure B.37 Sieve curve of the sample taken on August 23 in the northern feeder ('North feeder')

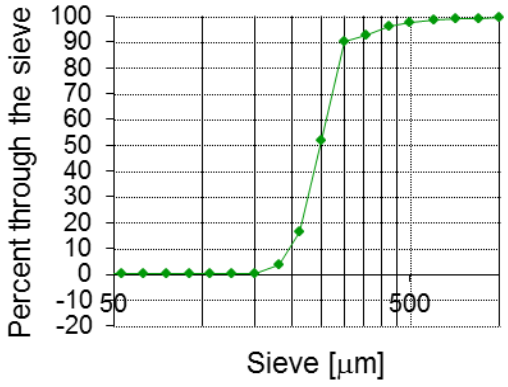

Figure B.38 Sieve curve of the sample taken on August 24 offshore of the southern bar ('South offshore')

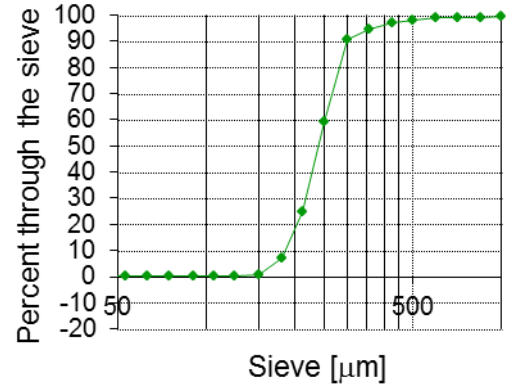

Figure B.39 Sieve curve of the sample taken on August 24 offshore of the rip channel ('Mid offshore')

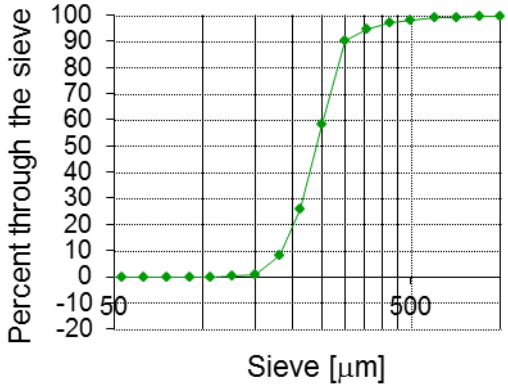

Figure B.40 Sieve curve of the sample taken on August 24 offshore of the northern bar ('North offshore')

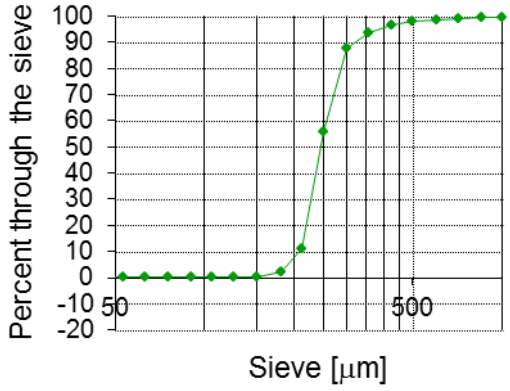

Figure B.41 Sieve curve of the sample taken on August 24 on the southern bar ('South bar')

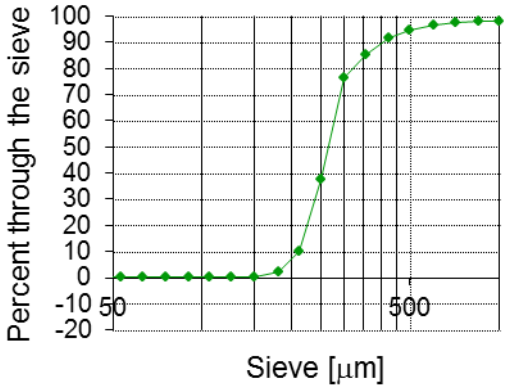

Figure B.42 Sieve curve of the sample taken on August 24 in the rip channel ('Mid bar')

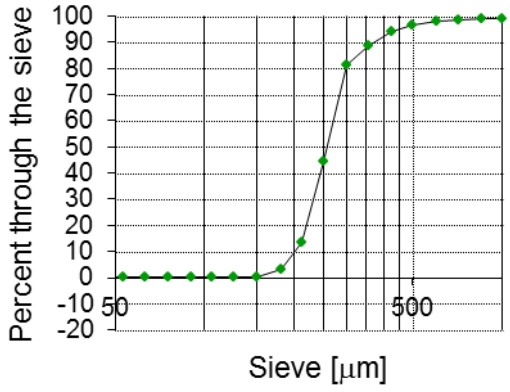

Figure B.43 Sieve curve of the sample taken on August 24 on the northern bar ('North bar)

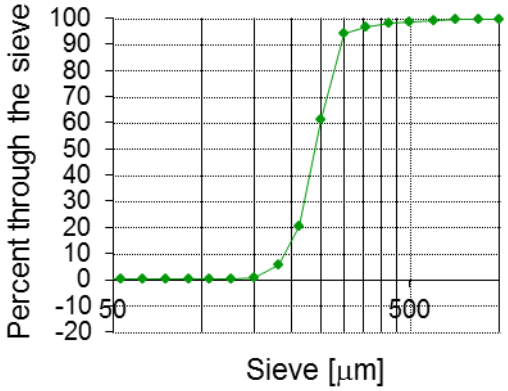

Figure B.44 Sieve curve of the sample taken on August 24 in the southern feeder ('South feeder)

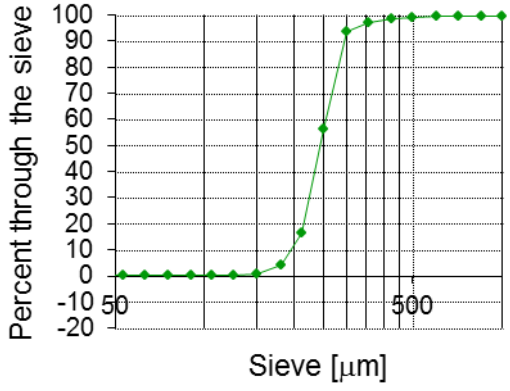

Figure B.45 Sieve curve of the sample taken on August 24 onshore of the rip channel ('Mid feeder')

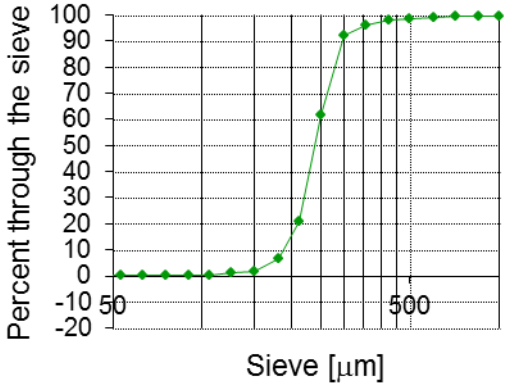

Figure B.46 Sieve curve of the sample taken on August 24 in the northern feeder ('North feeder')

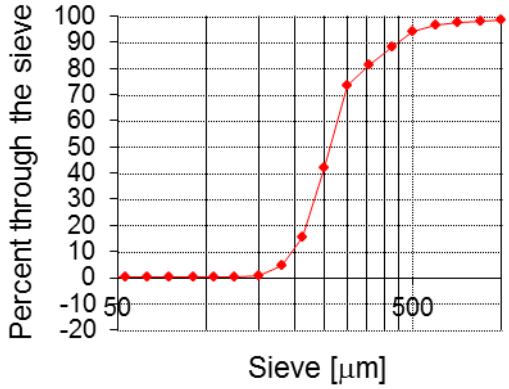

Figure B.47 Sieve curve of the sample taken on August 25 offshore of the southern bar ('South offshore')

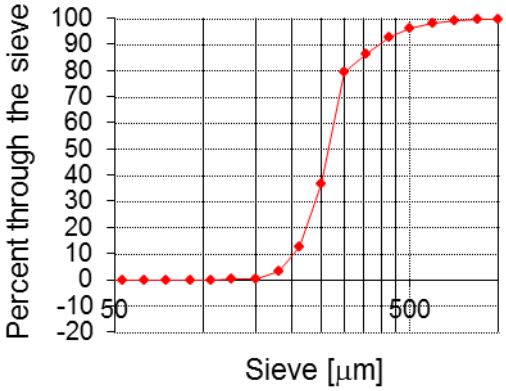

Figure B.48 Sieve curve of the sample taken on August 25 offshore of the rip channel ('Mid offshore')

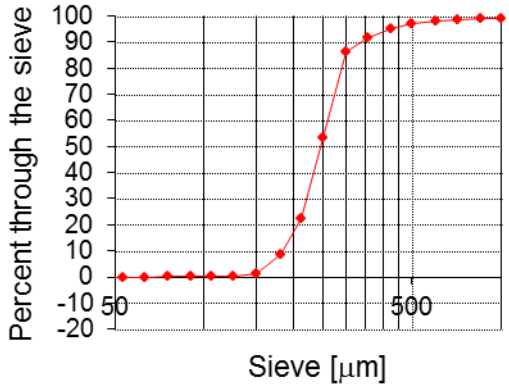

Figure B.49 Sieve curve of the sample taken on August 25 offshore of the northern bar ('North offshore')

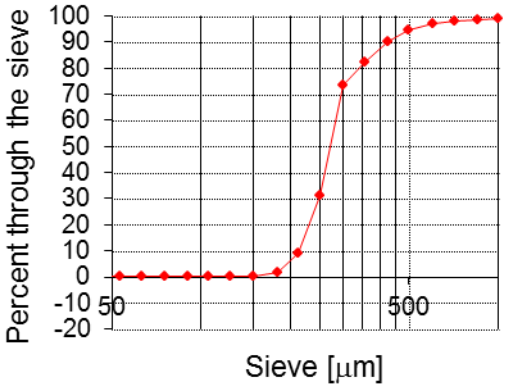

Figure B.50 Sieve curve of the sample taken on August 25 on the southern bar ('South bar')

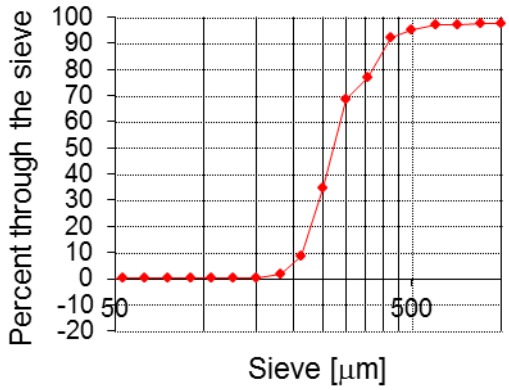

Figure B.51 Sieve curve of the sample taken on August 25 in the rip channel ('Mid bar')

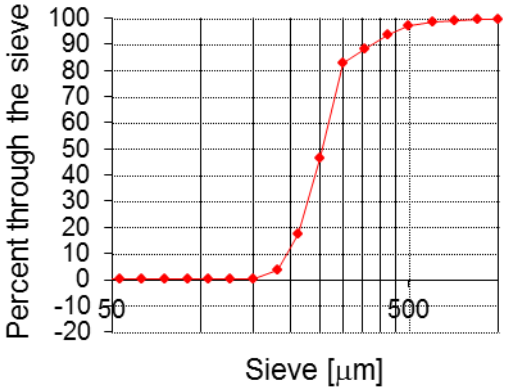

Figure B.52 Sieve curve of the sample taken on August 25 on the northern bar ('North bar)

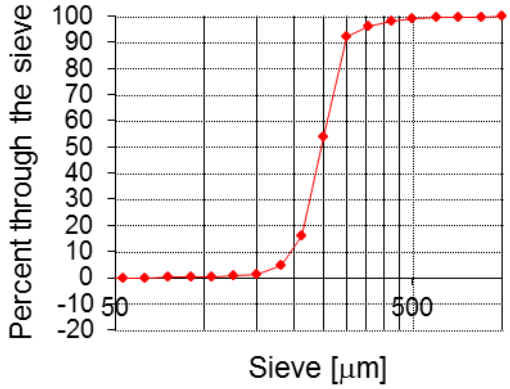

Figure B.53 Sieve curve of the sample taken on August 25 in the southern feeder ('South feeder)

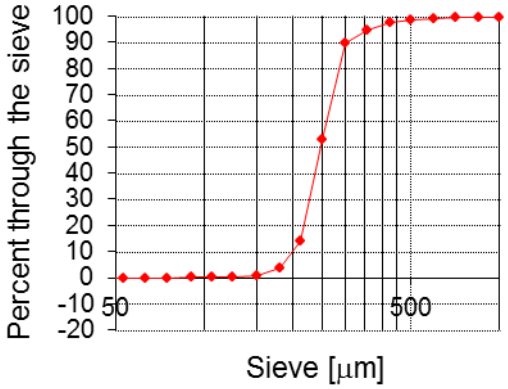

Figure B.54 Sieve curve of the sample taken on August 25 onshore of the rip channel ('Mid feeder')

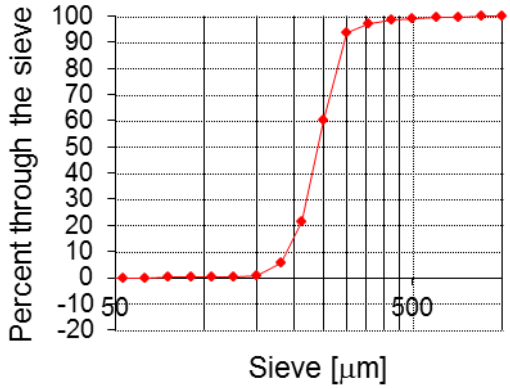

Figure B.55 Sieve curve of the sample taken on August 25 in the northern feeder ('North feeder')

C. Implementation of the tidal current

In XBeach it is only possible to specify water levels at the boundaries. To generate a longshore current two offset water levels need to be defined at the lateral boundaries. These generate a water level gradient that drives the tidal current. Two issues were identified with this tidal current implementation in XBeach: (1) the model of Egmond aan Zee was driven by stationary conditions and (2) the tidal current required some spin up time to fully develop.

The flow simulations are governed by the Nonlinear Shallow Water Equations (NSWE). As the tide flows predominantly shore parallel, only the one-dimensional NSWE in alongshore direction is considered here:

$$\frac{\partial v}{\partial t} + v\frac{\partial v}{\partial y} + g\frac{\partial \eta}{\partial y} + \frac{\tau_b}{\rho h} = 0 \tag{3.1}$$

where v is the tidal current, η the tidal water elevation, ρ the water density, h the local water depth and τ_b the bottom shear stress. Firstly, the difference between the stationary and in-stationary NSWE is examined. In stationary conditions $\partial v/\partial t$ is zero, which means that the negative water level gradient $-\partial \eta/\partial y$ and the tidal current are exactly in phase (Figure C.1, red and green line).

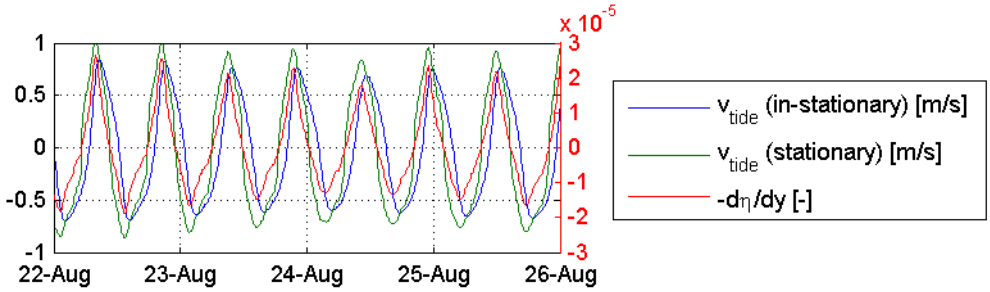

Figure C.1 Tidal current following from the stationary and in-stationary Shallow Water Equation (SWE)

In reality the negative water level gradient and the tidal current are not in phase due to inertia, introduced into the NSWE by the term $\partial v/\partial t$ (Figure C.1, blue line). That implies that the current is not zero when the water level gradient is zero, but remains to flow in the same direction somewhat longer so that the tidal current lags behind the water level gradient. To capture the effect of inertia in the model a large part of the tidal cycle would need to be simulated. For reasons of computational efficiency only single deployments with a duration of 15 to 20 minutes were modelled. Over that period the hydrodynamic conditions were assumed to be stationary. This assumption needed to be accounted for in the water level boundary definition. The tidal current from the Kuststrook model was translated into a stationary water level gradient as follows.

Beginning with equation (3.1) the inertial term $\partial v/\partial t$ was removed for stationary conditions. The contribution by the advection term $v(\partial v/\partial y)$ was considered negligible and the bottom shear stress was substituted by a quadratic friction law as follows:

$$\tau_b = \rho c_f u |u| . \tag{3.2}$$

For the stationary water level gradient, it then follows:

$$\frac{\Delta \eta}{\Delta y} = -c_f \frac{v|v|}{gh} \tag{3.3}$$

where v is the tidal longshore current. With the knowledge of $\Delta\eta/\Delta y$ and the size of the numerical domain, the water levels at the boundary were extrapolated from the mean water level over the domain.

Equation (3.3) resulted in very small water level gradients (in the order of a few millimetres). Because the driving force was so small the spin up time for the tidal current amounted to ~10 hours (Figure C.2). To save computational time a 'flow hotstart' option was implemented in XBeach. An initial flow field is calculated from a simplified linear stationary SWE that reads as follows:

$$g \frac{\partial \eta}{\partial y} + \frac{\tau_b}{\rho h} - \frac{\tau_w}{\rho h} = 0 \tag{3.4}$$

where τ_w is the wind stress at the surface.

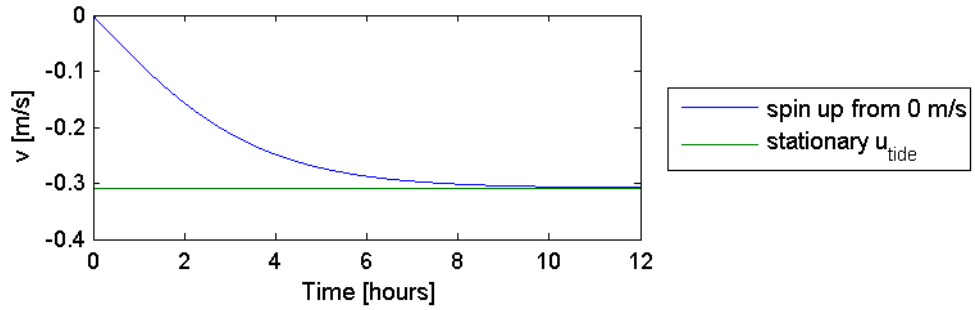

Figure C.2 Spin up time that the model needs to develop the tidal current for example for the hindcast of August 22 (dpl.4): It takes ~10 hours to reach the tidal velocity of -0.32 m/s.

D. Hindcast drifter trajectories

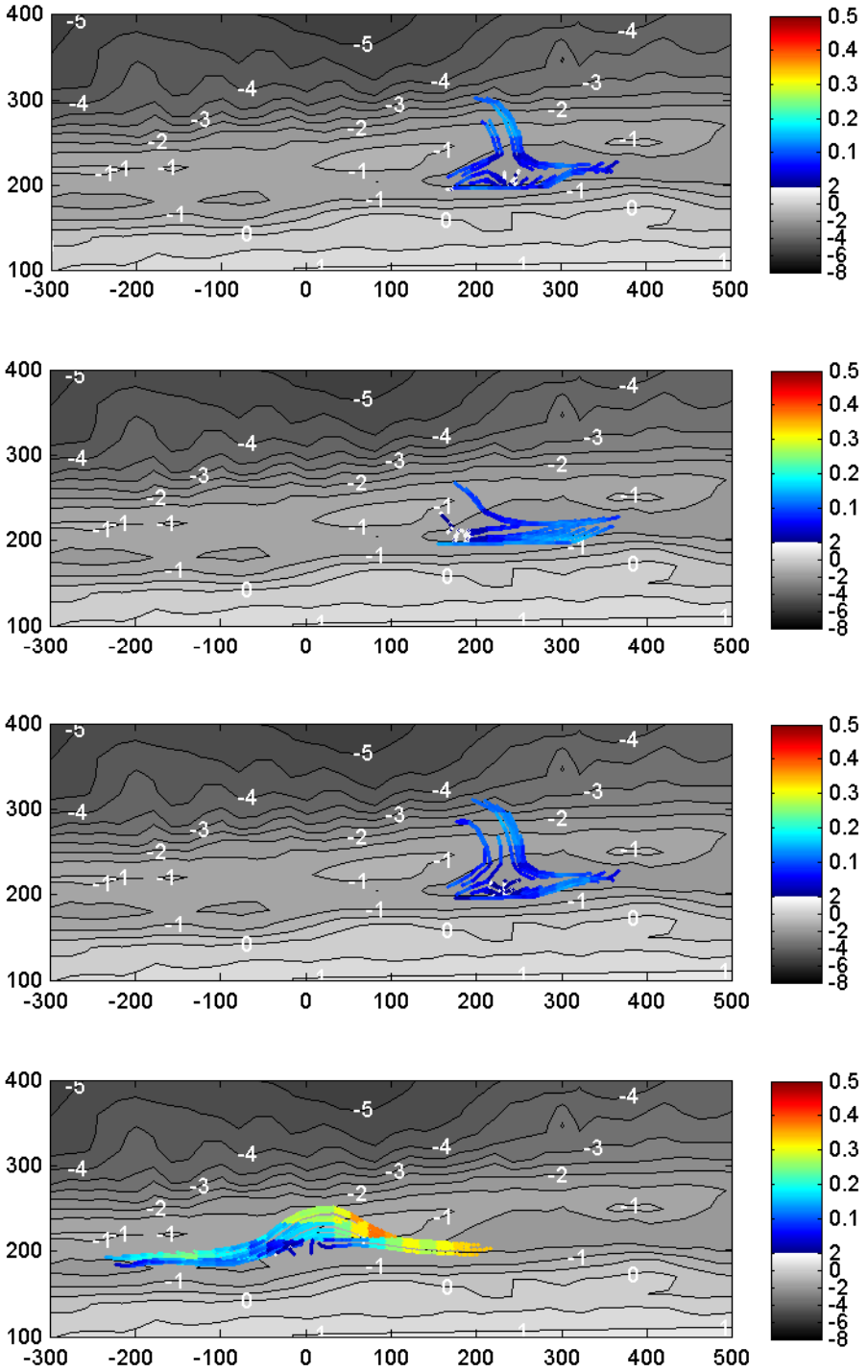

Figure D.1 Drifter trajectories in the model simulated on a 20 x 20 m grid.

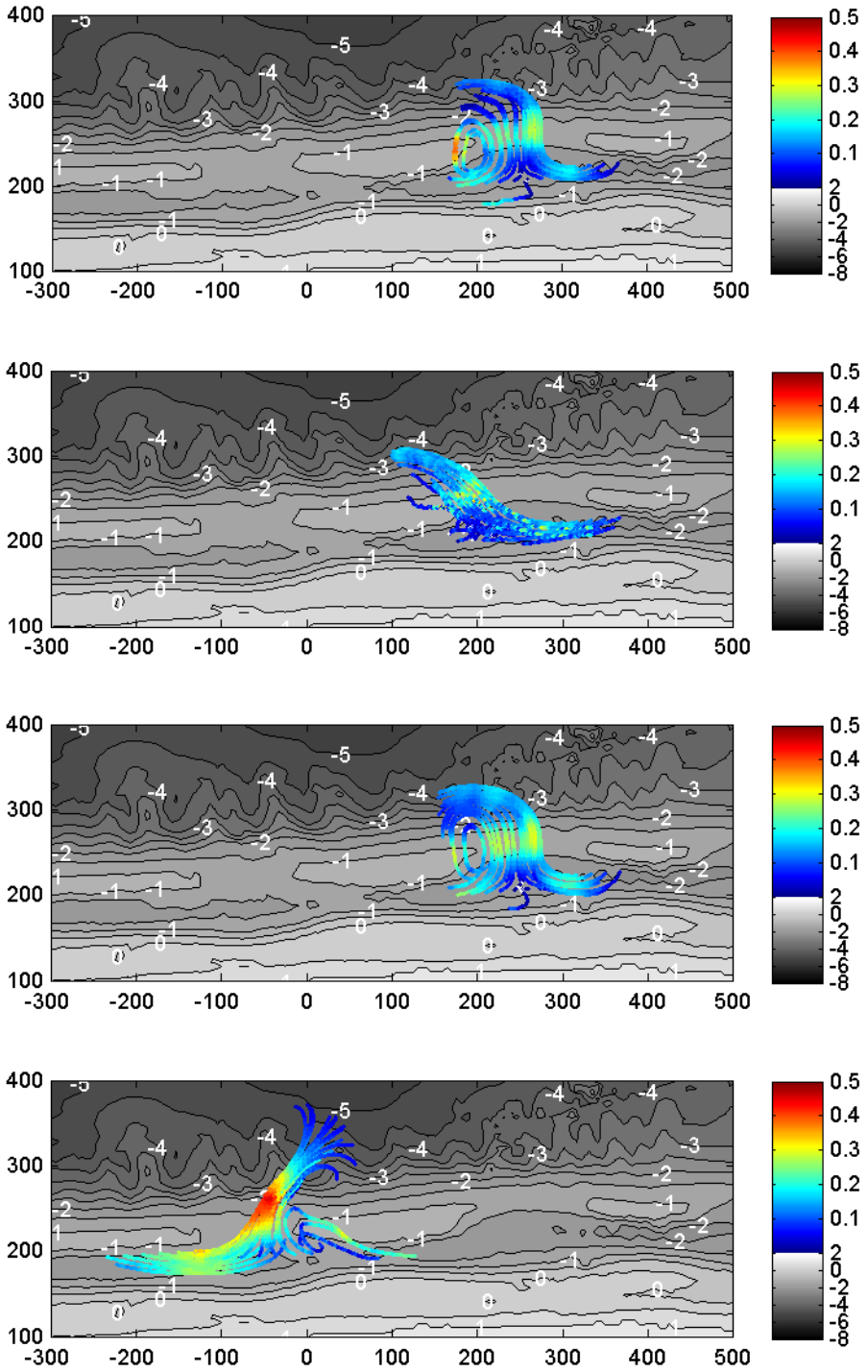

Figure D.2 Drifter trajectories in the model simulated on a 5 x 5 m grid.

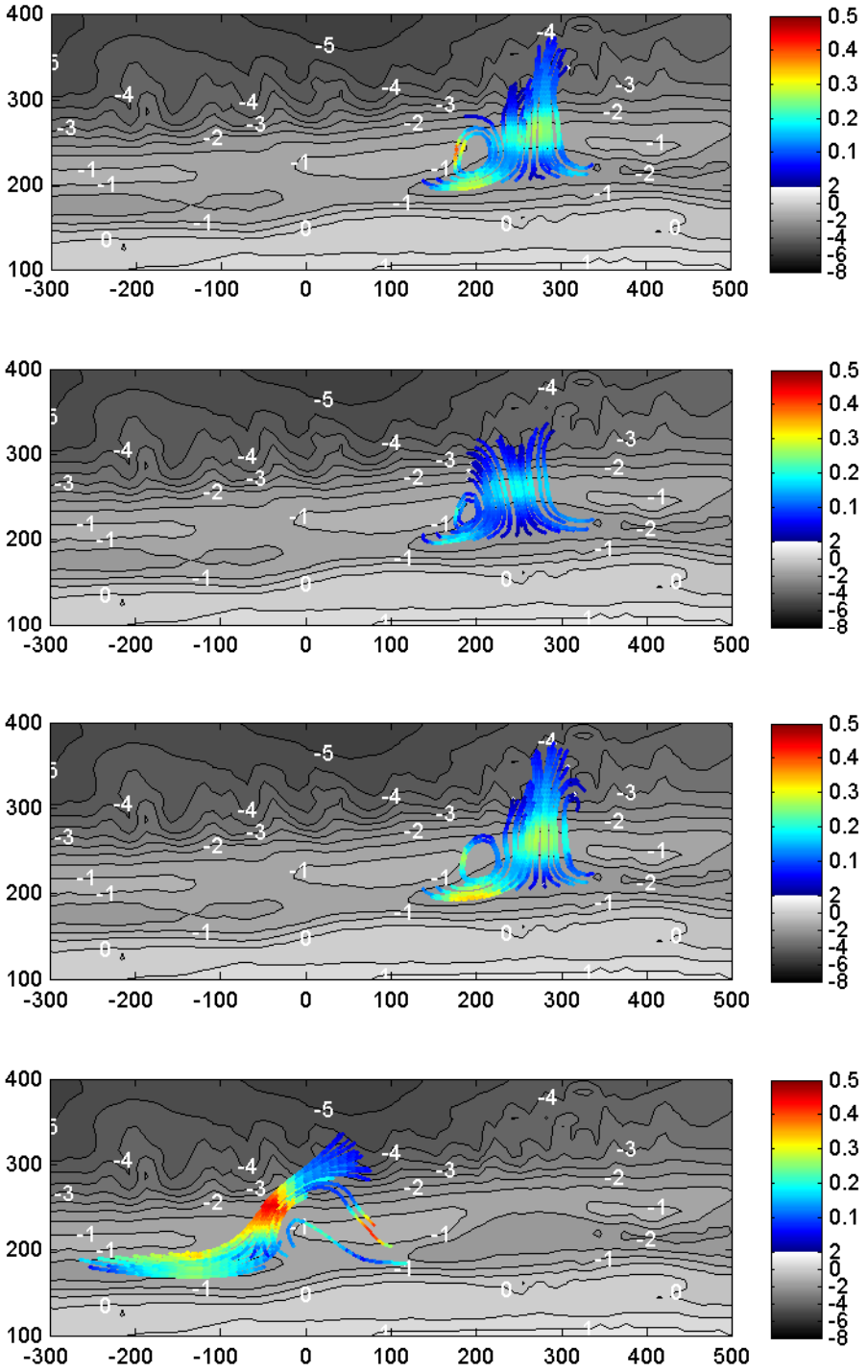

Figure D.3 Drifter trajectories in the model simulated without tidal currents.

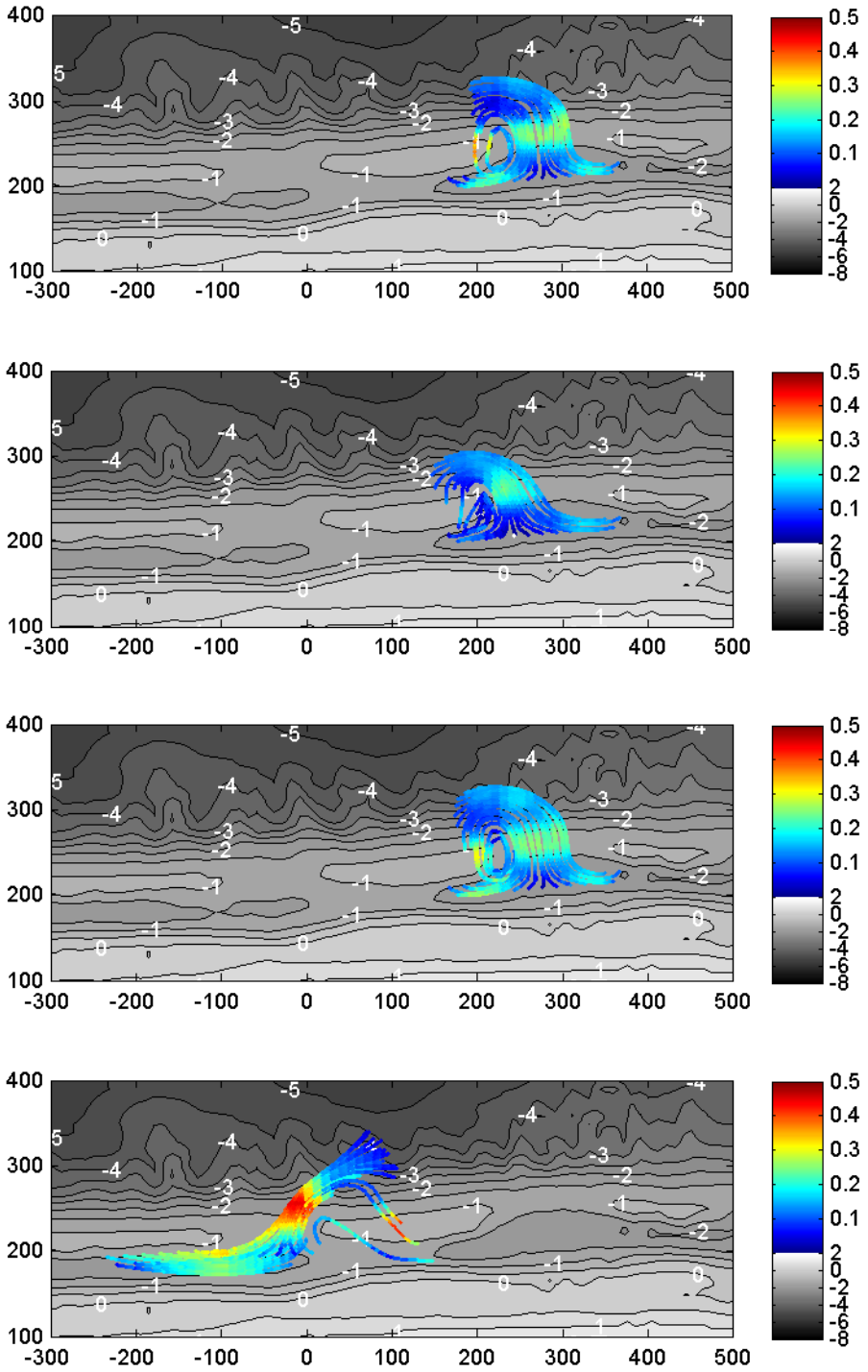

Figure D.4 Drifter trajectories in the model simulated with α_{roller} = 0.1.

E. Hindcast field measurements with in-stationary waves

In this study, rip currents were investigated with a model driven by stationary waves. The hindcast of the field measurements was also tested with the in-stationary wave driver in XBeach.

The longshore variation in wave height associated with wave groups generates rip currents independent from the bathymetry. The underlying bathymetry forces the rip circulation cells into rip channels and provokes oscillatory motions of the rip current at very low frequencies [*MacMahan et al.*, 2004]. These are believed to cause ejection of floating material from the surf zone [*Reniers et al.*, 2009].

The in-stationary short wave module is driven by the energy of the short waves that is resolved on the wave group scale. The wave field is composed of a superposition of linear wave components with different frequencies. The phase and directional information associated with each wave component are determined statistically. Bound long waves are generated through the interaction of short waves with different frequencies. For a detailed description of the procedure the reader is referred to *van Dongeren et al.* [2003].

The measured spectral wave data from the directional offshore buoy (Section 4.3.1) was transformed into an XBeach input spectra (Figure E.1).

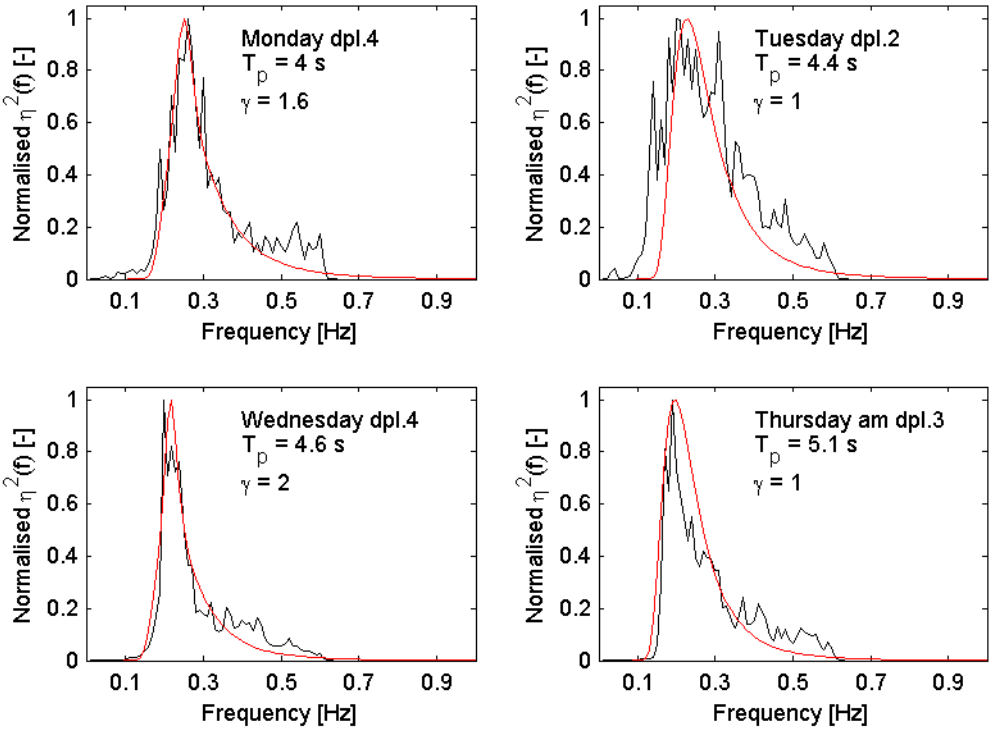

Figure E.1 Offshore wave conditions during the hindcasted deployments: Measured spectra (black) and XBeach input spectra (red). T_p is the peak frequency and γ is the peak enhancement factor in this context.

The in-stationary wave driver produced similar results to the stationary wave driver (Figure E.2) and did not provoke more drifter exits than the model presented in Chapter 6. It was observed in this context that the roller induced viscosity had a significant influence on the

results with in-stationary waves and the model calibrated better with $\alpha_{roller} = 0.1$ than with $\alpha_{roller} = 1$.

Along with the results from the sensitivity analysis (Section 7.3.3) it is concluded that surf zone exits are attributed to the lack of longshore in the case of Egmond aan Zee. However, the influence of wave group forcing on rip currents at Egmond aan Zee was not measured in the field and the model could not be validated. To investigate the impact of wave groups on rip currents at Egmond and Zee was not objective of this study and further research is required.

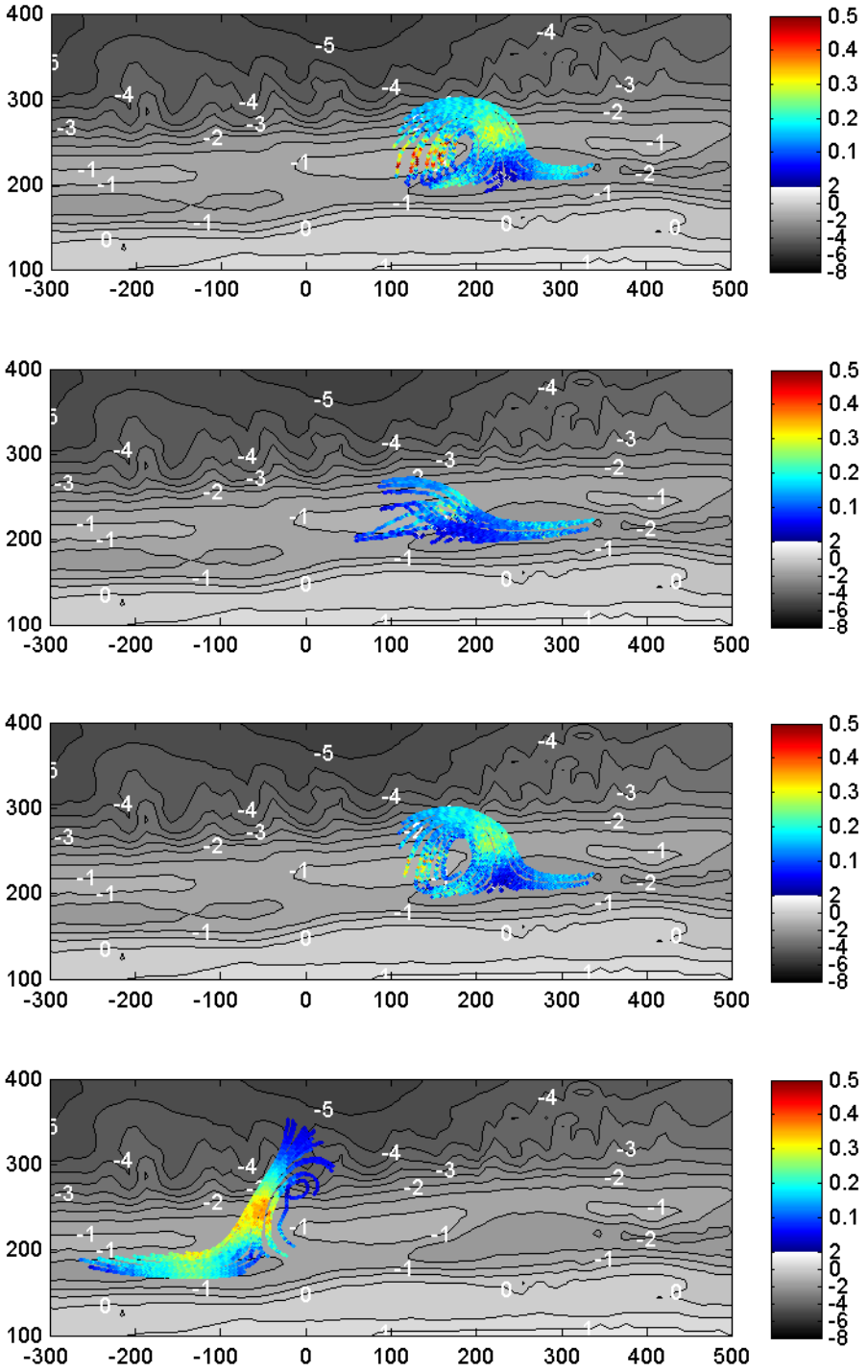

Figure E.2 Drifter trajectories simulated with in-stationary waves and α_{roller} = 0.1.